



DEIVIDAS MARTINAVIČIUS

---

**RESEARCH OF LOCAL  
BUCKLING BEHAVIOUR  
OF COMPOSITE  
THIN-WALLED  
STEEL-CONCRETE  
STRUCTURES**

---

DOCTORAL DISSERTATION

K a u n a s  
2 0 2 2

KAUNAS UNIVERSITY OF TECHNOLOGY

DEIVIDAS MARTINAVIČIUS

RESEARCH OF LOCAL BUCKLING  
BEHAVIOUR OF COMPOSITE THIN-WALLED  
STEEL-CONCRETE STRUCTURES

Doctoral dissertation  
Technological Sciences, Civil Engineering (T 002)

Kaunas, 2022

This doctoral dissertation was prepared at Kaunas University of Technology, Faculty of Civil Engineering and Architecture, Department of Civil Engineering and Architecture Competence Centre during the period of 2017–2021.

**Scientific Supervisor:**

Assoc. Prof. Dr. Mindaugas AUGONIS (Kaunas University of Technology, Technological Sciences, Civil Engineering, T 002).

**Scientific Advisor:**

Dr. Mário Rui Tiago ARRUDA (University of Lisbon, Portugal, Technological Sciences, Civil Engineering, T 002).

Edited by: English language editor Dr. Armandas Rumšas (Publishing House *Technologija*), Lithuanian language editor Violeta Meiliūnaitė (Publishing House *Technologija*).

**Dissertation Defence Board of Civil Engineering Science Field:**

Prof. Dr. Tadas ŽDANKUS (Kaunas University of Technology, Technological Sciences, Civil Engineering, T 002) – **chairman**;

Prof. Dr. Mindaugas DAUKŠYS (Kaunas University of Technology, Technological Sciences, Civil Engineering, T 002);

Prof. Dr. Valdas EIDUKYNAS (Kaunas University of Technology, Technological Sciences, Mechanical Engineering, T 009);

Dr. João Pedro FIRMO (University of Lisbon, Portugal, Technological Sciences, Civil Engineering, T 002);

Assoc. Prof. Dr. Darius ZABULIONIS (Vilnius Gediminas Technical University, Technological Sciences, Civil Engineering, T 002).

The official defence of the dissertation will be held at 10:00 a.m. on 16<sup>th</sup> of May, 2022 at the public meeting of the Dissertation Defence Board of Civil Engineering Science Field in the Dissertation Defence Hall at Kaunas University of Technology.

Address: K. Donelaičio St. 73-403, Kaunas, LT-44249, Lithuania.

Phone (+370) 37 300 042; fax. (+370) 37 324 144; email [doktorantura@ktu.lt](mailto:doktorantura@ktu.lt)

The doctoral dissertation was sent out on 15<sup>th</sup> of April, 2022.

The doctoral dissertation is available on the internet at <http://ktu.edu> and at the library of Kaunas University of Technology (K. Donelaičio St. 20, Kaunas, LT-44239, Lithuania).

KAUNO TECHNOLOGIJOS UNIVERSITETAS

DEIVIDAS MARTINAVIČIUS

PLONASIENIŲ KOMPOZITINIŲ  
PLIENBETONINIŲ KONSTRUKCIJŲ VIETINIO  
KLUPUMO ELGSENOS TYRIMAI

Daktaro disertacija  
Technologijos mokslai, statybos inžinerija (T 002)

Kaunas, 2022



Disertacija rengta 2017–2021 metais Kauno technologijos universiteto Statybos ir architektūros fakultete, Statybos ir architektūros kompetencijų centre.

**Mokslinis vadovas:**

doc. dr. Mindaugas AUGONIS (Kauno technologijos universitetas, technologijos mokslai, statybos inžinerija, T 002).

**Mokslinis konsultantas:**

dr. Mário Rui Tiago ARRUDA (Lisabonos universitetas, Portugalija, technologijos mokslai, statybos inžinerija, T 002).

Redagavo: anglų kalbos redaktorius dr. Armandas Rumšas (leidykla „Technologija“), lietuvių kalbos redaktorė Violeta Meiliūnaitė (leidykla „Technologija“).

**Statybos inžinerijos mokslo krypties disertacijos gynimo taryba:**

prof. dr. Tadas ŽDANKUS (Kauno technologijos universitetas, technologijos mokslai, statybos inžinerija, T 002) – **pirmininkas**;

prof. dr. Mindaugas DAUKŠYS (Kauno technologijos universitetas, technologijos mokslai, statybos inžinerija, T 002);

prof. dr. Valdas EIDUKYNAS (Kauno technologijos universitetas, technologijos mokslai, mechanikos inžinerija, T 009);

dr. João Pedro FIRMO (Lisabonos universitetas, Portugalija, technologijos mokslai, statybos inžinerija, T 002);

doc. dr. Darius ZABULIONIS (Vilniaus Gedimino technikos universitetas, technologijos mokslai, statybos inžinerija, T 002).

Disertacija bus ginama viešame Statybos inžinerijos mokslo krypties disertacijos gynimo tarybos posėdyje 2022 m. gegužės 16 d. 10:00 val. Kauno technologijos universiteto Disertacijų gynimo salėje.

Adresas: K. Donelaičio g. 73-403, Kaunas LT-44249, Lietuva.

Tel. (+370) 37 300 042; faks. (+370) 37 324 144; el. paštas [doktorantura@ktu.lt](mailto:doktorantura@ktu.lt)

Disertacija išsiųsta 2022 m. balandžio 15 d.

Su disertacija galima susipažinti interneto svetainėje <http://ktu.edu> ir Kauno technologijos universiteto bibliotekoje (K. Donelaičio g. 20, 44239 Kaunas).

## TABLE OF CONTENTS

ACKNOWLEDGMENT	7
NOTATION	8
ABBREVIATIONS	11
LIST OF FIGURES	12
LIST OF TABLES	14
INTRODUCTION	15
I. REVIEW OF THE LATEST RESEARCH	18
1.1. Advantages and practical use of composite steel-concrete structures .....	18
1.2. Compressive behaviour of concrete in composite steel-concrete structures.....	19
1.3. Initial imperfections of steel profiles.....	25
1.3.1. Geometrical imperfections	25
1.3.2. Residual stresses	27
1.4. Local buckling behaviour of steel structures .....	30
1.5. Local buckling behaviour of steel-concrete structures .....	31
1.6. Other research of structural behaviour of steel-concrete structures.....	36
1.7. Conclusions of Chapter One.....	39
II. EXPERIMENTAL RESEARCH OF THIN-WALLED STEEL-CONCRETE STRUCTURES	40
2.1. Experimental testing of concrete-filled welded steel columns .....	40
2.1.1. Preparation and properties of column specimens	40
2.1.2. Compressive column test setup and procedure	42
2.1.3. Experimental results of thin-walled steel concrete columns	43
2.2. Experimental testing of concrete-filled welded steel beams.....	47
2.2.1. Preparation and properties of beam specimens	47
2.2.2. Flexural beam test setup and procedure	50
2.2.3. Experimental results of thin-walled steel concrete beams	51
2.3. Conclusions of Chapter Two .....	54
III. THEORETICAL RESEARCH OF THIN-WALLED COMPOSITE STEEL-CONCRETE STRUCTURES	55
3.1. Calculation methods for thin-walled steel-concrete columns .....	55
3.1.1. Methods and general expressions	55
3.1.2. Comparison of calculation methods for thin-walled steel-concrete columns	55
3.2. Numerical modelling of thin-walled composite steel-concrete structures .....	57
3.2.1. Geometry and mesh	57

3.2.2. Material models and initial imperfections	58
3.2.3. Contacts, boundary conditions, loads and assembly of models	60
3.2.4. Numerical analysis of thin-walled composite steel-concrete columns	62
3.2.5. Numerical analysis of thin-walled composite steel-concrete beams	68
3.3. Proposed average normal-stress strain model for compressed steel flanges in concrete-filled steel structures .....	78
3.4. Iterative layer method for stress-strain analysis of thin-walled steel-concrete beams	84
3.5. Conclusions of Chapter Three .....	88
IV. RESULTS	89
4.1. Results of thin-walled steel-concrete columns.....	89
4.2. Results of thin-walled steel-concrete beams.....	92
4.3. Conclusions of Chapter Four .....	95
CONCLUSIONS	96
FUTURE DEVELOPMENTS	98
SANTRAUKA	99
REFERENCES	131
CURRICULUM VITAE	139
LIST OF SCIENTIFIC ARTICLES ON THE DISSERTATION TOPIC	140

## ACKNOWLEDGMENT

The author would like to express gratitude to the supervisor Associate Professor Mindaugas Augonis for the consultations, all the help and assistance during the experimental campaign and all the support throughout the period of the PhD studies.

The author is sincerely thankful to the scientific advisor Research Associate Mário Rui Tiago Arruda for the support during the traineeship at Instituto Superior Técnico, Universidade de Lisboa and all the consultations regarding the application of the finite element method.

The author is also sincerely grateful to André Biscaya for the consultations regarding the implementation of the programming code in the finite element analysis.

Furthermore, the author would like to express gratitude to the colleagues at Kaunas University of Technology Tadas Lisauskas and Vadimas Kitovas for the support and help during the experimental campaign. The author is also grateful to Tadas Zingaila for the support and helpful insights regarding the design and analysis of steel structures.

Finally, the author is especially thankful to his wife Greta, parents Danguolė and Vidas for all the care and support.

## NOTATION

$a$  – concrete cover, mm;  
 $a_{cr,b}$  – variable for compressed beam flange critical stress calculation, MPa;  
 $a_{cr,c}$  – variable for column panel critical stress calculation, MPa;  
 $a_i$  – constant coefficients for critical stress calculation;  
 $a_{u,b}$  – variable for compressed beam flange ultimate stress calculation, MPa;  
 $a_{u,c}$  – variable for column panel ultimate stress calculation, MPa;  
 $a_{u,c,l}$  – variable for column panel ultimate stress calculation, MPa;  
 $A_c$  – cross-sectional area of concrete core, mm<sup>2</sup>;  
 $A_{eff}$  – effective cross-sectional area of steel profile, mm<sup>2</sup>;  
 $A_s$  – cross-sectional area of steel profile, mm<sup>2</sup>;  
 $A_{sr}$  – total cross-sectional area of steel rebars, mm<sup>2</sup>;  
 $b$  – inner width of steel profile, mm;  
 $b_{eff}$  – effective width of steel panel, mm;  
 $b_{ne}$  – ineffective width of steel panel, mm;  
 $b_{ne,u}$  – maximum ineffective width of steel panel, mm;  
 $b_h$  – half-width of steel flange, mm;  
 $B$  – outer width of steel profile, mm;  
 $B_s$  – larger dimension of width and height of cross-section, mm;  
 $c_{cr,b}$  – variable for compressed beam flange critical stress calculation, MPa;  
 $c_{cr,c}$  – variable for column panel critical stress calculation, MPa;  
 $c_i$  – constant coefficients for ultimate stress calculation;  
 $c_{u,b}$  – variable for column panel ultimate stress calculation, MPa;  
 $c_{u,c}$  – variable for column panel ultimate stress calculation, MPa;  
 $c_{u,c,l}$  – variable for column panel ultimate stress calculation, MPa;  
 $d$  – layer height, mm;  
 $e$  – distance between centre lines of loading and support plates, mm;  
 $f_{b0}$  – equibiaxial compressive yield stress, MPa;  
 $f_{c0}$  – uniaxial compressive yield stress, MPa;  
 $f'_{cc}$  – compressive strength of confined concrete, MPa;  
 $f_{cm}$  – mean value of concrete cylinder compressive strength, MPa;  
 $f_{ctk,0.95}$  – 95% percentile of axial tensile strength of concrete, MPa;  
 $f_{ctm}$  – mean value of axial tensile strength of concrete, MPa;  
 $f_{c,avg}$  – average cubic compressive strength of concrete specimens, MPa;  
 $f_{c,i}$  – compressive strength of cubic concrete specimen, MPa;  
 $f_l$  – confining pressure, MPa;  
 $f_y$  – yield strength of steel, MPa;  
 $f_{y,avg}$  – average yield strength of steel specimens, MPa;  
 $f_{pym}$  – stress difference value, MPa;  
 $f_{sy}$  – yield strength of steel rebar, MPa;  
 $f_{su}$  – ultimate strength of steel rebar, MPa;  
 $f_u$  – ultimate strength of steel, MPa;  
 $f_{u,ex}$  – experimental ultimate stress of steel panel, MPa;  
 $E_{0.7}$  – secant elasticity modulus of steel, GPa;

$E_c$  – modulus of elasticity of concrete, GPa;  
 $E_{c,avg}$  – average modulus of elasticity of concrete specimens, GPa;  
 $E_{c,i}$  – modulus of elasticity of concrete specimen, GPa;  
 $E_s$  – elasticity modulus of steel, GPa;  
 $E_{sr}$  – elasticity modulus of steel rebar, GPa;  
 $G$  – non-associated plastic flow potential;  
 $G_f$  – fracture energy of concrete, N/m;  
 $h$  – inner height of steel profile, mm;  
 $H$  – outer height of steel profile, mm;  
 $j_1$  – factor for the calculation of average stress-strain curve descending branch;  
 $j_2$  – parameter for the calculation of average stress-strain curve descending branch;  
 $k$  – initial secant elasticity modulus and secant elasticity modulus at peak strain ratio of concrete;  
 $k_1$  – first constant of confined concrete model;  
 $k_2$  – second constant of confined concrete model;  
 $k_3$  – parameter defining descending branch of confined concrete model;  
 $k_b$  – local buckling coefficient;  
 $k_{red}$  – reduction factor;  
 $k_s$  – strain ratio;  
 $K_c$  – ratio of the second stress invariant on the tensile meridian to that on the compressive meridian;  
 $L$  – length of element, mm;  
 $m$  – number of lateral initial geometrical imperfection half-waves;  
 $M$  – external bending moment, kNm;  
 $n$  – number of longitudinal initial geometrical imperfection half-waves;  
 $n_k$  – stress-strain curve knee sharpness factor;  
 $N_{cr,ex}$  – experimental critical load, kN;  
 $N_{cr,Liang}$  – theoretical critical buckling load, kN;  
 $N_u$  – ultimate strength, kN;  
 $N_{u,ex}$  – experimental ultimate strength, kN;  
 $p$  – ledge width of steel profile, mm;  
 $p_h$  – hydrostatic pressure, MPa;  
 $q$  – von Mises equivalent effective stress, MPa;  
 $R$  – width-to-thickness ratio parameter;  
 $t$  – thickness of steel panel, mm;  
 $u_t$  – tensile displacement of concrete, m;  
 $u_{t0}$  – displacement corresponding to complete loss of concrete tensile resistance, m;  
 $v$  – distance between beam end and support plate, mm;  
 $w$  – lateral deflection of steel panel, mm;  
 $w_f$  – panel area width with tensile residual stresses, mm;  
 $W$  – full beam width including steel ledges, mm;  
 $x$  – lateral coordinate of steel panel, mm;  
 $x_{pl}$  – distance between beam end and loading plate, mm;  
 $y$  – longitudinal coordinate of steel panel, mm;  
 $y_{sg}$  – strain gauge coordinate from beam top, mm;

$\alpha$  – stress ratio between opposite sides of steel panel edge;  
 $\alpha_m$  – factor depending on boundary conditions of steel panel and method of manufacturing;  
 $\beta_c$  – factor for taking into account effects of confinement for ductility of concrete;  
 $\varepsilon$  – flow potential eccentricity;  
 $\varepsilon'_{cc}$  – compressive strain at compressive strength of confined concrete;  
 $\varepsilon_c$  – compressive strain of concrete;  
 $\varepsilon_{ct}$  – concrete strain at cracking;  
 $\varepsilon_{cu,1}$  – ultimate compressive strain of concrete;  
 $\varepsilon_{c,1}$  – concrete strain at peak stress;  
 $\varepsilon_i$  – layer strain;  
 $\varepsilon_{pym}$  – strain at stress difference value, MPa;  
 $\varepsilon_s$  – strain of steel;  
 $\varepsilon_{tu}$  – ultimate tensile strain of concrete;  
 $\varepsilon_u$  – strain corresponding to ultimate strength of steel;  
 $\varepsilon_{u,1}$  – strain corresponding to the onset of ultimate stress range of steel panel;  
 $\varepsilon_{u,2}$  – strain corresponding to the end of ultimate stress range of steel panel;  
 $\varepsilon_y$  – yield strain of steel;  
 $\varepsilon_{ym}$  – yield strain of panel with residual stresses;  
 $\eta$  – compressive concrete strain and concrete strain at peak stress ratio;  
 $\lambda$  – parameter accounting for the compressive properties of concrete;  
 $\lambda_p$  – compact–non-compact slenderness limit;  
 $\lambda_r$  – non-compact–slender slenderness limit;  
 $\nu$  – Poisson's ratio of steel;  
 $\sigma_{0.7}$  – secant yield strength of steel, MPa;  
 $\sigma_1$  – average edge stress of steel panel, MPa;  
 $\sigma_c$  – compressive stress of concrete, MPa;  
 $\sigma_{c,cr}$  – compressive concrete stress at the critical buckling strain of steel, MPa;  
 $\sigma_{cr}$  – critical buckling stress of steel panel, MPa;  
 $\sigma_{cr,b}$  – compressed beam flange critical buckling stress, MPa;  
 $\sigma_{cr,c}$  – column panel critical buckling stress, MPa;  
 $\sigma_{cr,ex}$  – experimental critical buckling stress of steel panel, MPa;  
 $\sigma_{cr,imp}$  – critical buckling stress of imperfect steel panel, MPa;  
 $\sigma_p$  – post-local buckling reserve stress, MPa;  
 $\sigma_{r,comp}$  – compressive residual stress, MPa;  
 $\sigma_{r,tens}$  – tensile residual stress, MPa;  
 $\sigma_s$  – stress of steel, MPa;  
 $\sigma_{t0}$  – tensile strength of concrete, Pa;  
 $\sigma_u$  – ultimate stress of steel, MPa;  
 $\sigma_{u,b}$  – compressed beam flange ultimate stress, MPa;  
 $\sigma_{u,c}$  – column panel ultimate stress, MPa;  
 $\sigma_{u,c,red}$  – reduced ultimate stress of steel panel, MPa;  
 $\psi$  – dilation angle, °;  
 $\omega$  – initial geometrical imperfection value, mm;  
 $\omega_0$  – initial geometrical imperfection amplitude, mm;

$(EA)_i$  – axial stiffness sum of different materials of a layer;  
 $[E]$  – stiffness matrix of cross section, mm;  
 $\{F\}$  – load vector;  
 $\{\varepsilon\}$  – vector of deformations.

## ABBREVIATIONS

*AISC* – American Institute of Steel Construction;  
*ANSI* – American National Standards Institute;  
*C3D8R* – 8-node 3D element with reduced integration;  
*CAN/CSA* – a standard developed by the Canadian Standards Association;  
*CDP* – concrete damaged plasticity (model);  
*CEB-FIP MC* – Euro-international Committee for Concrete & International Federation for Prestressing, Model Code for Concrete Structures;  
*CFSST* – concrete-filled square steel tube/tubular;  
*CFST* – concrete-filled steel tube/tubular;  
*EE* – embodied energy;  
*EN* – Euronorm;  
*FE* – finite element;  
*FEM* – finite element method;  
*HSQ* – Hedlunds Svetsade Q-balk (in Swedish);  
*IP* – integration point;  
*ISO* – International Organization for Standardization;  
*LVDT* – linear variable displacement transducer;  
*PE* – polyethylene;  
*PBA* – performance-based analysis;  
*RC* – reinforced concrete;  
*RUCFSST* – rubberized concrete-filled square steel tubular;  
*S4R* – 4-node 2D reduced integration shell element;  
*SG* – strain gauge;  
*T3D2* – 2-node linear displacement element;  
*W* – column specimen type with polyethylene film between steel and concrete;  
*WO* – column specimen type without polyethylene film between steel and concrete.



## LIST OF FIGURES

- Fig. 1.1.** Stress-strain model of concrete according to Eurocode 2 [26]  
**Fig. 1.2.** Types of confinement: a) active b) passive. Illustration of Johansson and Akesson [41]  
**Fig. 1.3.** Stress-strain models of concrete confined by shear reinforcement proposed by: a) Kent and Park [45] b) Mander et al. [58]  
**Fig. 1.4.** Combined stress-strain model of confined concrete used by Liang [49]  
**Fig. 1.5.** Cross-sections of columns analysed by Huang et al.  
**Fig. 1.6.** Equivalent uniaxial stress-strain curve for concrete proposed by Huang et al. [38]  
**Fig. 1.7.** Scheme of initial geometrical imperfections proposed by Wright  
**Fig. 1.8.** Scheme of residual stresses proposed by Uy [87]  
**Fig. 1.9.** Residual stress model of Shi et al. [78]: a) for closed composite sections b) for partially encased steel sections  
**Fig. 1.10.** Modified stress-strain model of steel: a) stress development b) stress-strain curves  
**Fig. 1.11.** Results of Liang et al. [53] research: a)  $w/\sigma_1$ – $w/t$  curves of steel panels b) critical stress to yield strength ratio and  $b/t$  ratio dependencies of steel panels  
**Fig. 2.1.** a) Scheme of the column specimens b) view of the column  
**Fig. 2.2.** a) Scheme of the column test b) setup of the column test  
**Fig. 2.3.** Experimental column post-buckling shapes  
**Fig. 2.4.** Load-shortening curves of the columns: a) 1-W, 1-WO, 2-W and 2-WO b) 3-W, 3.1-WO, 3.2-WO, 4-W and 4-WO c) 5-W, 5-WO and 6-W d) 7-W, 7-WO, 8-W and 8-WO  
**Fig. 2.5.** Load-web displacement curve of the column 3.2-WO  
**Fig. 2.6.** Load-strain curves of column 3.2-WO  
**Fig. 2.7.** Steel-concrete beam specimen: a) side view b) section A-A  
**Fig. 2.8.** Cross-section schemes of experimental beams: a) stiffened b) unstiffened  
**Fig. 2.9.** View of experimental beams prior to concrete casting  
**Fig. 2.10.** Flexural beam test: a) scheme b) section A-A  
**Fig. 2.11.** Experimental setup of the flexural beam test  
**Fig. 2.12.** Experimental post-buckling shapes of beams  
**Fig. 2.13.** Bending moment-deflection curves of the experimental beams  
**Fig. 2.14.** Bending moment-strain curves of the beam: a) B1 b) B2 c) B3 d) B4  
**Fig. 3.1.** Material model of: a) structural steel with and without residual stresses according to Song et al. [82] b) concrete according to Eurocode 2 [26]  
**Fig. 3.2.** Tensile post-cracking stress-displacement behaviour of concrete  
**Fig. 3.3.** Column model assembly with scaled initial imperfections: a) isometric corner view b) isometric view of the symmetry plane c) detail 'A'  
**Fig. 3.4.** Beam model assembly with scaled initial imperfections: a) left side isometric view b) right side isometric view  
**Fig. 3.5.** FE load-shortening curves of the columns: a) 1-WO, 2-WO, 3.1-WO and 4-WO b) 5-WO, 6-W, 7-WO and 8-WO  
**Fig. 3.6.** Integration points in finite elements models

**Fig. 3.7.** Column 2-WO steel-concrete separation at the ultimate load stage

**Fig. 3.8.** Ultimate load stage normal stress distributions in column 2-WO flange

**Fig. 3.9.** Column 2-WO steel stress (MPa) distributions at outer integration points: a) longitudinal stress at the ultimate load; b) longitudinal stress at 0.02 strain; c) von Mises stress at the ultimate load; d) von Mises stress at 0.02 strain

**Fig. 3.10.** Normal stress development in the flange of column 2-WO

**Fig. 3.11.** Average normal stress-strain curves of column flanges

**Fig. 3.12.**  $w/\sigma_1$ -  $w/t$  curves of column flanges

**Fig. 3.13.** Resisted load-strain dependencies of column 2-WO

**Fig. 3.14.** Bending moment-deflection curve of beam B3-1

**Fig. 3.15.** Beam B3-1 top flange normal stress distributions at the load corresponding to the maximum effective area of the flange

**Fig. 3.16.** Normal stress development in top flange of the beam B3-1

**Fig. 3.17.** Normal stress development of beam B3-1: a) web b) concrete core

**Fig. 3.18.** Normal stress distribution in beam B3-1 at loading step 8

**Fig. 3.19.** Beam B3-1 Von Mises stress (MPa) distributions (outer steel integration points) at the maximum top flange effective area

**Fig. 3.20.** Beam B3-1 normal stress (MPa) distributions (outer steel integration points) at the maximum top flange effective area

**Fig. 3.21.** Beam B3-1 Von Mises stress (MPa) distributions (outer steel integration points) at the maximum bending moment

**Fig. 3.22.** Beam B3-1 normal stress (MPa) distributions (outer steel integration points) at the maximum bending moment

**Fig. 3.23.** Beam B3-1 steel-concrete separation at the ultimate bending moment

**Fig. 3.24.** Displacements at the critical cross-section of beam B3-1

**Fig. 3.25.** Average normal stress-strain curves of beam B3-1 top flange

**Fig. 3.26.** Average normal stress-strain curves of beam B4-1 top flange

**Fig. 3.27.** Average top flange stress-strain curves of the beams

**Fig. 3.28.** Proposed average normal stress-strain model for compressed steel panels

**Fig. 3.29.** Column critical stress- $b/t$  ratio results and proposed curves

**Fig. 3.30.** Column ultimate stress- $b/t$  ratio results and proposed curves

**Fig. 3.31.** Beam critical stress- $b/t$  ratio results and proposed curves

**Fig. 3.32.** Beam ultimate stress- $b/t$  ratio results and proposed curves

**Fig. 3.33.** Algorithm of the calculations via the iterative layer method

**Fig. 3.34.** Material model of confined concrete according to Liang [49]

**Fig. 4.1.** Comparison of column ultimate strength results

**Fig. 4.2.** Critical stress results

**Fig. 4.3.** Idealised average normal stress-strain curves of column flanges ( $f_y=370$  MPa)

**Fig. 4.4.** Idealised average top flange stress-strain curves of beams

**Fig. 4.5.** Bending moment-deflection curves of the experimental beams: a) B1-1 b) B2-1 c) B3-1 d) B4-1

**Fig. 4.6.** Maximum bending moments of the beams obtained via the experimental, numerical and iterative layer methods

## LIST OF TABLES

**Table 2.1.** Column concrete properties

**Table 2.2.** Column steel properties

**Table 2.3.** Dimensions and material properties of the column specimens

**Table 2.4.** Experimental results of columns

**Table 2.5.** Beam concrete strength

**Table 2.6.** Beam concrete elastic modulus

**Table 2.7.** Beam steel properties

**Table 2.8.** Beam reinforcement properties

**Table 2.9.** Dimensions and material properties of the beam specimens

**Table 2.10.** Dimensions of the experimental scheme

**Table 4.1.** Experimental and theoretical local and post-local buckling results of the columns

**Table 4.2.** Comparison of experimental and theoretical local and post-local buckling results of the columns

**Table 4.3.** Comparison of experimental, numerical and theoretical ultimate strength results of the columns

**Table 4.4.** Dimensions and material properties of the beam models

**Table 4.5.** Development of the bending moment, top flange effective width, average concrete normal stress and reinforcement stress in the beam B3-1 at the different loading steps

## INTRODUCTION

### Relevance of the research

Composite steel-concrete structures are used to combine the advantages of steel and concrete structures. Such structures have an increased stiffness and fire resistance compared to that of steel structures and are more slender than concrete structures. The closed section steel profile also works as a formwork for the infill concrete, thus increasing the speed of construction.

Relatively thick profiles with low width-to-thickness ratios are simple to design as this kind of cross-section may reach the full plastic resistance. However, in some cases, the width-to-thickness ratios of steel cross-sections may be high because thinner steel panels tend to cost less. In this case, the steel profile acts more as a formwork and has a smaller contribution to the overall resistance of the composite cross-section.

Steel profiles with high width-to-thickness ratios are susceptible to local buckling, and the design procedures of such regular steel sections are well known. In this case, designers usually calculate the effective cross-sectional areas unaffected by local buckling. However, local buckling in composite structures is less severe compared to local buckling in regular steel sections because, due to the restriction provided by the concrete core, steel panels can only buckle in the outward direction.

Some of the globally used design codes, such as EN 1994-1-1, feature no specific design rules and expressions for steel-concrete cross-sections. As a consequence, the same design methods and expressions of the regular non-composite steel cross-sections are used for the steel parts of composite cross-sections. In this case, the resistance of the steel profile in the composite steel-concrete cross-section is underestimated. It leads to the non-economic design of the steel profile.

Although some research regarding the local buckling behaviour of steel-concrete cross-sections was carried out by other researchers previously, the idealised design models were only created for the cases of concentric and eccentric loading of composite structures. Specific local buckling models were not created for the case of bending. Thus, there are no guidelines on how to evaluate the local buckling in steel-concrete beams.

Furthermore, the currently available models usually consist of calculating the critical buckling stress of the steel panel which is related to the onset of the local buckling and the effective cross-sectional area at the ultimate load stage. However, the exact effective cross-sectional area or the average normal stress state as a function of strain is usually not described. It is necessary as the strength of the steel panel is reduced after the ultimate strength has been reached. What is more, such expressions of other authors are difficult to apply for the iterative calculation methods of steel-concrete structures.

Therefore, in order to design steel-concrete structures economically and to fully understand the local buckling behaviour of this type of structures, the average normal stress state as a function of strain needs to be described, and analytical expressions need to be proposed.

## **Scope of the work**

Welded thin-walled concrete-filled steel stub columns and beams are analysed in this work. The main object of this research is the local buckling phenomena in such structures.

## **Aim of the thesis**

The aim of the thesis is to create the average normal stress-strain model of the compressed steel panels in thin-walled concrete-filled steel structures evaluating the effect of local buckling and to apply it in order to obtain the moment-deflection relationships of thin-walled concrete-filled steel beams.

## **Objectives of the thesis**

1. To carry out the literature review about thin-walled steel structures and the mechanical properties of confined concrete.
2. To carry out compression tests on composite stub columns and flexural tests on composite beams.
3. To create finite element models of thin-walled composite stub columns and beams and to obtain the average normal stress-strain curves of compressed flanges.
4. To create the average normal-stress strain model for compressed steel flanges in concrete-filled thin-walled steel structures.
5. To obtain the moment-deflection curves of composite beams via the iterative layer method, while incorporating the created average normal stress-strain model.

## **Methods of research**

1. Experimental compressive testing of columns and flexural testing of beams by using a hydraulic press of the 500 tons capacity. Strain gauges and linear variable displacement transducers are used for the strain and displacement measuring, respectively.
2. Theoretical methods for the critical buckling stress, ultimate stress and effective width calculation. Iterative layer method for the beam bending moment-deflection analysis.
3. Numerical analysis via the finite element software *Abaqus*.

## **Scientific novelty**

In accordance with the obtained experimental and numerical results of thin-walled welded concrete-filled steel structures, a new analytical model for the calculation of the average normal stress state as a function of strain has been proposed for compressed steel panels in steel-concrete columns and beams.

## **Practical value of the research findings**

The proposed analytical model for the development of the average normal stress of compressed steel panels in composite structures can be used for the iterative calculation methods in order to obtain the axial load-shortening or moment-deflection curves of thin-walled welded concrete-filled steel structures. The proposed critical buckling stress and ultimate stress expressions can also be used for the manual calculation of the critical load and ultimate strength of such columns. In this way, the strength loss of the structure due to local buckling can be evaluated.

## **Statements presented for the defence**

1. The proposed analytical model for the development of compressed steel panel average normal stress as a function of strain is valid to use in the iterative calculation methods to obtain the load-axial shortening or moment-deflection curves of steel-concrete composite structures.
2. Compressed steel panels of composite structures having small or no initial imperfections have a higher ultimate stress, but the stress reduction in the post-ultimate range is more sudden, while the steel panels of composite structures with significant initial imperfections are denoted by lower ultimate stress, but the stress reduction is more gradual in the post-ultimate range. The stress differences due to the initial imperfections are diminished at high strains.

## **Publication of the thesis results**

Five scientific publications on the topic of the thesis have been published: two articles in the journals indexed on *Clarivate Analytics Web of Science*, one article in a journal indexed on other international databases, and two articles in the proceedings of international conferences.

## **Structure of the thesis**

This doctoral thesis consists of the introduction, four chapters, general conclusions, a list of the literature sources and a list of scientific articles on the dissertation topic. The volume of the thesis is 142 pages. 69 numbered mathematical expressions, 53 figures and 15 tables were used in the text of the thesis. 101 sources of the literature were cited.

## I. REVIEW OF THE LATEST RESEARCH

### 1.1. Advantages and practical use of composite steel-concrete structures

Composite concrete-filled steel columns and beams are a relatively old type of structures. However, until this day, this type of structures has been used in the modern buildings of various types: industrial, residential, commercial, etc. Composite steel-concrete structures combine the positive qualities of both materials. This type of structures, just like the regular steel structures, can be assembled quickly in the building site by using bolts or on-site welds. However, the concrete has to be cast-in-situ as well, thus slowing the pace of construction. On the other hand, the steel profile acts as a formwork. Therefore, additional formworks are not required, which is an advantage compared to the regular concrete structures. Thus, the advantage of rapid and economical construction can be utilised by the composite steel-concrete structures. As for the design of this type of structures, it is driven by the limited material resources, environmental impacts and technological competition which demands lightweight, low cost and high performance structures [50].

While slender thin-walled concrete-filled steel columns are less common than those that feature compact cross-sections, local buckling may also need to be considered in special occasions, such as concrete-filled steel tubular (CFST) piles, where the wall thickness reduces gradually in time due to corrosion [47]. The effects of corrosion were investigated by Zhang *et al.* [100]. It was found that the ultimate and critical buckling loads of the most corroded steel H-beam specimens decreased by up to 18.9% and 21.4%, respectively. In some cases, the strength failure was changed by the stability failure due to corrosion.

It is important to note that different kinds of waste materials may be utilised in steel-concrete structures. An experimental campaign on the compressive behaviour of rubberized concrete-filled square steel tubular (RUCFSST) columns was carried out by Duarte *et al.* [18]. In this research, regular fine and coarse concrete aggregates were partially replaced with tyre rubber aggregates. In addition to utilising the hazardous material, the ductility of such rubberised concrete-filled columns was increased as well. However, a slight decrease of stiffness and ultimate resistance was observed. Furthermore, the sustainability of RUCFSST columns was discussed by Duarte *et al.* [19]. The sustainability of RUCFSST columns was compared to that of normal aggregate concrete-filled square steel tubular (CFSST) columns and regular reinforced concrete (RC) columns. The mechanical performance of all specimens was similar. Thus, the cross-section of the RC column was significantly larger. It was found that the embodied energy (EE) of the RC columns was 30% higher, mainly due to the larger cross-section. The RC column had the lowest thermal transmittance coefficient due to the largest cross-section height. However, due to the highest exposed area, it also had the highest heat losses and heat gains. Finally, it was found that the total energy of RUCFSST and CFSST columns was 25% lower compared to the RC column in the assumed 50-year life span.

The concrete core of composite steel-concrete structures is less susceptible to high temperatures than the steel profile and is thus able to maintain the compressive resistance better. This concrete core can also be reinforced in order to increase the

resistance of the structure more. The fire design principles of composite steel-concrete structures are presented in part 1–2 of Eurocode 4 [30]. However, only the main fire design principles are described in this code, and the application of the presented principles for the calculation requires profound and extensive knowledge about the subject. Therefore, the simplified fire design method for steel-concrete columns based on the principles of Eurocode 4 was proposed by Wang [90]. The proposed method includes the design of protected composite beams, as well as those that are unprotected. By using the simple expressions, the reduced squash load and rigidity can be found at an increased temperature. The aforementioned values can then be used to obtain the buckling resistance of the structure under fire conditions. Compared to the results obtained by using the expressions and principles of Eurocode 4 part 1–2 directly, the accuracy of the proposed method was found to be in the range of  $\pm 10\%$ .

## 1.2. Compressive behaviour of concrete in composite steel-concrete structures

Various stress-strain models of concrete were created in the modern times. One of the more commonly used models is presented in Eurocode 2 [26]. This model is valid for non-confined concrete elements. The general shape and the characteristic points of this model are shown in Fig 1.1.

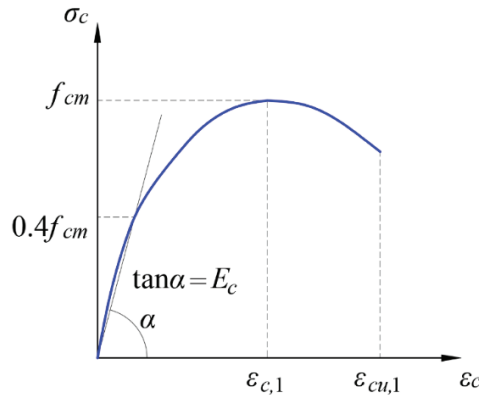


**Fig. 1.1.** Stress-strain model of concrete according to Eurocode 2 [26]

In this model, the elasticity modulus  $E_c$  of concrete is set as the secant value at 40% of the mean value of concrete cylinder compressive strength  $f_{cm}$ . The cylinder compressive strength of concrete is reached at the strain  $\varepsilon_{c,1}$ . From this strain, the strength of concrete reduces until the ultimate compressive strain value  $\varepsilon_{cu,1}$  is reached when concrete fails under compression. Concrete stresses can be calculated by using the following Expression (1.1) of Eurocode 2 [26]:

$$\sigma_c = \frac{f_{cm} (k\eta - \eta^2)}{1 + (k-2)\eta} \quad (1.1)$$

where:  $\varepsilon_c$  is the compressive strain of concrete;  $\varepsilon_{c,1}$  is the concrete strain at peak stress;  $\eta$  and  $k$  are the coefficients which can be calculated according to Eurocode 2 [26] by using Expressions (1.2) and (1.3), respectively.



$$\eta = \frac{\varepsilon_c}{\varepsilon_{c,l}} \quad (1.2)$$

$$k = \frac{1.05E_c\varepsilon_c}{f_{cm}} \quad (1.3)$$

It is well known that the stress-strain behaviour of concrete is different when the confining pressures are present. The main principles of concrete confinement were described by Johansson and Akesson [41]. The confining pressure may have one of the two following types: active or passive. The active confining pressure is caused by compressing the concrete element with external loads. On the other hand, passive confinement may be caused by other structural elements surrounding the concrete. The difference between the two types of confinement is presented schematically in Fig. 1.2.

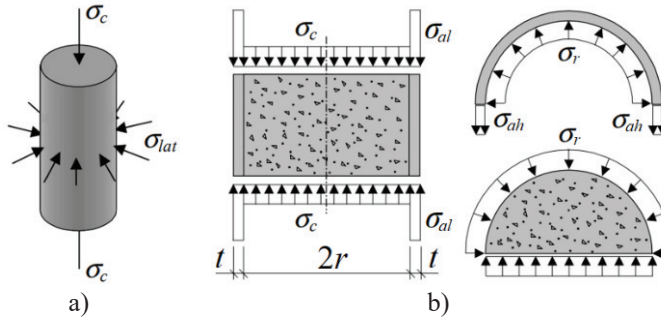


**Fig. 1.2.** Types of confinement: a) active; b) passive. Illustration of Johansson and Akesson [41]

One of the passive confinement examples is the pressure to concrete provided by the steel profile in concrete-filled steel structures. In this case, when the structure is gradually loaded, the passive confinement caused by the steel profile is variable. In the initial loading stage, the Poisson's ratio of steel is higher than that of concrete. Therefore, when the column is loaded with a small load, the lateral deformations of steel are higher than the deformations of concrete. Thus, no confinement is present in this initial stage. At higher loads, significant nonlinear strains of concrete develop, and the lateral strains of concrete reach the lateral strain values of steel. At this stage, the steel profile confines the concrete core in the lateral direction. This type of confinement allows concrete to deform significantly more in the longitudinal direction without sudden failure. The confinement may also increase the ultimate strength of concrete. However, the distinction is made between the circular and rectangular concrete-filled sections when evaluating the possible increase of concrete strength.

The early confined concrete models were created in order to evaluate the confinement effect due to the passive pressure caused by the shear reinforcement. One of the first confined concrete models for this kind of structures was proposed by Kent and Park [45]. It was proved that the confining pressure caused by the rectangular or square reinforcement hoops did not lead to any significant increase of the concrete strength. Therefore, the ultimate stress was assumed to be the same as that of non-

confined concrete, while the ductility was increased in the descending branch of the proposed stress-strain model.

An alternative confined concrete stress-strain model was later proposed by Mander *et al.* [58]. The proposed model was based on the previous experimental tests of full scale circular, rectangular and square columns carried out by Mander *et al.* [59]. It was found that the concrete strength increase may be significant when the transversal reinforcement ratio is high. When using this model, the confining pressure in the lateral directions of the cross section may be calculated by using the parameters of the transverse reinforcement and the confinement effectiveness coefficient. The latter coefficient is used to define the effectively confined concrete core due to the arching action caused by the shear reinforcement between the longitudinal bars [58]. By using the calculated values of the confining pressure, the strength and the full stress-strain curve of concrete may be obtained. The schemes of the models of concrete confined by the shear reinforcement are presented in Fig. 1.3.

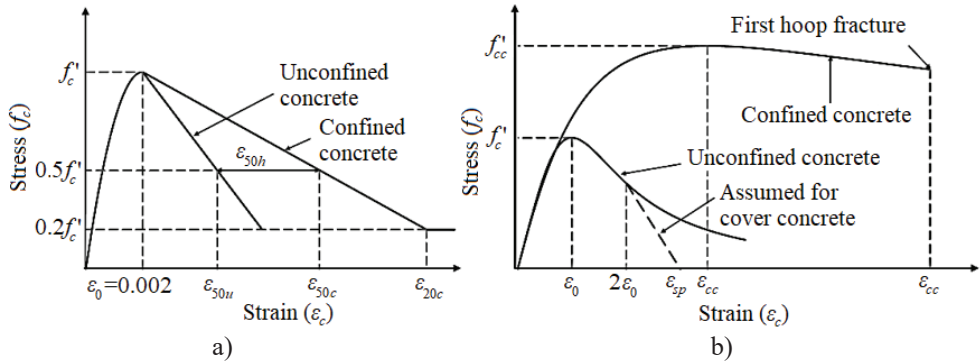


**Fig. 1.3.** Stress-strain models of concrete confined by shear reinforcement proposed by: a) Kent and Park [45]; b) Mander *et al.* [58]

Stress-strain models were also created for concrete confined by a steel profile. One of such models was proposed by Tomii and Sakino [85]. This model is widely used and is applicable for structures under axial compression, as well as bending. It assumes that the strength increase of concrete is not significant, while the ductility is increased substantially.

In order to analyse the behaviour of thin-walled concrete-filled steel structures, a combination of different confined concrete models was used by Liang [49]. The general shape of the aforementioned combined model is shown in Fig. 1.4.

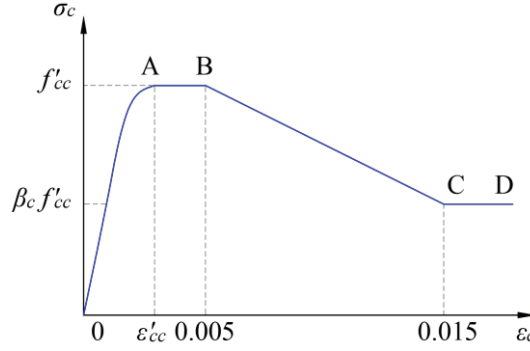


**Fig. 1.4.** Combined stress-strain model of confined concrete used by Liang [49]

In this model, the initial compressive part 0A of the curve was modelled using the formulas of Mander *et al.* [58]. Therefore, the longitudinal compressive concrete stress was calculated by using the following Expression:

$$\sigma_c = \frac{f'_{cc} \lambda \left( \varepsilon_c / \varepsilon'_{cc} \right)}{\lambda - 1 + \left( \varepsilon_c / \varepsilon'_{cc} \right)^\lambda} \quad (1.4)$$

where:  $f'_{cc}$  is the compressive strength of the confined concrete assumed equal to that of the non-confined concrete for rectangular cross-sections;  $\varepsilon_c$  is the longitudinal compressive concrete strain;  $\varepsilon'_{cc}$  is the strain at stress  $f'_{cc}$  calculated from Expression (1.5);  $\lambda$  is the parameter accounting for the compressive properties of concrete calculated from Expression (1.6).

$$\varepsilon'_{cc} = \begin{cases} 0.002 & \text{for } f'_{cc} \leq 28 \\ 0.002 + \frac{f'_{cc} - 28}{54000} & \text{for } 28 < f'_{cc} \leq 82 \\ 0.003 & \text{for } f'_{cc} > 82 \end{cases} \quad (1.5)$$

$$\lambda = \frac{E_c}{E_c - (f'_{cc} / \varepsilon'_{cc})} \quad (1.6)$$

The stress values in the ranges AB, BC and CD were based on Expression (1.7) proposed by Tomii and Sakino [85]:

$$\sigma_c = \begin{cases} f'_{cc} & \text{for } \varepsilon'_c < \varepsilon_c \leq 0.005 \\ \beta_c f'_{cc} + 100(0.015 - \varepsilon_c)(f'_{cc} - \beta_c f'_{cc}) & \text{for } 0.005 < \varepsilon_c \leq 0.015 \\ \beta_c f'_{cc} & \text{for } \varepsilon_c > 0.015 \end{cases} \quad (1.7)$$

where:  $\beta_c$  is the factor taking into account the effects of confinement for the ductility of concrete depending on the width-to-thickness ratio ( $B_s/t$ ) of the beam. In this case, value  $B_s$  is taken as the larger dimension of the outer width  $B$  (disregarding the ledges)

and the outer height  $H$ . Based on the experimental results of Tomii and Sakino [85],  $\beta_c$  is calculated from Expression (1.8).

$$\beta_c = \begin{cases} 1.0 & \text{for } \frac{B_s}{t} \leq 24 \\ 1.5 - \frac{B_s}{48t} & \text{for } 24 < \frac{B_s}{t} \leq 48 \\ 0.5 & \text{for } \frac{B_s}{t} > 48 \end{cases} \quad (1.8)$$

It is generally assumed that the passive confinement provided by the rectangular steel cross-section does not increase the compressive strength of concrete effectively. Therefore, the compressive strength of confined concrete  $f'_{cc}$  is assumed to be equal to strength  $f_{cm}$  of non-confined concrete. On the other hand, the confinement increases the ductility of concrete significantly. Therefore, concrete is able to sustain the maximum stress across a wide interval of strains.

Significant research about the confinement of concrete-filled steel columns was carried out by Schneider [76]. It was proved that the ductility of circular columns was significantly higher compared to square and rectangular columns. Only the columns having width-to-thickness ratios less than 20 exhibited strain hardening characteristics.

Confinement effects for the behaviour of concrete-filled steel columns having width-to-thickness ratios in the range 24–48 were investigated via the finite element (FE) analysis and experimental tests by Chen *et al.* [15]. It was found that the strength of such columns decreased rapidly once the ultimate strength had been reached. This strength reduction was observed mainly due to the strength decrease of the concrete core. Thus, according to the authors of the aforementioned research, concrete confinement was not very significant at this stage. Different confined concrete models were summarized by Bhartiya *et al.* [8]. Twenty-two circular composite steel-concrete columns were tested experimentally. A new refined confined concrete model considering the influence of diameter-to-thickness and length-to-diameter ratios was proposed.

The confinement effects for concrete-filled steel columns were also analysed in the research of Huang *et al.* [38]. Three cross-section types of experimental columns were modelled by using the FE software: circular CU sections, square SU sections and square SS sections with reinforcing ties in the tube corners. The aforementioned cross-sections are presented in Fig. 1.5. The authors of the research worked on the basis of the confined concrete model created by Mander *et al.* [58]. The general shape of the model proposed by Huang *et al.* [38] is presented in Fig. 1.6, where the descending branch is modelled by using the idealised linear dependency.

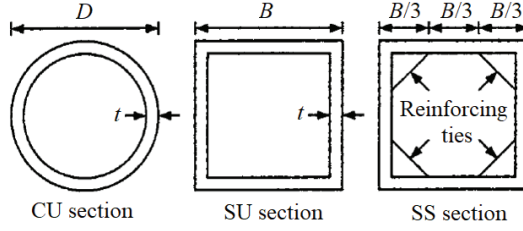


**Fig. 1.5.** Cross-sections of columns analysed by Huang *et al.* [38]

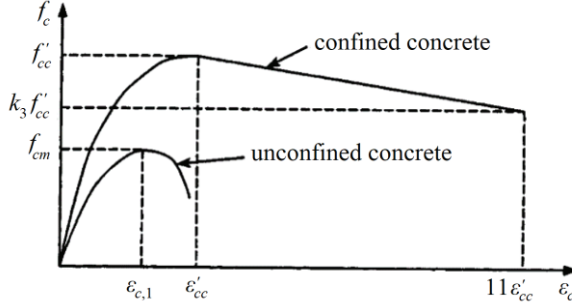


**Fig. 1.6.** Equivalent uniaxial stress-strain curve for concrete proposed by Huang *et al.* [38]

In this model, the strength of confined concrete and the corresponding strain can be calculated from Expressions (1.9) and (1.10), respectively.

$$f'_{cc} = f_{cm} + k_1 f_l \quad (1.9)$$

$$\varepsilon'_{cc} = \varepsilon_{c,1} \left( 1 + k_2 \frac{f_l}{\varepsilon_{c,1}} \right) \quad (1.10)$$

where:  $f_l$  is the confining pressure;  $k_1$  and  $k_2$  are constants obtained from the experimental data of Richart *et al.* [74] which are equal to 4.1 and 20.5, respectively.

According to the findings of Huang *et al.* [38], the confining pressure was not significant for the SU type cross-sections having width-to-thickness ratios in the range  $29.2 \leq B/t \leq 150$ . Therefore, in this range, concrete strength can be assumed to be the same as that of non-confined concrete. On the other hand, the ratio between the confining pressure and the yield strength of steel for columns having width-to-thickness ratios in the range  $17 \leq B/t < 29.2$  can be calculated from the following empirical Expression:

$$f_l / f_y = 0.055048 - 0.001885(B/t) \quad (1.11)$$

where:  $f_y$  is the yield strength of steel.

Parameter  $k_3$  defining the descending branch of the confined concrete stress-strain model can be assumed as 0.4 in the range  $70 \leq B/t \leq 150$ . Expression (1.12) was proposed for parameter  $k_3$  calculation in the width-to-thickness range  $17 \leq B/t < 70$ :

$$k_3 = 0.000178(B/t)^2 - 0.02492(B/t) + 1.2722 \quad (1.12)$$

The confinement effect was the most significant, and local buckling was found to be unlikely for CU type cross-sections. Significant values of confining pressure were provided by steel profiles with diameter-to-thickness ratios in the range  $0 \leq B/t \leq 150$ . Empirical expressions were proposed for the calculation of  $f_l/f_y$  and  $k_3$ . It was also found that the reinforcing ties in the columns of the SS cross-section were effective in preventing local buckling. The use of ties also led to more significant confining pressure values than that of the SU type columns. However, confining pressure was still less significant than the confining pressure provided by the CU type of cross-section. As a general conclusion, it was found that the confining pressure and the material degradation parameter  $k_3$  decreases with an increase of the width-to-thickness or the diameter-to-thickness ratio.

Different width-to-thickness ratios of steel profiles to provide the significant confinement effects have also been reported by other authors. For example, it was reported by Hajjar and Gourley [35] that the effects of confinement are only significant for columns having  $B/t$  ratios lower than 40. It was also found in the research of Martinavičius *et al.* [62] that the concrete infill increased the flexural resistance of concrete-filled steel HSQ beams by more than 50% compared to the regular steel HSQ beams of the same cross-section. Due to concrete confinement, the failure of such composite beams was very ductile.

### 1.3. Initial imperfections of steel profiles

The production of steel cross-sections is a set of complex procedures. Initially, the steel panels of required dimensions need to be cut. Usually, two alternative cutting procedures are distinguished: cutting by flame and mechanical cutting. According to Song *et al.* [82], different levels of residual stresses may be introduced into the steel elements depending on the type of the cutting procedure. Once the steel panels have been cut, separate parts need to be assembled to form the closed rectangular sections. For this purpose, the procedure of welding is usually used. As a consequence, significant tensile residual stresses are introduced into the welding areas according to Uy [86]. On the other hand, compressive residual stresses develop in the areas further from the welds in order to maintain the stress equilibrium in every cross-section. Geometrical imperfections are also likely to be introduced during the welding, transportation and on-site assembly of the produced structures. As a consequence of the production and construction complexity, the production of perfect structures is highly unlikely. Therefore, the initial geometrical imperfections and residual stresses have to be considered during the analysis of steel and steel-concrete structures, as it may reduce the buckling stress, ultimate strength and stiffness of steel panels significantly. Such effects were significant in the research of Liang and Uy [48]. However, there are various ways to evaluate the initial imperfections.

#### 1.3.1. Geometrical imperfections

The initial geometrical imperfections of real structures may have any form, as it is a result of production, transportation and on-site assembly of structures. However, in the design stage, the exact shape of imperfections is not known yet. Thus, ideally,

the initial geometrical imperfections assumed for analysis should consider the most severe case for buckling.

One of the methods to evaluate the initial imperfections is to use the local buckling shapes obtained from the linear buckling analysis. This method was used by Liang and Uy [48]. The first local buckling shape of every plate analysed with amplitudes varying from  $0.1t$  to  $0.5t$  was assumed as the initial geometrical imperfection in this research. Liang and Uy [48] found that the increase of the geometrical imperfection amplitude led to a decrease of the critical buckling stress, the ultimate buckling stress, and post-buckling stiffness. It was also found that the post-local buckling reserve strength was 55% of the ultimate strength of the plate ( $b/t=100$ ) with  $0.1t$  imperfection amplitude, compared to 28% of a plate with  $0.5t$  imperfection amplitude. However,  $0.1t$  was selected as the base imperfection amplitude for the design methods proposed in this research. Finally, it is also important to note that the use of this imperfection evaluation method is limited when steel-concrete structures are analysed as linear buckling analysis does not allow to evaluate the steel-concrete contact. This method is only suitable when the behaviour of the steel plate in the concrete-filled steel structure is simplified as the behaviour of a plain clamped steel plate, as it was the case in the research of Liang and Uy [48].

Alternatively, imperfections may be assumed to have an idealised shape. This kind of idealised initial geometrical imperfection shape model was proposed by Wright [93], and a scheme of this model is presented in Fig. 1.7.

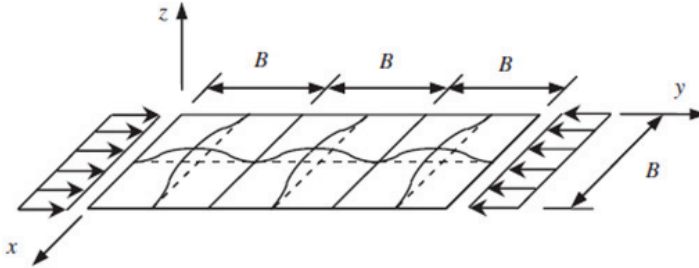


**Fig. 1.7.** Scheme of initial geometrical imperfections proposed by Wright [93]

Expression (1.13) was proposed by Wright [93] to describe this kind of shape:

$$\omega = \frac{\omega_0}{4} \left( 1 - \cos \frac{2m\pi x}{B} \right) \left( 1 - \cos \frac{2n\pi y}{L} \right) \quad (1.13)$$

where:  $x$  and  $y$  are the respective lateral and longitudinal coordinates of a steel panel, when assuming the bottom column corner as the reference point;  $B$  and  $L$  are the width and length of the steel panel, respectively;  $m$  and  $n$  are the numbers of the lateral and longitudinal imperfection half-waves, respectively;  $\omega_0$  is the geometrical imperfection amplitude.

The imperfections of the already existing structures may be measured by using manual tools, such as dial gauges mounted on the precision rail. This method was used in the research of McAnallen *et al.* [65]. Alternatively, more advanced methods like high-precision 3D laser scanning can be applied. The aforementioned method was used by Biscaya *et al.* [9] and Huang *et al.* [39].



It is important to note that geometrical imperfection amplitudes in the research of Liang and Uy [48] were relative to the thickness of the analysed plates, thus setting the base value as  $0.1t$ . On the other hand, part 1–5 of Eurocode 3 [28] assumes imperfection amplitudes to be relative to panel widths. The imperfection amplitude adopted by this code is set as  $B/200$ . For example, the maximum absolute value of the imperfection amplitude of the closed-section column measured by Huang *et al.* [39] was 0.94 mm or  $B/266$ . If the imperfection amplitude value was set as  $0.1t$  in the research of Huang *et al.* [39], the amplitude of 0.5 mm would be obtained. Thus, it is important to note that the amplitudes relative to the width and the thickness of the panel may be significantly different. Finally, it is also obvious that imperfection amplitude values as high as  $B/200$  are also very likely in real structures.

### 1.3.2. Residual stresses

Residual stresses are mainly introduced into steel panels during the procedure of welding, and the strains caused by welding can be measured by using strain gauges. This type of strain measurement was carried out by Uy [86]. Strains of columns caused by welding were measured before and after the welding of cross-sections. Three strain gauges were used on the same steel panel. In this way, the level of residual stresses was assessed. It was found that tensile residual stresses equal to the yield strength of steel were introduced into the welding areas, while the compressive stresses were observed in the mid-panel areas between the welds. As a consequence, assuming the stress equilibrium of the cross-sections, Uy [86] was then able to obtain the widths of the initial tensile and compressive fields. The aforementioned residual stress results and the results of other researchers were summarized by Uy [87]. It was found that the maximum compressive residual stress based on the available published data was 30% of the yield strength. An idealised residual stress model was proposed. The scheme of this model is shown in Fig. 1.8.

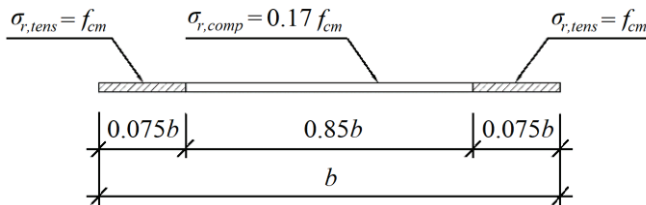


**Fig. 1.8.** Scheme of residual stresses proposed by Uy [87]

A more accurate idealised model for square concrete-filled and partially encased steel columns was proposed by Shi *et al.* [78]. The schemes of this model are presented in Fig. 1.9. In this model, the smooth transition between the tensile and compressive stress is considered. This kind of idealised models may be directly used in the finite element analysis. Different residual stress distribution models for hot-rolled and welded cross sections have also been proposed by Young [97], Szalai and Papp [84], Barth and White [7], Bjorhovde *et al.* [10] and summarised by Rossi *et al.* [75]. In-depth residual stress analysis of welded steel columns was also carried out by Chen and Chang [17]. More recently, an improved residual stress model for welded square sections was developed by Somodi and Kövesdi [80].



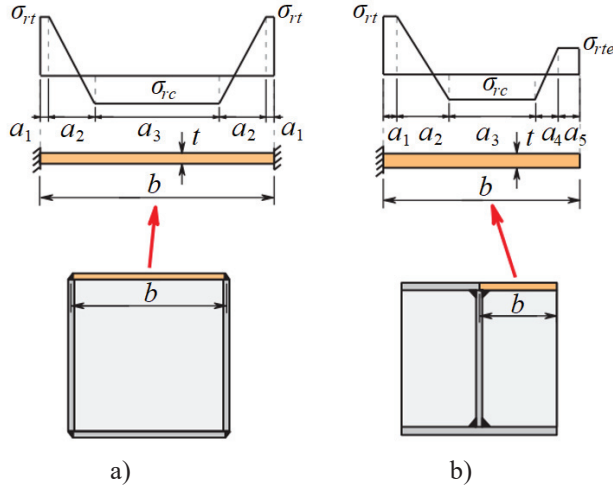


**Fig. 1.9.** Residual stress model of Shi *et al.* [78]: a) for closed composite sections; b) for partially encased steel sections

Alternatively, the effects of residual stresses can be considered by modifying the stress-strain curve of the analysed steel. This kind of approach was used in the research of Song *et al.* [82] where a modified stress-strain curve of steel was proposed. The scheme of the proposed model is shown in Fig. 1.10. Mechanical cut and flame cut plates were distinguished as separate cases in the research of Song *et al.* [82]. However, only the case of mechanical cut plates is discussed further, as this type of plates was used in the current research. According to the proposed residual stress model, several stress development and redistribution steps are distinguished. The initial stiffness (step a1) of the compressed steel panel with residual stresses is the same as that of the perfect panel with no initial imperfections. At higher stresses (step a2), the middle area of the steel panel starts to yield. This leads to the early decrease of stiffness. Therefore, the full yield strength of the steel panel is reached at a significantly higher strain level (step a3). However, it is important to note that residual stresses have no influence on the yield strength of steel.

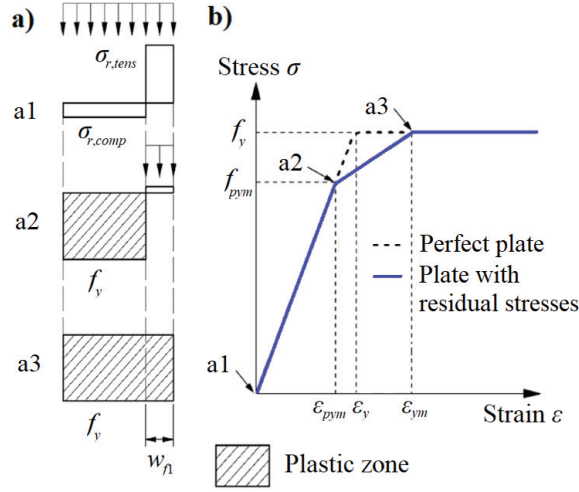


**Fig. 1.10.** Modified stress-strain model of steel: a) stress development; b) stress-strain curves

The stress difference value  $f_{pym}$  may be calculated as proposed by Song *et al.* [82]:

$$f_{pym} = f_y - \sigma_{r,comp} \quad (1.14)$$

where:  $\sigma_{r,comp}$  is the compressive residual stress which can be calculated from Expression (1.15) proposed by Uy [87].

$$\sigma_{r,comp} = 0.17 f_y \quad (1.15)$$

The strain value  $\epsilon_{pym}$  corresponding to stress  $f_{pym}$  and yield strain  $\epsilon_{ym}$  can be calculated from Expressions (1.16) and (1.17) proposed by Song *et al.* [82], respectively.

$$\epsilon_{pym} = \frac{(f_y - \sigma_{r,comp})}{E_s} \quad (1.16)$$

where:  $E_s$  is the elasticity modulus of steel.

$$\epsilon_{ym} = \epsilon_{pym} + \frac{\sigma_{r,comp} b_h}{E_s w_{f1}} \quad (1.17)$$

where:  $b_h$  is the half-width of the steel flange;  $w_{f1}$  is the panel area width with tensile residual stresses which can be calculated from Expression (1.18) proposed by Uy [87].

$$w_{f1} = 0.075b \quad (1.18)$$

Alternative modified stress-strain model for steel was proposed by Ramberg and Osgood [72]. Steel strain in this model can be calculated by using the following Expression:

$$\varepsilon_s = \frac{\sigma_s}{E_s} \left( 1 + \frac{3}{7} \left( \frac{\sigma_s}{\sigma_{0.7}} \right)^{n_k} \right) \quad (1.19)$$

where:  $\sigma_s$  is the steel stress;  $\sigma_{0.7}$  is the secant yield strength, which is the stress corresponding to  $E_{0.7}=0.7E_s$ ;  $n_k$  is the stress-strain curve knee sharpness factor which can be assumed as 25 according to Liang and Uy [48].

#### 1.4. Local buckling behaviour of steel structures

Steel panels of cross-sections with high width-to-thickness ratios are likely to lose the local stability even if the global stability of the member is maintained. The stress corresponding to the onset of local buckling is called the critical local buckling stress. This is often also referred to as the bifurcation point. Local buckling phenomena have a different nature than that of the global buckling of a member. There is no sudden loss of resistance in this case. Once the critical local buckling stress has been reached, the stress redistribution starts. Once local buckling starts in square or rectangular steel profiles, stiffness begins to decrease in the mid-panel areas, and stresses gradually concentrate in the corner regions. Finally, the failure of such a member is governed by the yielding of the non-buckled corner regions. This area unaffected by the local buckling is usually referred to as the effective cross-sectional area, and most of the models used to evaluate the local buckling behaviour are based on this effective area concept. This concept is also adopted in part 1–5 of Eurocode 3 [28]. According to part 1–1 of Eurocode 3 [27], steel members are classified into classes 1–4. The panels of classes 1 and 2 are usually referred to as compact, while classes 3 and 4 are referred to as non-compact and slender, respectively. According to part 1–1 of Eurocode 3 [27], only the slender members of class 4 are susceptible to local buckling. According to this code, the slenderness of separate panels is calculated, thus evaluating the effective areas. As a consequence, the sum of those separate effective areas is considered to be the effective cross-sectional area of the member.

Multiple catastrophic bridge failures happened in the 19<sup>th</sup> and the 20<sup>th</sup> centuries due to having not taken into account the effects of local buckling [4]. While, in statically indeterminate frames, the local buckling of the cross-section may cause load redistribution, in statically determinate frames, instability may occur. Therefore, it is fundamentally important to understand the slenderness of separate panels of the designed structural element.

It was observed by Wael [71] that the compact–non-compact ( $\lambda_p$ ) and non-compact–slender ( $\lambda_r$ ) class limits have significantly different values in different design codes. In some cases, the aforementioned limits are conservative, while, in other cases, it leads to the cross-section capacity overestimation. What is more, such codes as Eurocode 3 [27] and CAN/CSA S16-01 [14] do not take into account the web-flange interaction while evaluating the slenderness limits. This kind of interaction is only covered in ANSI/AISC 360-05 [2]. It was found by Wael [71] that the slenderness limits of the flanges and the webs of the beams are greatly affected by the width-to-height ratio of the entire cross-section. As a consequence, the new slenderness limits taking into account the web-flange interaction were proposed. Furthermore, expressions for the calculation of the local buckling coefficient  $k$  values

for flexural members taking into account the web-flange interaction were proposed by Mina and Schafer [77]. Multiple expressions were derived for different cross-section types from the AISC shapes database. Furthermore, the flange-induced buckling of plate girders fabricated from high strength steel was analysed by Nascimento *et al.* [67]. It was found that the web slenderness limits provided in part 1–5 of Eurocode 3 to prevent flange-induced buckling yield very conservative results for this type of structures.

### 1.5. Local buckling behaviour of steel-concrete structures

The same design method based on the effective area concept is adopted by part 1–5 of Eurocode 3 [28] and Eurocode 4 [29]. However, this model does not take into account the additional constraints for thin-walled steel panels provided by concrete. Since the steel profile is filled with concrete, the panels are not allowed to buckle towards the inside of the cross-section. Therefore, the critical buckling stress and the effective cross-sectional area is increased significantly compared to that of the regular steel cross-section.

Despite the limitations of some design codes, the local buckling behaviour of steel-concrete structures was analysed by various researchers. Ten compressive tests of thin-walled concrete-filled welded columns were carried out by Uy [86]. Two types of specimens were tested: columns where only the steel profile was loaded, and columns loaded as composite sections. In this research, the tested specimens had width-to-thickness ratios  $b/t$  in the range of 40–100. During the course of the experimental tests, the load-shortening curves of the columns were obtained. Critical buckling stresses were obtained as well by tracking the reduction of stiffness from the load-average strain results of the column specimens. The effective widths of the steel panels were obtained by calculating the steel profile strength contribution as a proportion of strength of the perfect unbuckled steel profile with stresses equal to the yield strength.

The research was later continued by Uy [87]. A set of 30 thin-walled welded concrete-filled steel cross-sections was tested. Concrete strengths were in the range between 32 and 50 MPa. Width-to-thickness ratios of the analysed columns were in the range of 40–100. The columns were tested under concentric and eccentric loads. In this case, the specimens were loaded as composite cross-sections. Additional beam specimens were also tested by using four-point bending. When using the same methods as used in the previous research, the critical buckling stresses and effective widths were obtained. The finite strip method was used afterwards to create combined flexural and compressive models incorporating the local buckling behaviour and residual stresses. However, the initial geometrical imperfections were not taken into account. Nevertheless, the results of this model showed good agreement with the experimental results.

The later research of Uy [88] included experimental tests of concrete-filled thin-walled and partially concrete encased welded I-sections. Concrete-filled columns had  $b/t$  ratios in the range of 120–180. Partially encased I-sections had flange outstands with outstand-to-thickness ratios in the range of 20–35. Only the steel edges of the columns were loaded. Steel-concrete contact surfaces were covered with grease in

order to ensure that no bond could be developed. Based on the experimental results and the use of the finite strip method, simplified curves were proposed in order to obtain the critical buckling stress depending on the steel panel  $b/t$  ratio, the yield strength of steel, and the level of residual stresses. Having calculated the critical buckling stress, the effective width can then be calculated from the expression of Winter [92]. This expression was later modified by Bradford *et al.* [12] to take into account the residual stresses and initial imperfections:

$$b_{eff} = b \cdot \alpha_m \sqrt{\frac{\sigma_{cr}}{f_y}} \quad (1.20)$$

where:  $b_{eff}$  is the effective width of the steel panel;  $\sigma_{cr}$  is the critical buckling stress;  $\alpha_m$  is the factor depending on the boundary conditions of the panel and the method of manufacturing which can be assumed as 0.65 for heavily welded plates supported on two longitudinal edges [12].

An iterative method for calculating the global resistance of concrete-filled steel columns also taking into account the effects of local buckling was presented by Vrcelj and Uy [89]. The resistance of a slender column with local buckling effects was expressed as the percentage of the global column resistance disregarding the local buckling for steels with various yield strengths. Rectangular concrete-filled slender circular steel columns with unequal wall thickness were analysed by Fu *et al.* [33]. Even though the cross-sections were compact, local buckling was observed at the top and at the mid height of specimens in the more advanced loading stages.

The effects of concrete-filled steel column pre-stressing were analysed by Richard Liew and Xiong [73]. This type of steel profile pre-stressing may occur due to the construction stage loads from the upper floors prior to concrete casting. A design method based on the modified approach of part 1-1 of Eurocode 4 [29] was developed to evaluate the axial resistance of such columns while considering the preloading effect. Experimentally analysed columns were mainly non-slender. Thus, local buckling was only observed in the post-ultimate load range.

The local buckling behaviour of H beams partially encased with concrete was analysed by Song *et al.* [82]. In this research, columns were reinforced with transverse links between flange tips. Detailed finite element models were created and analysed. The initial geometrical imperfections and residual stresses were introduced into the aforementioned models. It was found by Song *et al.* [82] that the inward geometrical imperfections of the H columns led to a significant increase of the post-buckling strength, while the outward imperfections led to a less significant decrease of the post-buckling strength. Expressions for the calculation of critical stresses of flanges were proposed. Additional formulas were also proposed in order to obtain the full stress-strain curves of the flanges undergoing local buckling.

Expressions for the calculation of effective width ratios for steel panels in composite steel-concrete columns were proposed by Yamaki [95]. Significant research was also carried out by Liang and Uy [48]. In this research, the behaviour of steel plates in welded steel box columns filled with concrete was analysed via the finite element method and compared against the experimental data of other authors. It was assumed during finite element analysis that the behaviour of a steel plate in a

composite column is the same as that of a regular rectangular steel plate clamped on all four edges. This kind of simplification can be explained by the fact that the restraint provided by concrete allows the plate edges to rotate in one direction only. Thus, buckling waves can only form towards the outside of the cross-section. Therefore, the behaviour of a clamped steel plate is indeed similar to the behaviour of a steel plate in a concrete-filled steel section. In this research, the analysed square plates had width-to-thickness ratios in the range of 30–110. The base geometrical imperfection amplitude value was set as  $0.1t$ . The effects of residual stresses were taken into account by using the stress-strain model of Ramberg and Osgood [72]. As a result of research by Liang and Uy [48], effective width expressions were proposed as follows:

$$b_{eff} = \begin{cases} 0.675b \left( \frac{\sigma_{cr}}{f_y} \right)^{1/3} & \text{for } \sigma_{cr} \leq f_y \\ 0.915b \left( \frac{\sigma_{cr}}{\sigma_{cr} + f_y} \right)^{1/3} & \text{for } \sigma_{cr} > f_y \end{cases} \quad (1.21)$$

The critical buckling stress of the perfect plate with no imperfections may be calculated by using the following Expression [13]:

$$\sigma_{cr} = \frac{k \cdot \pi^2 \cdot E_s}{12(1-\nu^2) \left( \frac{b}{t} \right)^2} \quad (1.22)$$

where:  $k$  is the local buckling coefficient, assumed equal to 9.81 [51];  $\nu$  is the Poisson's ratio of steel, assumed as 0.3 [27].

The aforementioned effective width expressions were adopted in the research of Jiang *et al.* [40], where the behaviour of combined rolled and welded cross-sections was analysed. The proposed analytical model results were compared against the experimental flexural test results, and relatively good agreement was obtained. The same expressions were also used for the numerical fibre element method for welded steel-concrete columns proposed by Liang *et al.* [54] incorporating the effects of local buckling and concrete confinement. When the local buckling effects were ignored, the ultimate strength of the analysed square column  $306 \times 306 \times 3$  mm was overestimated by 10%. A fibre element model was also developed and used by Zubydan and Elsabbagh [101] to analyse the cyclic behaviour of steel-concrete beam-columns.

The further research of Liang *et al.* [53] considered the behaviour of steel plates in composite columns under concentric and eccentric compression. In this research, the following expression for the calculation of the critical stress of the plate with imperfections was proposed:

$$\sigma_{cr,imp} = f_y \left( a_1 + a_2 \left( \frac{b}{t} \right) + a_3 \left( \frac{b}{t} \right)^2 + a_4 \left( \frac{b}{t} \right)^3 \right) \quad (1.23)$$

where:  $a_1$ ,  $a_2$ ,  $a_3$  and  $a_4$  are the constant coefficients depending on the load eccentricity. The aforementioned coefficients are equal to 0.5507, 0.005132,  $-9.869 \cdot 10^{-5}$  and  $1.198 \cdot 10^{-7}$ , respectively, when the load is concentric.

It was noted by Liang *et al.* [53] that bifurcation points of steel plates cannot be observed in the load–lateral displacement curves due to the existence of geometrical imperfections. Therefore, a new method for determining the critical stresses of imperfect plates was proposed. The lateral deflection to average the edge stress ratio  $w/\sigma_1$  is plotted against the lateral deflection to the plate thickness ratio  $w/t$ . The minimum value of  $w/\sigma_1$  can be assumed as the inflection point corresponding to the critical buckling stress. Such curves are presented in Fig. 1.11 a). In this graph, the  $\alpha$  value represents the stress ratio between the opposite sides of the steel panel edge, where  $\alpha=1$  corresponds to the case of concentric load. The curves of the critical stress to yield strength ratio as a function of  $b/t$  ratio of the analysed plates are shown in Fig. 1.11 b). It is obvious that slender steel plates under concentric compression start to buckle under relatively low stresses compared to compact plates under eccentric compression.

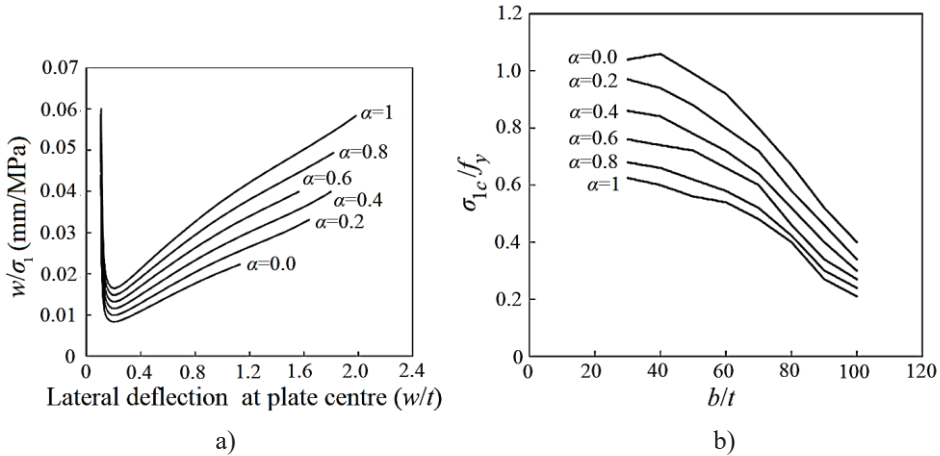


**Fig. 1.11.** Results of Liang *et al.* [53] research: a)  $w/\sigma_1$ – $w/t$  curves of steel panels; b) critical stress to yield strength ratio and  $b/t$  ratio dependencies of steel panels

Alternative critical buckling stress expressions for eccentrically and concentrically loaded plates were also proposed by Long *et al.* [56]. The theoretical calculations of this research were based on the energy method. Limit panel length-to-width and width-to-thickness ratios were proposed in order to avoid the local buckling prior to reaching the yield stress.

A formula for the calculation of the ultimate stresses of steel plates in concrete-filled steel columns was proposed by Liang *et al.* [53]:

$$\sigma_u = f_y \left( c_1 + c_2 \left( \frac{b}{t} \right) + c_3 \left( \frac{b}{t} \right)^2 + c_4 \left( \frac{b}{t} \right)^3 \right) \quad (1.24)$$



where:  $c_1$ ,  $c_2$ ,  $c_3$  and  $c_4$  are the constant coefficients taking into account the load eccentricity. The aforementioned coefficients are equal to 0.5554, 0.02038,  $-3.944 \cdot 10^{-4}$  and  $1.921 \cdot 10^{-6}$ , respectively, when the load is concentric.

Therefore, according to Liang *et al.* [53], the post-local buckling reserve stress can be calculated from Expression (1.25). It was observed that this reserve is much higher for slender plates compared to those that are compact.

$$\sigma_p = \sigma_u - \sigma_{cr,imp} \quad (1.25)$$

An expression for the calculation of the ultimate stresses of steel plates in composite steel-concrete columns was also proposed by Ge and Usami [34]:

$$\sigma_u = f_y \left( \frac{1.2}{R} - \frac{0.3}{R^2} \right) \leq f_y \quad (1.26)$$

where:  $R$  is the width-to-thickness ratio parameter calculated from Expression (1.27).

$$R = \frac{b}{t} \sqrt{\frac{12(1-\nu^2)}{\pi^2 k}} \cdot \sqrt{\frac{f_y}{E_s}} \quad (1.27)$$

where:  $k$  is the local buckling coefficient, assumed as 4, when the method of Ge and Usami [34] is used.

Another method to obtain the ultimate stress of steel panels in composite steel-concrete structures was proposed by Nakai *et al.* [66]:

$$\sigma_u = f_y \left( 0.433(R-0.5)^2 - 0.831(R-0.5) + 1 \right) \quad (1.28)$$

where:  $R$  is calculated from Equation (1.27) while assuming the value of the local buckling coefficient  $k$  as 9.81.

In order to compare the results of the different methods directly, the unreduced cross-sectional area of the steel panel with the calculated ultimate stress can be converted into the effective cross-sectional area with the yield stress by using the following Expression:

$$A_{eff} = \frac{\sigma_u \cdot b \cdot t}{f_y} \quad (1.29)$$

Following the previous research, Liang developed a performance-based analysis (PBA) technique which was based on the fibre element formulations for the nonlinear analysis and performance-based design of concrete-filled steel columns with local buckling effects. The theoretical description of this method was published in a research paper of Liang [49]. The verification and application of the method was published in a separate article [52]. The proposed iterative method can be used for the load-strain and moment-curvature calculations of tubular concrete-filled columns under compression and biaxial bending. It takes into account the effects of buckling, residual stresses and geometrical imperfections. The development of the ineffective width of the steel panel between the critical stress and the ultimate stress is calculated by using the following linear interpolation Formula:



$$b_{ne} = \left( \frac{\sigma_1 - \sigma_{cr,imp}}{f_y - \sigma_{cr,imp}} \right) b_{ne,u} \quad (1.30)$$

where:  $\sigma_1$  is the average edge stress;  $b_{ne,u}$  is the maximum ineffective width calculated from Equation (1.31).

$$b_{ne,u} = b - b_{eff} \quad (1.31)$$

It is very likely that this kind of linear interpolation formula does not reflect the actual effective area development of steel panels. It was shown in the research of Song *et al.* [82] that, once the ultimate stress of the flange in the partially encased H beam has been reached, the effective area starts to decrease. Therefore, similar idealised average stress-strain curves for thin-walled panels undergoing local buckling need to be developed for the case of concrete-filled steel columns. This kind of a model would also help to understand if the maximum effective area of a steel profile is reached at the same time as the ultimate stress of concrete. This factor is very important when calculating the strength of steel-concrete columns while using the simplified manual methods.

Local buckling effects were also analysed for the case of circular concrete-filled steel columns. A series of experimental tests were conducted by Young *et al.* [11]. A simple squash load formula was proposed taking into account concrete strength enhancement and steel stress reduction due to confinement. Concrete infill effects for the local buckling behaviour of such columns were analysed via the parametric finite element study carried out by Kazemzadeh Azad and Uy [44]. It was found that concrete had a relatively small impact on the increase of the local buckling capacity of the analysed circular steel profiles.

Finally, two steel HSQ beams and two concrete-filled steel HSQ beams were experimentally tested by Martinavičius *et al.* [63]. Two pairs of different steel cross-sections were used. One steel profile was filled with concrete, while another steel profile of the same cross-section was tested as a hollow steel cross-section. It was found during the experimental campaign that the steel HSQ beams failed early due to local buckling, while the failure of concrete-filled HSQ beams was very ductile, and local buckling was prevented by concrete.

## 1.6. Other research of structural behaviour of steel-concrete structures

Multiple articles on various topics in the field of composite steel-concrete structures have been published by a number of authors. A series of experimental tests on concrete-filled stub columns, columns and beam-columns were carried out by Han *et al.* [37]. The cross-sections of the specimens had width-to-thickness ratios in the range of 20.5–36.5 and were relatively compact. A full load-strain mechanics model was developed for the calculation of such steel-concrete structures, while also taking into account the effects of confinement. The results obtained via the proposed model were in good agreement with the experimental data of more than 300 tests carried out by other researchers. Finally, the simplified mechanics model was developed for the capacity calculation of square concrete-filled steel columns.

Further research of Han [36] considered the flexural behaviour of concrete-filled steel tubes. A series of experimental tests were carried out for beams with depth-to-width-ratios in the range of 1–2 and depth-to-thickness ratios in the range of 20–50. Theoretical load-deflection curves, by taking into account the effects of confinement, were obtained and compared against the experimental data, thereby achieving good agreement. A simplified calculation method for the moment capacity of square, rectangular and circular cross-sections was developed. The results of this method were compared with the results obtained by using the methods of different design codes. It was found that the moment capacity was approximately 10% lower when using the proposed method and the method of Eurocode 4 [29], while other codes, such as AISC [3], yielded more conservative resistance values.

Recently, more and more research articles regarding concrete-filled steel sections have been based on innovative cross-sections, the use of high-strength materials and stress-strain behaviour of structures in elevated temperatures. Song *et al.* [81] carried out push-out tests on concrete-filled steel tubes (CFST). It was found that the columns with normal steel-concrete interfaces at temperatures higher than 200 °C had negligible bond strength. However, the use of expansive concrete, welding internal rings or shear studs proved to be effective in increasing the bond strength. Zhang *et al.* [99] analysed the behaviour of steel circular concrete-filled reinforced stub columns. An experimental and numerical study was carried out. Based on the obtained results, a method for the prediction of temperature and resistance for this type of structural members was proposed. Analytical post-fire load-strain simulations based on the fibre element method, incorporating the effects of local buckling of concrete-filled steel columns were carried out by Kamil *et al.* [42]. A simplified expression for strength calculation was proposed. Furthermore, the interaction between the local and global buckling behaviour in structures exposed to fire was analysed via the fibre element method by Kamil *et al.* [43].

The local buckling behaviour of partially encased and concrete-filled columns fabricated from normal and high strength steels was investigated by Song *et al.* [83]. Simplified finite element models taking into account the effects of geometrical imperfections and residual stresses were created and analysed. Local buckling stress, local buckling strain and effective width expressions were proposed. It was also suggested that the local buckling effects have to be taken into account for plates having slenderness higher than 0.42, which is 30% lower than the limit adopted by Eurocode 4 [29]. Three cases were analysed by Song *et al.* [83] via finite element analysis. In the first case, the whole composite steel-concrete cross-section was loaded, assuming the perfectly linear concrete stress-strain behaviour and disregarding the steel-concrete bond. The second case was similar, but the nonlinear concrete behaviour was assumed. In the third case, only the steel profile was loaded, and concrete was acting as a rigid medium only. It was consequently found that there was no significant difference between the stress-strain behaviour of steel panels when comparing all three cases.

Concrete-filled and partially encased by concrete welded high strength steel columns were analysed by Huang *et al.* [39]. Sixteen specimens of 690 MPa yield strength were experimentally tested. Parametric finite element analysis was carried

out. The critical buckling stress and ultimate stress values were obtained. New slenderness limits were proposed. During the experimental campaign, it was found that the concrete infill enhanced the ultimate strength of steel columns by up to 60% and 35% for concrete-filled and concrete-encased cross-sections, respectively. A full-scale experimental study on the composite behaviour of ultra-high strength concrete-filled high-strength steel columns under axial compression was carried out by Xiong *et al.* [94], which included testing 14 specimens overall.

Fibre element based numerical analysis of square ultra-high strength concrete-filled steel columns under compression and biaxial bending was carried out by Phan [69] *et al.* The new Brent's method algorithm was developed to adjust the neutral axis position and to iterate the curvature in order to maintain the moment and force equilibrium. It was suggested that the steel contribution factor should be maintained above 0.3 in order to ensure the required ductility of columns.

A model for local buckling of CFST columns with binding bars was proposed by Yue-Ling and Zeng [57]. The effects of longitudinal and horizontal spacing were taken into account. It was found that longitudinal spacing had a more significant impact on the critical buckling stress. The diameter of the binding bars was also found to be a significant factor for the cases when the bar spacing was small. The behaviour of thin-walled dodecagonal section double skin concrete-filled steel tubes was analysed by Chen *et al.* [16]. Octagonal thin-walled cross-sections filled with concrete were investigated by Lim and Eom [55]. Circular tubed steel-reinforced-concrete slender columns were analysed by Biao *et al.* [96]. Ahmed and Liang [1] investigated structural responses of thin-walled round-ended concrete-filled steel tubular columns under eccentric loads by using the fibre element method. This kind of cross-sections requires complex analysis as the flat portions of steel profiles are susceptible to local buckling, while the rounded edge parts are able to confine the concrete effectively. In addition to fibre element analysis, simplified design expressions were also proposed. Finite element analysis of such structures was carried out by Zhang *et al.* [98].

## 1.7. Conclusions of Chapter One

1. Various confined concrete models were created by the different authors. There is a general consensus that the confinement caused by steel hollow rectangular cross-sections does not increase the concrete strength effectively when compared to circular cross-sections. On the other hand, some strength increase was reported for rectangular cross-sections having width-to-thickness ratios in the range of 17–29.2. It was also found that the ductility of concrete is increased for the columns having width-to-thickness ratios in the range of 17–150. However, different maximum slenderness ratios of steel profiles causing significant confinement effects were reported by other authors.
2. The models used for the calculation of local buckling of steel cross-sections suffer from various shortcomings. There is no integrity in the compact–non-compact and non-compact–slender slenderness limits adopted by different design codes. What is more, the web–flange interaction is not considered in most cases. This kind of interaction is not taken into account, either, in the design codes for steel-concrete structures.
3. Various methods have been proposed to evaluate the ultimate strength of steel plates in concrete-filled structures. Some of the models are based on the average ultimate edge stress of plates, while other models are based on the effective width concept. However, different methods still yield comparable values of the ultimate strength.
4. Various approaches were used by a number of authors in order to evaluate the effects of geometrical imperfections. In some cases, scaled linear buckling shapes were used. However, this method is only valid to use for the analysis of clamped steel plates. In other cases, mathematical expressions were proposed in order to obtain the idealised imperfection shapes, which is a universal method. In the case of existing structure analysis, the exact imperfections can be measured manually by using dial gauges on the precision rail or by using the more advanced methods, such as high-precision 3D scanning.
5. The strains caused during the procedure of welding were measured by various authors. It was found that the tensile residual stresses equal to the yield strength of steel are caused in the welding regions. Compressive stresses with maximum values of 30% of the yield strength are caused in the mid-panel areas between the welds. Idealised residual stress distributions were proposed by a number of authors. During the design or analysis of structures, residual stresses can be taken into account when using a variety of methods. Finite element analysis allows for the direct input of the experimentally measured initial stress values. Alternatively, residual stresses can be taken into account via the use of modified stress-strain curves of steel.
6. In the scope of the literature review, expressions which could be used to obtain full average stress-strain curves of flanges of concrete-filled thin-walled welded steel beams have not been proposed. This kind of average stress-strain model for flanges undergoing local buckling could be used for the analysis of the moment-deflection behaviour of such structures.

## II. EXPERIMENTAL RESEARCH OF THIN-WALLED STEEL-CONCRETE STRUCTURES

A two-part experimental programme was carried out during this research. The first part was based on the compressive testing of thin-walled steel-concrete columns. A part of the material obtained during the experimental column campaign was published in the research articles by Martinavičius and Augonis [60], Martinavičius *et al.* [64]. The second part of the experimental programme was based on the flexural testing of thin-walled reinforced steel-concrete beams. A part of the material of the experimental beam campaign was published in a research article by Martinavičius and Augonis [61].

### 2.1. Experimental testing of concrete-filled welded steel columns

#### 2.1.1. Preparation and properties of column specimens

Sixteen rectangular steel columns with eight different cross-sections were welded from separate thin-walled steel panels. Initially, the steel panels were tack-welded, and internal bracing was provided. Subsequently, the panels were welded with full longitudinal welds. Once the welding had been finished, the internal bracing was removed. Eight stiffeners were welded at both ends of every column to avoid buckling at significantly lower loads, as mentioned in the research of Uy [88]. The scheme and a view of the column specimens are presented in Fig 2.1.

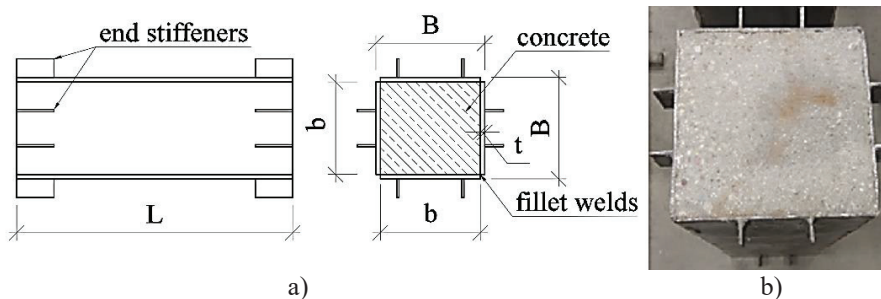


Fig. 2.1. a) Scheme of the column specimens; b) view of the column

It was decided to evaluate the influence of the steel-concrete contact conditions. Therefore, two column specimens of the same dimensions were fabricated for each type of cross-section (except for one). One specimen of each column cross-section type had a regular bond between steel and concrete, while the PE film was placed inside of another respective specimen to ensure that no bond is developed.

The concrete was poured in 2–3 batches (by using the same concrete mix) into each steel column placed in the vertical position and consolidated by using an internal electric concrete vibrator. Additionally, cubic and prism concrete specimens were casted and covered tightly with the PE film to simulate the curing conditions of the closed section composite column. Compressive testing of the columns was carried out after a 28-day period. Prior to testing, both end surfaces of each column were polished.

Two main types of column cross-sections were used: square and rectangular. The columns had different  $b/t$  and  $h/t$  ratios. Columns were grouped into ten separate

batches prior to concrete casting. Thirty cubic 100×100×100 mm specimens overall (three for each batch) were tested according to EN 12390-3 [25] to find the compressive strength values of the concrete. Ten 100×100×300 specimens were also tested according to EN 12390-13 [24] to obtain the elasticity modulus of the concrete of each batch. The results of the concrete specimens and the respective standard deviations are summarised in Table 2.1.

**Table 2.1.** Column concrete properties

Column batch	Compressive strength of first specimen $f_{c,1}$ , MPa	Compressive strength of second specimen $f_{c,2}$ , MPa	Compressive strength of third specimen $f_{c,3}$ , MPa	Average concrete compressive strength $f_{c,avg}$ , MPa	Elasticity modulus $E_c$ , GPa
1-WO	31.06	29.21	29.65	29.97±0.97	32.623
1-W	32.77	30.35	32.33	31.82±1.29	34.423
2-WO	26.98	24.19	29.19	26.79±2.51	32.176
2-W	27.36	25.07	25.35	25.93±1.25	31.469
3-W, 3.1-WO	33.54	31.51	31.26	32.10±1.25	32.204
4-W	29.18	29.23	32.83	30.41±2.10	30.597
3.2-WO, 4-WO	36.22	30.17	34.39	33.59±3.10	32.794
5-W, 5-WO	35.45	34.78	35.17	35.13±0.34	34.074
6-W	34.71	32.15	33.85	33.57±1.30	34.078
7-W, 7-WO, 8-W, 8-WO	30.43	30.84	33.71	31.66±1.79	30.474
Standard deviation of the elasticity modulus					±1.404

Five steel specimens were tested according to EN ISO 6892-1 [31] to obtain the yield strength and ultimate strength. The results and the respective standard deviations are summarized in Table 2.2. According to the specification, the elasticity modulus  $E_s$  of the steel was 210 GPa.

**Table 2.2.** Column steel properties

Steel specimen	Yield strength $f_y$ , MPa	Ultimate strength $f_u$ , MPa
SS-1	372.92	491.94
SS-2	373.40	476.68
SS-3	374.35	479.49
SS-4	367.84	476.68
SS-5	365.73	483.11
Average strength	370.85±3.82	481.58±6.37

All of the column specimens with the respective dimensions, width-to-thickness ratios and material properties are summarised in Table 2.3. The column marking consists of the cross-section number and the letters referring to the type of the steel-concrete contact. The letter W refers to the columns with the PE film placed in the steel-concrete contact zone. The letters WO refer to the columns without the PE film, i.e., to these which feature the regular steel-concrete contact.

**Table 2.3.** Dimensions and material properties of column specimens

Column marking	Inner width $b$ , mm	Inner height $h$ , mm	Thickness $t$ , mm	$b/t$	$h/t$	Length $L$ , mm	Avg. concrete strength $f_{c,avg}$ , MPa	Avg. yield strength $f_{y,avg}$ , MPa
1-WO	238.4	178.8	3.12	76.4	57.3	719.3	29.97	370.85
1-W	238.5	178.7	3.05	78.2	58.6	718.5	31.82	370.85
2-WO	237.0	237.6	3.09	76.7	76.9	718.0	26.79	370.85
2-W	238.0	237.7	3.14	75.8	75.7	719.0	25.93	370.85
3-W	198.1	198.1	3.09	64.1	64.1	598.8	32.10	370.85
3.1-WO	198.4	198.4	3.02	65.7	65.7	599.5	32.10	370.85
3.2-WO	199.0	199.6	3.10	64.2	64.4	598.3	33.59	370.85
4-W	178.6	116.9	3.15	56.7	37.1	539.0	30.41	370.85
4-WO	178.3	119.0	3.10	57.5	38.4	537.3	33.59	370.85
5-W	217.4	157.2	3.07	70.8	51.2	659.3	35.13	370.85
5-WO	218.9	158.4	3.07	71.3	51.6	659.0	35.13	370.85
6-W	178.5	179.4	2.98	59.9	60.2	539.5	33.57	370.85
7-W	158.7	158.7	3.07	51.7	51.7	479.0	31.66	370.85
7-WO	158.6	159.2	3.08	51.5	51.7	479.0	31.66	370.85
8-W	138.7	138.7	3.09	44.9	44.9	419.0	31.66	370.85
8-WO	139.2	139.5	3.06	45.5	45.6	419.0	31.66	370.85

### 2.1.2. Compressive column test setup and procedure

A hydraulic press of the 500 tons capacity was used to load the columns. The experimental scheme and the setup are presented in Fig. 2.2. The bottom part of the press is movable, while the top part acts as a support. Prior to loading, each column was centred. Three strain gauges (SG1–SG3) were glued onto one web at different heights. During the pre-testing, it was determined that the usual local buckling areas were the middle of the column or the areas that were approximately 5 cm away from the end stiffeners. Therefore, three strain gauges were glued in those areas. LVDT transducers T1 and T2 were used to measure the displacement of the press base. This displacement was initially assumed to be equal to the shortening of the column. Furthermore, to complement the results of the strain gauges, LVDT transducers T3 and T4 were used to measure the lateral displacement of the webs. Electronic equipment was used to write down and record the load, shortening, lateral web displacement, and strain results. The load controlled column testing was carried out with a load increase rate of 10 kN/s. The loading was stopped when the load resisted by the specimen decreased by at least 10% of the ultimate load.



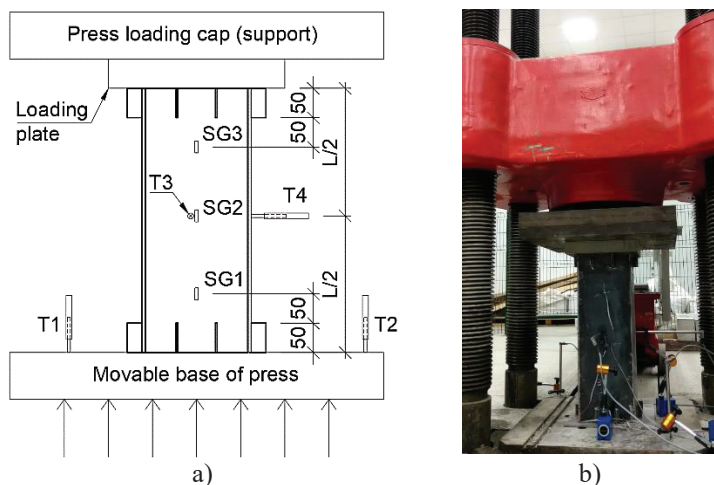


**Fig. 2.2.** a) Scheme of the column test; b) setup of the column test

### 2.1.3. Experimental results of thin-walled steel concrete columns

The typical experimental post-local buckling areas are presented in Fig. 2.3. The cross-sections where the failure occurred were in the middle of the column or 4–6 cm away from the end stiffeners in all cases. The local buckling failure of the steel profile was in some cases followed by the separation of the steel panels in the weld areas at the high values of axial shortening.



**Fig. 2.3.** Experimental column post-buckling shapes

Experimental load-shortening curves of the columns are presented in Fig. 2.4. Curves of the columns having the same cross-section (type W and WO) are plotted in the same figure by using the same colour.



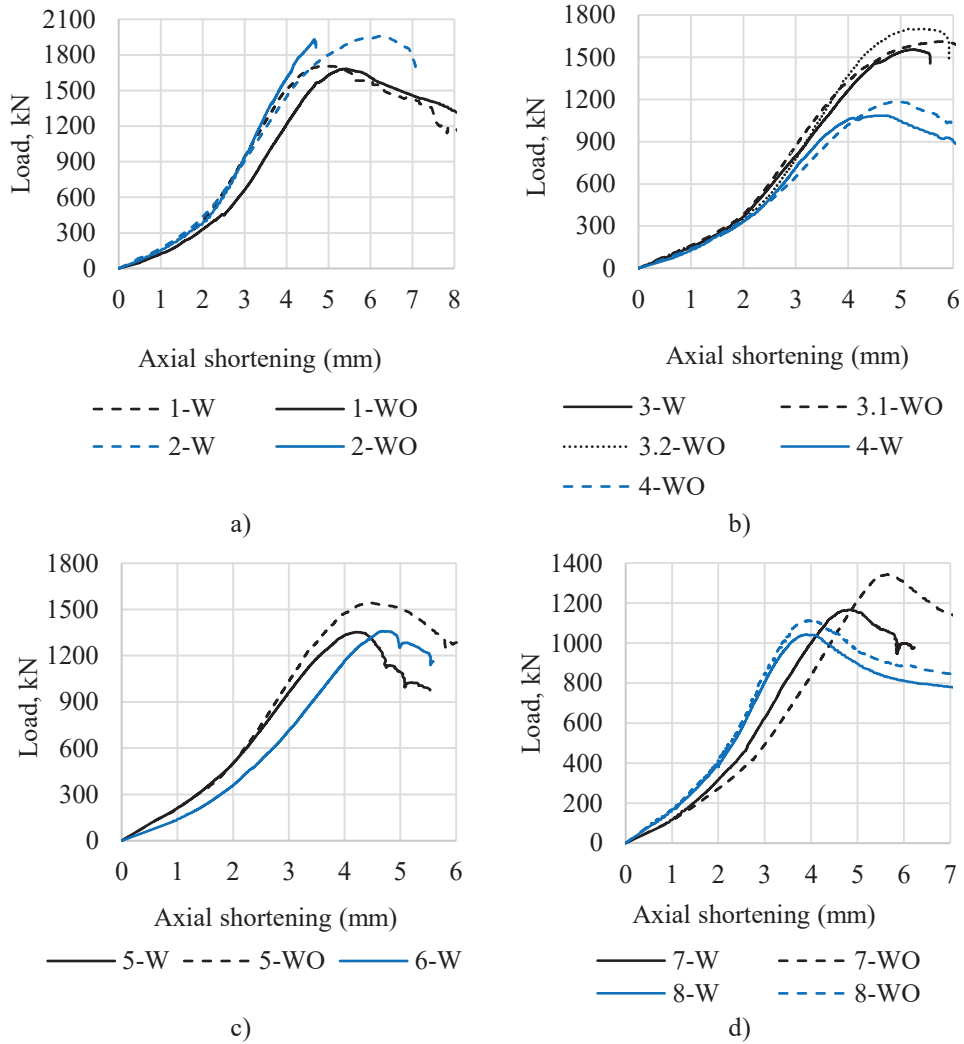


**Fig. 2.4** Load-shortening curves of the columns: a) 1-W, 1-WO, 2-W and 2-WO; b) 3-W, 3.1-WO, 3.2-WO, 4-W and 4-WO; c) 5-W, 5-WO and 6-W; d) 7-W, 7-WO, 8-W and 8-WO

It was observed that the shortening of the columns had a significantly higher value than predicted. The low initial stiffness could be expected as the loading plates have to adjust to the column surfaces. However, the low initial stiffness is normalized and becomes close to linear at a higher load. This normalised stiffness is also several times lower than the theoretically predicted linear stiffness. This type of difference was also reported in the researches of Hu *et al.* [38], Duarte [20], as well as in the research of Ellobody and Young [22]. The possible reasons suggested by Duarte [20] were as follows: small gaps between the hydraulic press, the loading plates and the loading surfaces; existence of geometrical imperfections and residual stresses; small loading eccentricities and out-of-straightness of the columns; micro cracks caused by the restrained shrinkage of the concrete due to friction between the concrete core and

the steel profile. Furthermore, even though the column end surfaces were polished, it was still difficult to achieve the ideal smoothness. Even a small protrusion of the concrete above the steel edges could lead to the concrete core being loaded first. Once the steel profile has been loaded, the concrete could already behave nonlinearly due to the concrete pre-loading effect. It would mean that the full predicted theoretical elastic stiffness could not be achieved. Due to the limitations of the equipment, only the displacement of the bottom support of the press was measured. Thus, the possible settlement of the top support could lead to the increased axial shortening values.

Load-web displacement curves were obtained for the two webs of every column. A typical curve (specifically, of column 3.2-WO) is shown in Fig. 2.5. From this curve, it is obvious that the web displacement starts to propagate more rapidly at the 700–900 kN load. It could be due to the onset of the local buckling. On the other hand, it could also be due to the onset of the nonlinear stress-strain behaviour of the concrete. Therefore, web displacement results are complementary and must be analysed together with the strain results in order to evaluate the critical buckling stress.

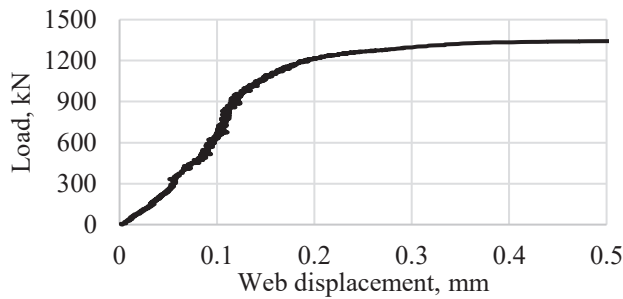


**Fig. 2.5.** Load-web displacement curve of the column 3.2-WO

The load-strain results of the column 3.2-WO strain gauges SG1, SG2 and SG3 are presented in Fig. 2.6. It can be seen that the strains stopped propagating at the specific loads at different heights of the column. This load could be associated with the onset of the local buckling. Thus, the stress corresponding to the minimum strain value can be assumed as the critical buckling stress  $\sigma_{cr,ex}$ . In this case, the lowest critical load was 700 kN for the analysed column 3.2-WO.

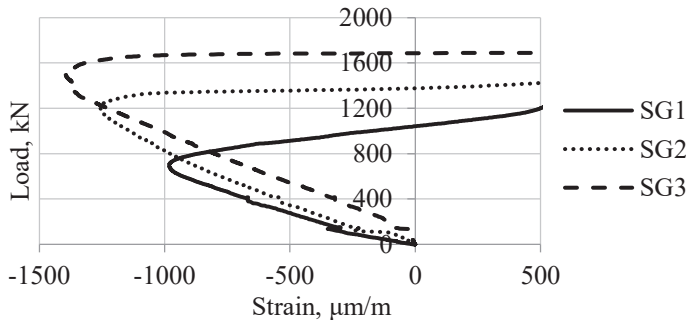


**Fig. 2.6.** Load-strain curves of column 3.2-WO

The load-strain curves of the steel webs at different heights of the column have a similar shape, but the critical loads are different. One of the reasons for this type of difference is the initial imperfections. The higher level of geometrical imperfections and residual stresses may reduce the critical load and the corresponding critical stress significantly. Variation of the initial imperfections is very likely due to the complex production of the columns and the manual welding of the thin-walled steel panels. The idealised imperfection shape model having a variable number of imperfection half-waves is shown in Fig. 1.7. On the other hand, the experimental columns may have any shape of imperfections. In the theoretical models, local buckling half-waves usually form in the same place where the initial geometrical imperfection half waves are prescribed. However, as the experimental imperfections are random, the centre of the local buckling half-wave may also form at any height of the column. Thus, the local buckling half-wave may be away from the strain gauge. This factor is important for the accuracy of the critical load measurement.

The experimental results of the columns are summarised in Table 2.4, where  $f_{y,avg}$  is the average yield strength taken from Table 2.2. The ultimate stress of the steel profile undergoing buckling is calculated by using Expression (2.1):

$$f_{u,ex} = \frac{N_{u,ex} - A_c \cdot f_{cm}}{A_s} \quad (2.1)$$

where:  $f_{cm}$  is the average cylinder strength of concrete calculated from Expression (2.2) [46];  $A_c$  is the cross-sectional area of the concrete core.

$$f_{cm} = \left( 0.76 + 0.2 \log_{10} \frac{f_{c,avg}}{19.6} \right) f_{c,avg} \quad (2.2)$$

**Table 2.4.** Experimental results of columns

Column marking	$b/t$	$h/t$	Exp. critical load $N_{cr,ex}$ , kN	Exp. ultimate load $N_{u,ex}$ , kN	Exp. critical stress $\sigma_{cr,ex}$ , MPa	Exp. ultimate stress $f_{u,ex}$ , MPa	$\sigma_{cr,ex}/f_{y,avg}$	$f_{u,ex}/f_{y,avg}$ ( $A_{eff}/A_s$ )
1-W	78.2	58.6	1350.0	1706.6	157.5	242.3	0.42	0.65
1-WO	76.4	57.3	975.0	1682.6	149.1	253.9	0.40	0.68
2-W	75.8	75.7	1400.0	1957.0	165.9	263.1	0.45	0.71
2-WO	76.7	76.9	1750.0	1930.5	228.3	246.4	0.62	0.66
3-W	64.1	64.1	600.0	1554.9	127.1	223.5	0.34	0.60
3.1-WO	65.7	65.7	600.0	1612.1	130.0	251.7	0.35	0.68
3.2-WO	64.2	64.4	700.0	1701.9	204.8	256.5	0.55	0.69
4-W	56.7	37.1	900.0	1085.3	240.2	306.2	0.65	0.83
4-WO	57.5	38.4	800.0	1184.2	192.2	328.5	0.52	0.89
5-W	70.8	51.2	750.0	1352.7	154.4	168.1	0.42	0.45
5-WO	71.3	51.6	1300.0	1543.7	210.0	244.8	0.57	0.66
6-W	59.9	60.2	950.0	1358.4	85.3	233.7	0.23	0.63
7-W	51.7	51.7	1025.0	1167.2	204.8	268.1	0.55	0.72
7-WO	51.5	51.7	1100.0	1343.2	228.9	356.4	0.62	0.96
8-W	44.9	44.9	900.0	1043.4	263.3	320.1	0.71	0.86
8-WO	45.5	45.6	1000.0	1112.0	207.9	358.6	0.56	0.97

The critical stress results showed wide stochastic scattering due to the uncertainty of the initial geometrical imperfections. Thus, some of the W type columns had a higher critical stress compared to that of the corresponding WO type column. It is known that the critical stress results are sensitive to the initial imperfections and that the higher level of imperfections may reduce the critical stress significantly. Due to the random shape of the initial imperfections, local buckling may start at a different height of the column, and the load-strain curve may be significantly different if the strain gauge is glued away from the centre of the local buckling wave. Furthermore, due to the limitations of the equipment, the strains were measured only on one web of every column, and the remaining three webs were not measured. Due to small random eccentricities, the development of the stresses may be uneven in the different webs of the same column. Finally, a higher number of strain measurement gauges is advisable for the same web. The average web strain results could be used to evaluate the critical buckling stress alternatively.

The ratios between the effective steel cross-sectional area and the full steel cross-sectional area  $A_{eff}/A_s$  were mostly higher for the WO type columns. The highest difference was 47% compared to the W type columns. The only series where the W type column had a higher  $A_{eff}/A_s$  ratio was series 2. In this case, column 2-W had a 9% higher  $A_{eff}/A_s$  ratio than column 2-WO. This could possibly be observed due to the uncertainty of the concrete strength or the different level of initial imperfections.

## 2.2. Experimental testing of concrete-filled welded steel beams

### 2.2.1. Preparation and properties of beam specimens

Four box-shaped rectangular steel beams with different cross-sections were welded from separate thin-walled steel panels. Similarly to the previously tested columns, the steel panels were initially tack-welded, while also internally bracing the beam. Full length fillet welds were then welded, and the internal bracing was removed. The scheme of the beam specimens is presented in Fig 2.7. Each beam was stiffened in the support zones, while the middle-third of every beam length was left unstiffened. The purpose of the stiffeners was to avoid the effects of shear buckling. The middle area was designed as a pure bending zone. The stiffened and unstiffened cross-section schemes of steel profiles of the composite beams are presented in Fig 2.8. The steel profiles prior to concrete casting are shown in Fig. 2.9.

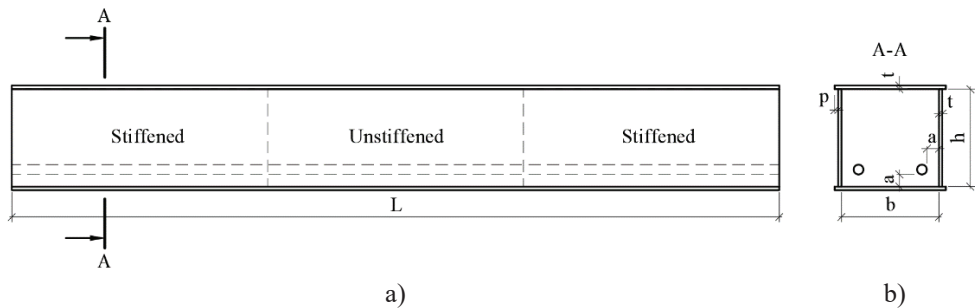


**Fig. 2.7.** Steel-concrete beam specimen: a) side view; b) section A-A

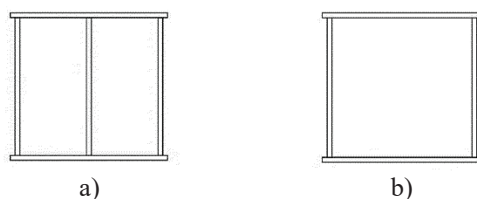


**Fig. 2.8.** Cross-section schemes of experimental beams: a) stiffened; b) unstiffened



**Fig. 2.9.** View of experimental beams prior to concrete casting

One end of each beam specimen was initially closed with a welded end plate. Two reinforcement bars of 20 mm diameter were placed inside. Prior to casting the concrete, the beams were placed in the vertical position. Concrete was then poured in 2–3 batches (by using the same concrete mix) for each beam and consolidated by using an internal electric concrete vibrator. Cubic and prism concrete specimens were also casted and covered tightly with the PE film to simulate the curing conditions of the closed section beam. The flexural testing of the beams was carried out 28 days later. Prior to testing, the open end of each beam was closed with a welded end plate.

Thirty cubic 100×100×100 mm specimens overall (6–9 for each beam) were tested according to EN 12390-3 [25] to obtain the compressive strength values of the concrete. The compressive results of the concrete specimens are summarised in Table 2.5.

**Table 2.5.** Beam concrete strength

	Beam B1	Beam B2	Beam B3	Beam B4
$f_{c,1}$ , MPa	33.46	40.86	39.41	36.32
$f_{c,2}$ , MPa	35.95	39.41	39.69	35.16
$f_{c,3}$ , MPa	33.48	40.72	39.03	36.28
$f_{c,4}$ , MPa	33.93	39.32	38.14	35.21
$f_{c,5}$ , MPa	35.51	39.96	38.83	36.14
$f_{c,6}$ , MPa	35.54	38.69	38.26	35.41
$f_{c,7}$ , MPa	33.51	—	37.88	—
$f_{c,8}$ , MPa	34.86	—	37.26	—
$f_{c,9}$ , MPa	33.61	—	37.40	—
$f_{c,avg}$ , MPa	34.43	39.83	38.43	35.75

Ten 100×100×300 concrete specimens overall (2–3 for each beam) were tested according to EN 12390-13 [24] to obtain the elasticity modulus of the concrete. The results are summarised in Table 2.6.

**Table 2.6.** Beam concrete elastic modulus

	Beam B1	Beam B2	Beam B3	Beam B4
$E_{c,1}$ , GPa	33.49	35.05	34.77	32.93
$E_{c,2}$ , GPa	33.73	35.57	34.85	32.86
$E_{c,3}$ , GPa	32.53	-	35.81	-
$E_{c,avg}$ , GPa	33.25	35.31	35.14	32.90

Steel panels of 3 mm and 4 mm thickness were used for the production of the beams. Three steel specimens were tested for the 3 mm panels, and three additional specimens were tested for the 4 mm panels. The dimensions of the specimens and the testing procedure were based on the rules of EN ISO 6892-1 [31]. The yield strength and the ultimate strength results are summarised in Table 2.7.

**Table 2.7.** Beam steel properties

Steel specimen	Yield strength $f_y$ , MPa	Ultimate strength $f_{us}$ , MPa
3 mm thickness		
SS-T3-1	333.26	482.82
SS-T3-2	343.81	493.15
SS-T3-3	330.50	504.54
Group average	335.86	493.50
4 mm thickness		
SS-T4-1	421.82	543.78
SS-T4-2	439.81	537.96
SS-T4-3	423.91	532.48
Group average	428.52	538.07

The reinforcement specimens were tested similarly to the structural steel specimens. Ribbed reinforcement bars of the B500B class were used in this research. The diameter of the bars was 20 mm in all cases. The yield strength and the ultimate strength results of the reinforcement are presented in Table 2.8. According to the specification, elasticity modulus  $E_{sr}$  of the steel rebars was 200 GPa.

**Table 2.8.** Beam reinforcement properties

Reinforcement specimen	Yield strength $f_{sy}$ , MPa	Ultimate strength $f_{su}$ , MPa
RS-1	581.76	684.97
RS-2	573.56	677.56
RS-3	580.21	674.30
RS-4	569.23	677.10
Group average	576.26	678.48

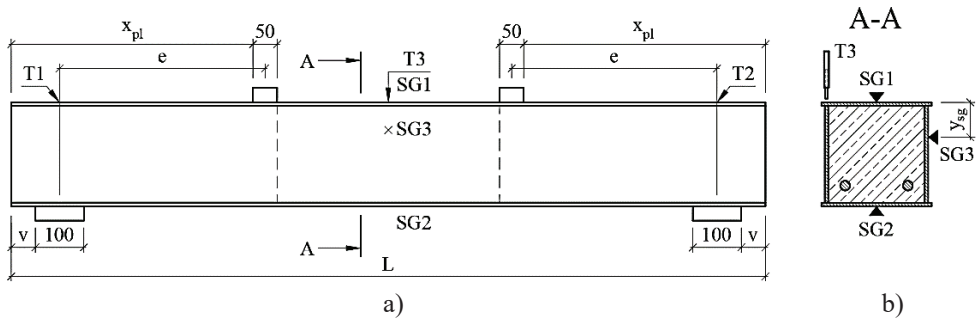
The dimensions and the material properties of the tested beam specimens are presented in Table 2.9. The marking of the dimensions is as shown in Fig. 2.10.

**Table 2.9.** Dimensions and material properties of beam specimens

Beam marking	$b$ , mm	$h$ , mm	$t$ , mm	$b/t$	$h/t$	$L$ , mm	$p$ , mm	$a$ , mm	$f_{c,avg}$ , MPa	$f_{y,avg}$ , MPa
B-1	236.0	240.0	4.02	58.7	59.7	2110.0	8.0	20.0	34.43	428.52
B-2	200.0	200.0	3.01	66.4	66.4	1750.0	7.0	20.0	39.83	335.86
B-3	240.0	240.0	3.01	79.7	79.7	2110.0	7.0	20.0	38.43	335.86
B-4	180.0	240.0	3.01	59.8	79.7	2110.0	7.0	20.0	35.75	335.86

### 2.2.2. Flexural beam test setup and procedure

A hydraulic press of the 500 tons capacity was used to load the beams. A four point loading scheme with two concentrated loads was adopted. Three LVDT transducers were used to measure the deflection of each beam. Transducers T1 and T2 were used to eliminate the possible effects of the support settlement. The latter transducers were centred to match the centre of the support plates. Transducer T3 was used to measure the deflection of each beam at the mid-span. This transducer was placed to match the plane of the beam web in order to avoid the effects of local buckling at the top flange. Strain gauges SG1, SG2 and SG3 were used to measure and track the strain development of the top flange, the bottom flange and the upper part of the web, respectively. The experimental scheme is presented in Fig. 2.10. The dimensions important for the testing of beams are presented in Table 2.10. The experimental setup of the flexural beam test is shown in Fig. 2.11. The bottom support plates were placed onto the cylinder rollers to simulate hinged supports. The load increase rate was set as 10 kN/s. The loading was stopped when the deflection had reached at least the 15 mm value and the bending moment had not been significantly increasing anymore.

**Fig. 2.10.** Flexural beam test: a) scheme; b) section A-A



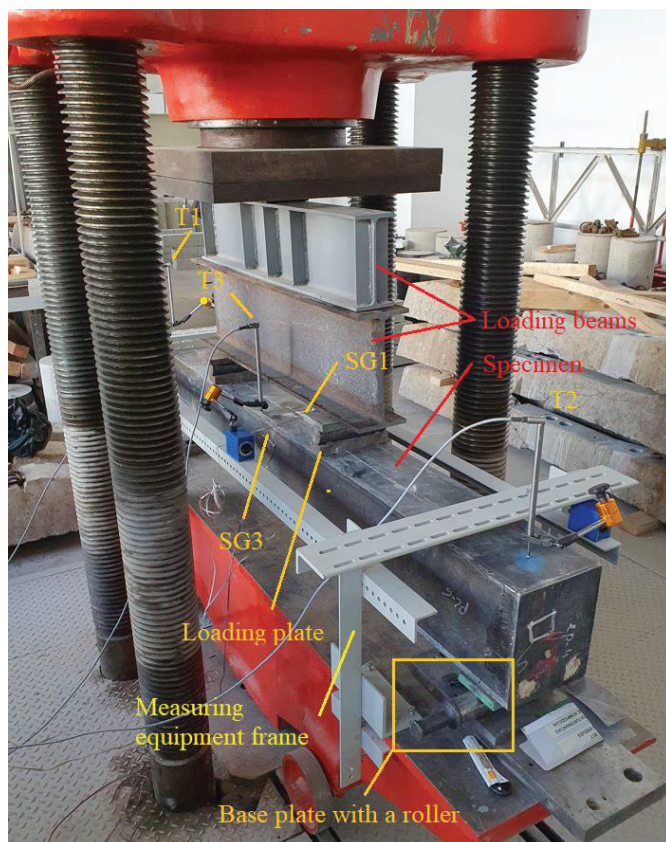


**Fig. 2.11.** Experimental setup of the flexural beam test

**Table 2.10.** Dimensions of experimental scheme

Beam marking	$L$ , mm	$v$ , mm	$x_{pl}$ , mm	$e$ , mm	$y_{sg}$ , mm
B1	2110.0	25	695	645	70
B2	1750.0	25	575	525	65
B3	2110.0	25	695	645	60
B4	2110.0	25	695	645	60

### 2.2.3. Experimental results of thin-walled steel concrete beams

Typical experimental post-local buckling shapes of the beams are presented in Fig. 2.12. In most cases, two major local buckling waves at the top flange formed. One major wave was present in all the beams close to one of the two loading plates. A second major buckling wave formed in the middle of two beams. In the cases of the latter two beams, a small third local buckling wave was barely visible close to the second loading plate. Top flange buckling was subsequently followed by the web buckling at the same cross-sections where the major top flange buckles had formed. It is obvious that the buckles did not form towards the inside of the beam, as the steel panels were constrained by concrete in this direction.





**Fig. 2.12.** Experimental post-buckling shapes of beams

The bending moment-deflection curves of the beams are presented in Fig. 2.13. It can be seen that the failure of the beams was very ductile. No sudden reduction of resistance was observed. It is generally considered that the failure due to buckling is sudden. However, this is only true in the case of global buckling, whereas the onset of the local buckling is followed by the stress redistribution. The middle unstiffened areas of the compressed panels are undergoing buckling. At first, the flange undergoing buckling acts as an eccentrically compressed element. When the local buckling is significant, the eccentric loading is replaced by the bending. This buckled part of the element undergoing bending then becomes inefficient in terms of carrying the compressive load. Thus, major stresses begin to concentrate at the edges of the flange. As a consequence, the average stiffness of the flange is reduced. It can be seen in Fig. 2.13 that only the initial part of the curves is linear. Slight nonlinearity is already noticeable in the early loading stages. However, when analysing the aforementioned curves, it is difficult to make a distinction whether those first nonlinearities are caused by the local buckling or the nonlinear behaviour of concrete.

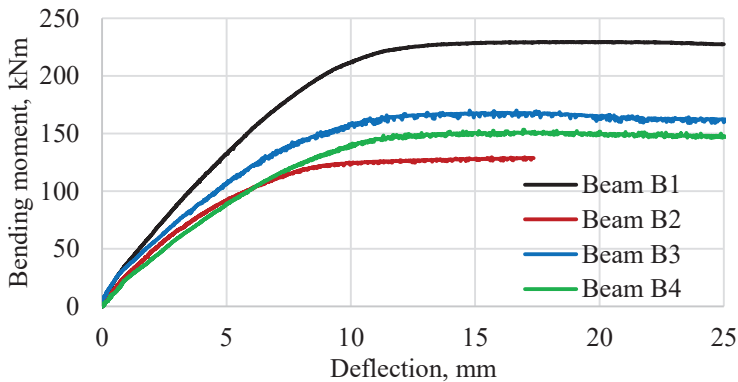


**Fig. 2.13.** Bending moment-deflection curves of experimental beams

The experimental bending moment-strain curves of the beams are presented in Fig. 2.14. This type of results is highly sensitive to the initial imperfections. When analysing the strains of the SG1 strain gauge at the top flange of beam B2, it became obvious that this flange was undergoing local buckling. As this flange is buckling, the compressive strain at lower loads becomes the tensile strain at higher loads. This shift from compression to tension is very clear because the centre of the buckling wave is

in the same position where the strain gauge is glued. In the other three cases, the top flange buckling wave centre is away from the strain gauge. As a consequence, there is no shift from compression to tension.

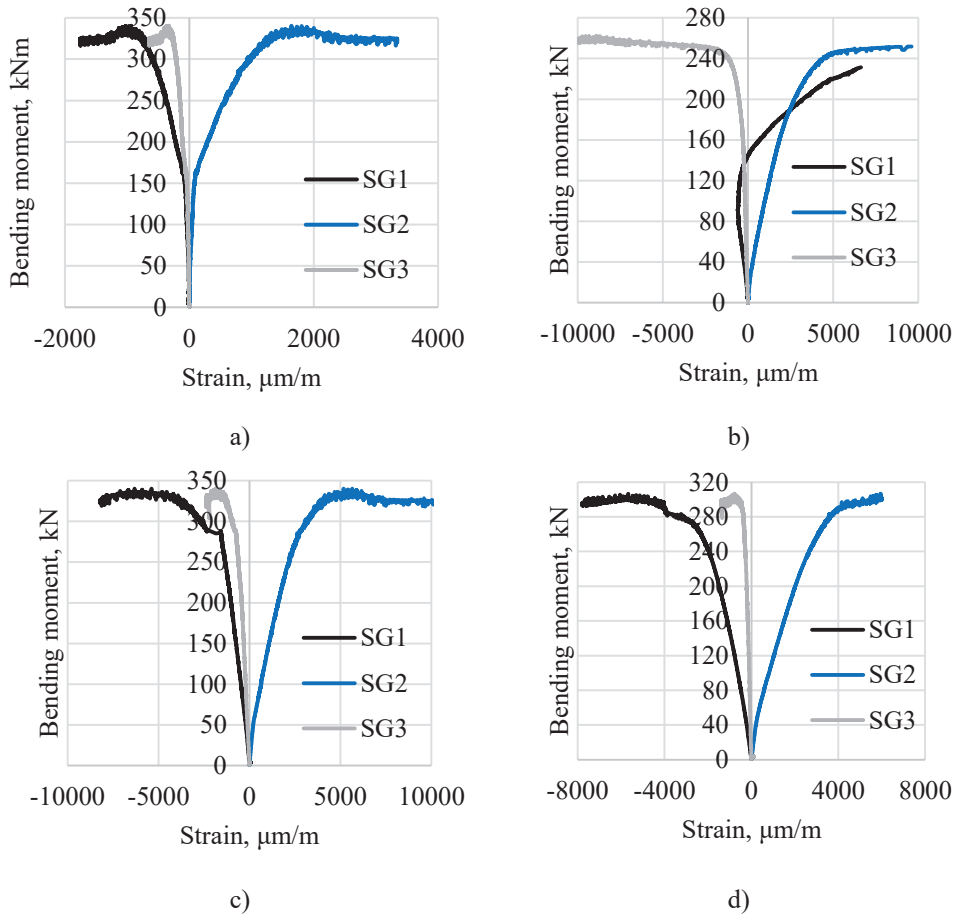


**Fig. 2.14.** Bending moment-strain curves of the beam: a) B1; b) B2; c) B3; d) B4

In this case, the results of a single strain gauge at the steel panel (the top flange, the bottom flange, or the web) can only be used as complementary. The more in-depth results and the development of strains shall be obtained by using the theoretical methods in the following chapters.

### 2.3. Conclusions of Chapter Two

1. It was found during the experimental testing of steel-concrete columns that the average reduction of the effective cross-sectional area ratio  $A_{eff}/A_s$  due to the poor bond conditions was 12% compared to the columns having a regular bond. Individual WO type columns had an up to 47% higher effective cross-sectional area ratio compared to the corresponding W type columns.
2. The critical stress results of the columns showed wide stochastic scattering due to the uncertainty of the initial geometrical imperfections. As a consequence, some strain gauges could be glued away from the centres of the local buckling half-waves. Random loading eccentricities could also exert influence on the precision of such results. A similar situation was also obtained during the flexural testing of the beams. If the strain gauge is in the centre of the local buckling half-wave, the compressive strains develop into the tensile strains at high deflections, as it was the case for beam B2. However, due to the initial geometrical imperfections, it is very likely that a single strain gauge may be away from the centre of the local buckling half-wave.
3. The failure of the columns was ductile. The onset of local buckling led to the stress redistribution. The failure was then governed by the yielding of the unbuckled corner areas. After the ultimate strength had been reached, gradual loss of resistance was observed. A more sudden loss of resistance was obtained in some cases where the corner fillet welds failed. However, it is important to note that the welds only failed after the ultimate strength had been reached and high amplitude local buckling half-waves had been observed. Flexural beam specimens exhibited even higher ductility. After the significant local buckling half-waves had already formed, no significant loss of resistance was observed.

### III. THEORETICAL RESEARCH OF THIN-WALLED COMPOSITE STEEL-CONCRETE STRUCTURES

#### 3.1. Calculation methods for thin-walled steel-concrete columns

##### 3.1.1. Methods and general expressions

In this chapter, concrete-filled thin-walled welded steel columns are analysed by using theoretical calculation methods. Detailed descriptions of the methods are provided in Chapter One. Expression (1.23) of Liang *et al.* [53] was used to calculate the critical stresses of experimental steel plates with the initial imperfections. Expression (1.21) proposed by Liang and Uy [48] and Expression (1.20) proposed by Bradford *et al.* [12] were used to obtain the effective widths of steel panels. Expression (1.24) proposed by Liang *et al.* [53], Expression (1.26) proposed by Ge and Usami [34] and Expression (1.28) proposed by Nakai *et al.* [66] were used to calculate the ultimate strengths of steel panels. The ultimate stresses were subsequently converted to effective widths by using Expression (1.29).

The critical buckling load of a column is obtained by using the following Expression (3.1) where the critical stress is calculated according to Liang *et al.* [53]:

$$N_{cr,Liang} = A_s \sigma_{cr,imp} + A_c \sigma_{c,cr} \quad (3.1)$$

where:  $\sigma_{c,cr}$  is the concrete stress calculated from Expression (1.1) at the strain corresponding to the critical stress of steel.

The ultimate strengths of columns were calculated by using the following Expression:

$$N_u = A_{eff} f_y + A_c f_{cm} \quad (3.2)$$

where:  $A_{eff}$  is the effective cross-sectional area of steel profile.

##### 3.1.2. Comparison of calculation methods for thin-walled steel-concrete columns

The experimental and theoretical critical buckling load and the ultimate strength results of the columns obtained by using the methods listed in Chapter 3.1.1 are summarised in Table 3.1. Experimental results are marked with the subscript ‘ex’. Theoretical results are marked with the subscript referring to the method author’s name. The critical buckling loads and the ultimate strengths were obtained by using the general Expressions (3.1) and (3.2), respectively. However, the critical stresses and effective steel cross-sectional areas for those expressions were obtained by using the methods of the respective authors. The list of the methods and subscripts used in Table 3.1 with reference to the original research of other authors is as follows: the critical buckling stress calculation method of Liang *et al.* [53] (‘Liang’), the effective width calculation methods of Liang and Uy [48] (‘Liang,Uy’), Bradford *et al.* [12] (‘Br’), the ultimate strength calculation method proposed by Ge and Usami [34] (‘Ge’), as well as the alternative method of Nakai *et al.* [66] (‘Nakai’).

**Table 3.1.** Experimental and theoretical local and post-local buckling results of the columns

Column marking	$N_{cr,ex}$ , kN	$N_{u,ex}$ , kN	$N_{cr,Liang}$ , kN	$N_{u,Liang,Uy}$ , kN	$N_{u,Liang}$ , kN	$N_{u,Br}$ , kN	$N_{u,Ge}$ , kN	$N_{u,Nakai}$ , kN
1-W	1350.0	1706.6	1136.1	1730.7	1762.2	1700.7	1714.9	1759.4
1-WO	975.0	1682.6	1132.9	1684.4	1718.5	1660.9	1672.7	1715.0
2-W	1400.0	1957.0	1350.6	1868.4	1916.8	1818.8	1849.2	1912.7
2-WO	1750.0	1930.5	1344.4	1886.4	1933.1	1835.1	1866.2	1930.8
3-W	600.0	1554.9	1236.0	1681.7	1688.4	1634.7	1643.4	1677.0
3.1-WO	600.0	1612.1	1209.9	1663.2	1665.8	1607.9	1619.2	1654.5
3.2-WO	700.0	1701.9	1273.6	1747.3	1753.5	1698.6	1707.8	1742.0
4-W	900.0	1085.3	793.3	1065.6	1084.2	1166.0	1109.6	1113.9
4-WO	800.0	1184.2	827.9	1120.6	1139.2	1208.0	1163.1	1164.6
5-W	750.0	1352.7	1087.0	1576.9	1612.9	1586.9	1584.9	1612.8
5-WO	1300.0	1543.7	1090.4	1587.9	1623.8	1595.5	1594.6	1623.4
6-W	950.0	1358.4	1096.8	1458.9	1473.4	1443.0	1442.5	1465.9
7-W	1025.0	1167.2	936.7	1214.3	1239.5	1262.8	1239.4	1247.8
7-WO	1100.0	1343.2	938.3	1216.5	1241.9	1266.7	1242.5	1250.7
8-W	900.0	1043.4	788.6	1011.0	1035.5	1119.8	1070.6	1065.6
8-WO	1000.0	1112.0	788.5	1011.6	1036.1	1112.4	1066.9	1063.3

The ratios between the experimental and the theoretical strength values are shown in Table 3.2. It is obvious that the variation of the  $N_{cr,ex}/N_{cr,Liang}$  ratio is large. The reasons that may have led to inaccuracies of the experimental critical stress measurement were described in Chapter Two. However, the average  $N_{cr,ex}/N_{cr,Liang}$  ratio is 3% higher for the WO type columns compared to the W type columns. Thus, it is likely that steel panels are stabilised by the steel-concrete bond.

The results obtained by using the theoretical ultimate strength calculation methods were adequate. The aforementioned methods underestimated the strength of the experimental WO type columns by up to 2% if considering the average experimental to theoretical ultimate strength ratios  $N_{u,ex}/N_u$ ; meanwhile, the strengths of the W type columns were overestimated by up to 5%. Generally, the ultimate strength was predicted more accurately for the WO type columns. The only individual column with the strength overestimation of more than 10% was column 5-W. Furthermore, the  $N_{u,ex}/N_u$  ratio of column 5-W was more than 10% lower than the ratio of the respective 5-WO column. This kind of difference is too large to be explained by the different level of imperfections. It is likely that it was influenced by the concrete strength uncertainty for column 5-W. The only W type column having a higher  $N_{u,ex}/N_u$  ratio than the respective WO type column was from series 2. However, the difference was less than 3%, and it is likely that it was observed due to the different level of the initial imperfections. Considering the results of the individual columns, the theoretical results varied from an underestimation of 10% to an overestimation of 14%. When comparing the average values of  $N_{u,ex}/N_u$  ratios, it is obvious that some strength may be lost due to the poor bond. The mid-panel areas of the steel profiles are separated from concrete at the ultimate load stage. However, it is still possible that

some steel-concrete bond remains in the corner regions of the columns at this stage. Therefore, the corner regions may be stabilised due to the remaining bond.

When considering the average  $N_{u,ex}/N_u$  ratios of the columns having the regular bond, the best agreement with the experimental results was obtained by using the method of Nakai *et al.* [66]. Considering the average ratios of all columns, the best agreement was observed when the method of Liang and Uy [48] was used. This method showed the lowest strength overestimation in the case of poor contact conditions, while a moderate reserve was maintained for the WO type columns.

**Table 3.2.** Comparison of experimental and theoretical local and post-local buckling results of the columns

Column marking	$N_{cr,ex}/N_{cr,Liang}$	$N_{u,ex}/N_{u,Liang,Uy}$	$N_{u,ex}/N_{u,Liang}$	$N_{u,ex}/N_{u,Br}$	$N_{u,ex}/N_{u,Ge}$	$N_{u,ex}/N_{u,Nakai}$
1-W	1.19	0.99	0.97	1.00	1.00	0.97
1-WO	0.86	1.00	0.98	1.01	1.01	0.98
2-W	1.04	1.05	1.02	1.08	1.06	1.02
2-WO	1.30	1.02	1.00	1.05	1.03	1.00
3-W	0.49	0.92	0.92	0.95	0.95	0.93
3.1-WO	0.50	0.97	0.97	1.00	1.00	0.97
3.2-WO	0.55	0.97	0.97	1.00	1.00	0.98
4-W	1.13	1.02	1.00	0.93	0.98	0.97
4-WO	0.97	1.06	1.04	0.98	1.02	1.02
5-W	0.69	0.86	0.84	0.85	0.85	0.84
5-WO	1.19	0.97	0.95	0.97	0.97	0.95
6-W	0.87	0.93	0.92	0.94	0.94	0.93
7-W	1.09	0.96	0.94	0.92	0.94	0.94
7-WO	1.17	1.10	1.08	1.06	1.08	1.07
8-W	1.14	1.03	1.01	0.93	0.97	0.98
8-WO	1.27	1.10	1.07	1.00	1.04	1.05
Avg. W	0.95	0.97	0.95	0.95	0.96	0.95
Avg. WO	0.98	1.02	1.01	1.01	1.02	1.00
Avg. all	0.97	1.00	0.98	0.98	0.99	0.97

## 3.2. Numerical modelling of thin-walled composite steel-concrete structures

### 3.2.1. Geometry and mesh

Doubly symmetric quarter models of columns and beams were created by using the finite element software *Abaqus* to analyse the behaviour of thin-walled structures. When analysing both types of structures, the same finite element types were used for the respective cross-section elements. The steel profile and the stiffeners were modelled by using the 4-node 2D reduced integration shell elements (S4R). 8-node 3D elements with reduced integration (C3D8R) were used to model the concrete, as well as the loading and support plates. 2-node linear displacement elements (T3D2) were used to model the reinforcement.

The mesh size of the column steel profile was assumed as  $B/24$  and  $H/24$  along the width and the height of the cross-section, respectively. The mesh size along the length of the column was set as  $L/100$ . The mesh dimensions of the column concrete

core were assumed to be of the double size of the steel profile. Therefore, the concrete mesh sizes were set as  $B/12$ ,  $H/12$  and  $L/50$ , respectively. Similar mesh sizes for the concrete and steel parts were used in the research of Duarte *et al.* [21]. After the initial mesh sensitivity analysis, it was found that such mesh discretisation is adequate to achieve sufficient accuracy of the results. Further mesh size reduction was found to increase the calculation time significantly, but only had a minor effect on the results. The adopted mesh discretisation is also illustrated in Fig. 3.3 and Fig. 3.4 in Chapter 3.2.3.

The mesh element sizes along the width and the height of the cross-sections were also set the same for the modelling of the beams. It is important to note that the length of the pure bending zone of the beams was equal to the unstiffened length of the columns having a similar cross-section. It is relevant because the unstiffened length of a steel panel may exert influence on the critical buckling stress. In this case, the same lengths were designed, and, thus, the results of the different types of structures are comparable. For example, the unstiffened length of columns 2-W and 2-WO was 620 mm, same as the length of the pure bending zone of beam B-1. The aforementioned columns and the beam had a similar cross section of 240×240 mm. Therefore, the mesh size along the length of the beam was adjusted to have the same length as the respective column of a similar cross-section.

The mesh size of the loading and support plates was set to be in the range between 10 mm to 20 mm. The size of the T3D2 mesh elements for the reinforcement was set as 25 mm. It was also found that the mesh size of the plates and the reinforcement had a negligible influence on the results.

### 3.2.2. Material models and initial imperfections

Two types of initial imperfections were evaluated during the finite element modelling of the steel-concrete structures: the initial geometrical imperfections and the residual stresses. Geometrical imperfections were taken into account by introducing the idealised imperfection shapes proposed by Wright [93] via the use of Expression (1.13). Number  $m$  of lateral geometrical imperfection half-waves had a fixed value of 1. However, a different number  $n$  of longitudinal imperfection half-waves were tested during the initial sensitivity analysis. It was found that this number exerted minor influence on the ultimate strength of the structures, as long as there were three or more half-waves. A lower number of half-waves were found to increase the resistance of the analysed members. Therefore, based on the observations of the experimental post-buckling shapes and the results of the sensitivity analysis, the longitudinal half-wave number  $n$  was set as 5. Parameter  $\omega_0$  was set as 1/200 of the width of the steel panel according to part 1–5 of Eurocode 3 [28]. The geometrical imperfections in *Abaqus* models were introduced for the compressed flanges and the upper half of the webs via the *Python* programming script.

Primarily, the residual stress distribution adopted in the current finite element analysis was based on the idealised model proposed by Uy [87]. This kind of residual stresses was directly introduced into the FE models by using the ‘predefined fields’ function in *Abaqus*. Alternatively, the influence of the residual stresses was taken into account indirectly via the modification of the stress-strain curves of the structural



steels. This kind of the modified stress-strain curve model for the mechanical cut steel plates was proposed by Song *et al.* [82]. It was found that there was a minor difference of the load-shortening and moment-deflection results of the analysed structures when using the different residual stress evaluation methods. Therefore, the second method was selected in order to simplify the analysis of the obtained results.

The adopted stress-strain material models for structural steel are presented in Fig. 3.1 a). As proposed by Liang [49], the strain corresponding to the onset of strain hardening  $\varepsilon_{ym,2}$  can be assumed 10 times higher than the yield strain  $\varepsilon_y$  of steel with no residual stresses. Furthermore, according to Pan [68], the strain corresponding to the ultimate strength of steel  $\varepsilon_u$  can be assumed as  $10\varepsilon_{ym,2}$ . The stress-strain curve modified according to Song *et al.* [82] was used to take into account the effects of residual stresses. Stress value  $f_{pym}$  and strain values  $\varepsilon_{pym}$ ,  $\varepsilon_{ym}$  were calculated according to Expressions (1.14), (1.16) and (1.17), respectively, as proposed by Song *et al.* [82]. In order to model the compressive behaviour of concrete, the nonlinear uniaxial stress-strain curve of Eurocode 2 [26] was used. This model is presented in Fig. 3.1 b). The idealised elastic-perfectly plastic material model with no strain hardening was used for reinforcement.

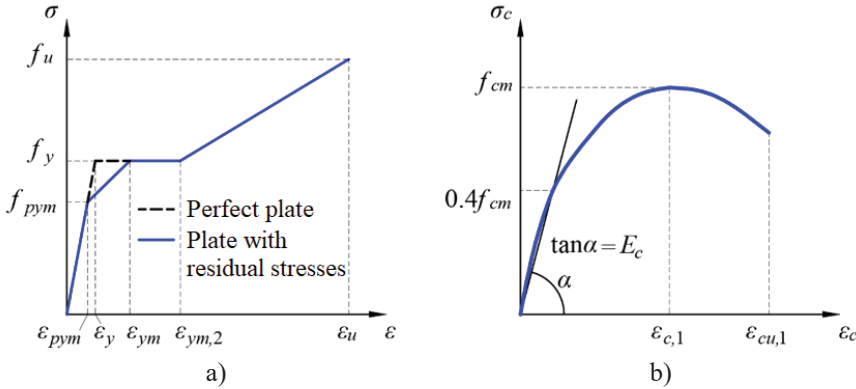


**Fig. 3.1.** Material model of: a) structural steel with and without residual stresses according to Song *et al.* [82]; b) concrete according to Eurocode 2 [26]

The concrete behaviour in *Abaqus* was modelled by using the ‘Concrete Damaged Plasticity’ (CDP) material model. This model uses a non-associated plastic flow potential  $G$  based on the Drucker-Prager hyperbolic Function [79]:

$$G = \sqrt{(\varepsilon \sigma_{t0} \tan \psi)^2 + q^2} - p_h \tan \psi \quad (3.3)$$

where:  $\varepsilon$  is the flow potential eccentricity of the hyperbolic function;  $\sigma_{t0}$  is the tensile strength of concrete;  $\psi$  is the dilation angle;  $q$  is the von Mises equivalent effective stress;  $p$  is the hydrostatic pressure.

The CDP model also considers the initial equibiaxial compressive yield stress to the initial uniaxial compressive yield stress ratio  $f_{b0}/f_{c0}$ , as well as the ratio of the second stress invariant on the tensile meridian to that on the compressive meridian  $K_c$ . The default values of  $f_{b0}/f_{c0}=1.16$  and  $K_c=2/3$  were used [79]. The dilation angle value  $\psi$  was set as  $20^\circ$  according to Ellobody *et al.* [23]. Lastly, the flow potential



eccentricity  $\varepsilon$  was set equal to the default value of 0.1 [79]. It is important to note that the effects of confinement in the CDP material model are accounted for via the use of the aforementioned plasticity parameters. Therefore, the uniaxial stress-strain model of confined concrete is not used in this case.

The tensile stress-strain behaviour of concrete is elastic until the tensile strength  $\sigma_{t0}$  is reached. The tensile post-cracking curve of concrete is presented in Fig. 3.2. The post-cracking behaviour was described via the fracture energy  $G_f$ . This type of definition is simplified and does not take into account the exact post-cracking behaviour. However, it is still sufficient for the case of steel-concrete composite structures where the resistance of the cross-section is usually governed by the compressive strength of concrete as well as the compressive and tensile strength of steel. In this case, the fracture energy  $G_f$  can be calculated by using the following Expression from CEB-FIP MC 2010 [32]:

$$G_f = 73 f_{cm}^{0.18} \quad (3.4)$$

Therefore, the displacement corresponding to the complete loss of tensile resistance can be calculated by using the following Expression:

$$u_{t0} = \frac{2G_f}{\sigma_{t0}} \quad (3.5)$$

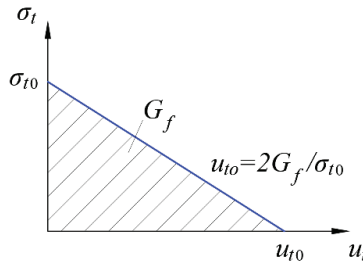


**Fig. 3.2.** Tensile post-cracking stress-displacement behaviour of concrete

### 3.2.3. Contacts, boundary conditions, loads and assembly of models

During the modelling of the columns, the tangential contact between the steel profile and the concrete core was described by using the frictional penalty method. Different friction coefficient values were reported by different authors. Baltay and Gjelsvik [6], Rabbat and Russell [70], and Williamson *et al.* [91] reported 0.47, 0.57, and 0.5–0.6 values of the friction coefficient, respectively. However, this factor was found not to influence the results significantly, and the value of 0.57 was selected. The penetration of one material into another in the normal direction was disallowed by setting the ‘hard’ contact conditions. The contact of the support plate and the loading plate with the analysed structure was defined by using the tie constraints. Therefore, any slip between the aforementioned parts was disallowed. The bottom nodes of the bottom plate were tied with the reference point at the bottom of each column. Similarly, the top nodes of the top plate were tied to the reference point at the top of each column. The bottom reference point was prescribed to have zero degrees of freedom. The top reference point had a single degree of freedom and was allowed

to move in the longitudinal direction of the column. This top reference point was also prescribed to have a displacement load in the same direction. Therefore, the loading was displacement-controlled. This type of loading was selected because it is more stable and allows for a better convergence of the model. Lastly, two symmetry boundary conditions were assigned for the two planes of the column. This allowed to analyse the quarter models of every column and to save on the computational capacity. The assembly of the column model with scaled imperfections is presented in Fig. 3.3.

During the modelling of the beams, the loading and support plates were tied to the surfaces of the steel profile. The reinforcement was embedded into the concrete, thus disallowing the slip between the contact surfaces. Identically to the column models, the same tangential and normal steel-concrete contact conditions were assumed. The linear supports were attached to the support plates. The reference point was created in the top-middle of each loading plate. This point was tied with the nodes at the load line at the top of the loading plate. The vertical displacement load was then applied on this reference point. The reference point was allowed to rotate around the lateral axis of the beam and to displace along the longitudinal beam axis in order not to create additional restraints during the loading process. Similarly to the columns, quarter beam models were created. Therefore, two symmetry boundary conditions were assigned to each model. The assembly of the beam model with scaled imperfections is shown in Fig. 3.4. The reinforcement was modelled as a 2-node linear displacement element. Therefore, it is hidden in the concrete part and, thus, is not visible.

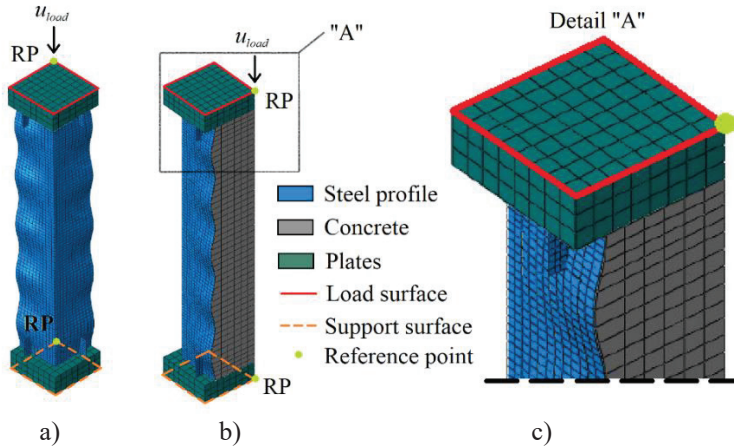


**Fig. 3.3.** Column model assembly with scaled initial imperfections: a) isometric corner view; b) isometric view of the symmetry plane; c) detail 'A'

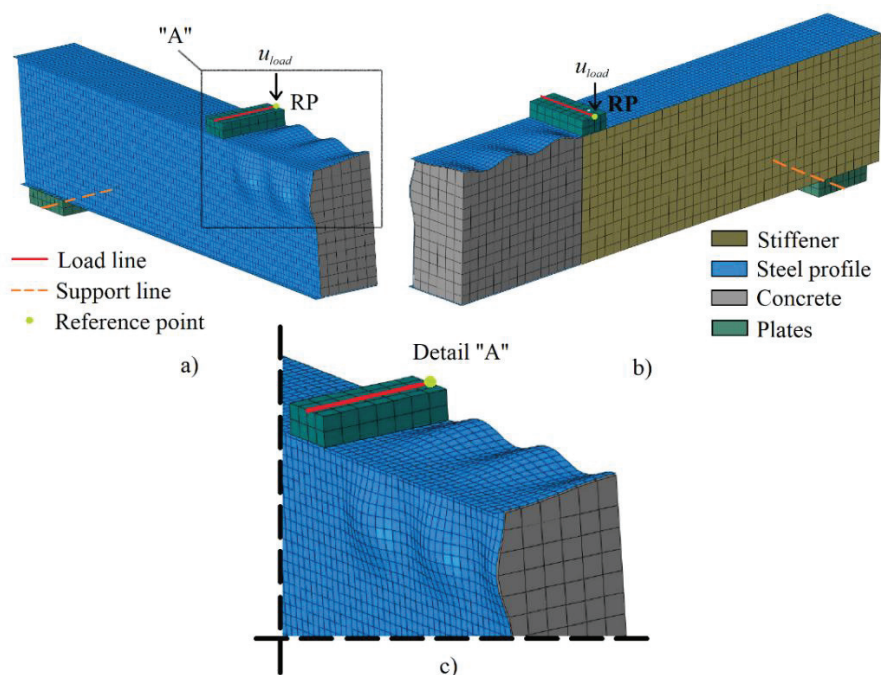


**Fig. 3.4.** Beam model assembly with scaled initial imperfections: a) left side isometric view; b) right side isometric view

The static, general analysis procedure was used. Geometrical nonlinearity was considered. The maximum step increment size was selected as 1%. The full Newton solution technique was adopted.

### 3.2.4. Numerical analysis of thin-walled composite steel-concrete columns

In this chapter, the finite element models (with the initial imperfection amplitude of  $B/200$ ) of most of the WO type columns were created and analysed. Column 3.2-WO was excluded because two WO type specimens (3.1-WO and 3.2-WO) of the same cross-section were analysed experimentally, and a single specimen was sufficient for the finite element analysis. During the experimental campaign, only one column from series 6 was analysed. Thus, in order to expand the variety of the cross-sections, column 6-W was modelled as well.

The numerical load-shortening curves of the analysed columns were obtained and presented in Fig. 3.5. It can be seen that the maximum axial shortening value when the ultimate strength had been reached was approximately 1.4 mm. In some cases, the experimental shortening values at the ultimate strength were as high as 5–6 mm. Low experimental stiffness was also reported by other authors, and the possible reasons were discussed in Chapter 2.

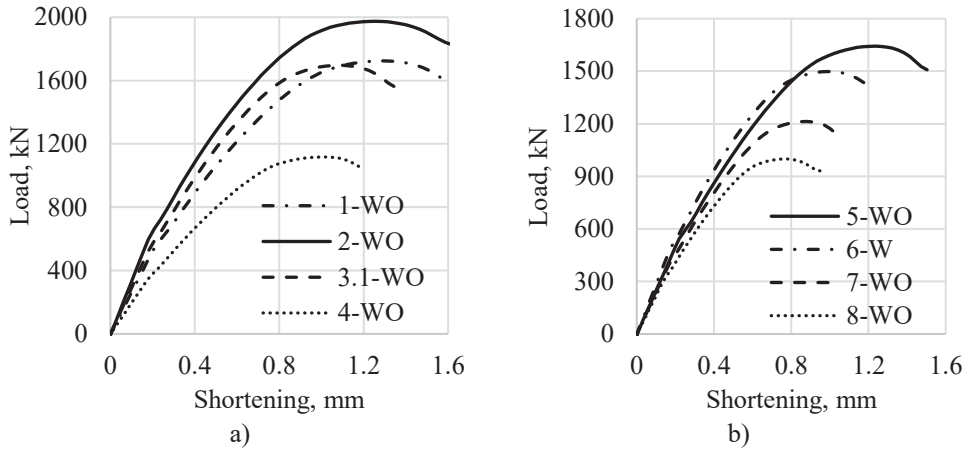


**Fig. 3.5.** FE load-shortening curves of the columns: a) 1-WO, 2-WO, 3.1-WO and 4-WO; b) 5-WO, 6-W, 7-WO and 8-WO

The normal stress development of steel flanges was analysed by using the finite element method. Nine integration points (IP-1 to IP-9) through the flange thickness were used for each finite element. The setup of the integration points is presented in Fig. 3.6. Integration point IP-9 represents the flange surface in contact with concrete. Integration point IP-1 is on the opposite side of the flange, while integration point IP-5 is in the middle. The initial imperfections are relatively low. Thus, in the early loading stages, relatively constant stress distribution is expected. As the flange strain increases, flange deflection is becoming increasingly higher, and the middle of the flange is undergoing eccentric compression. At this point, the compressive stress at integration point IP-1 is lower than that of integration point IP-9. At a relatively high deflection, the mid-flange curvature becomes so large that integration point IP-1 is undergoing tension.

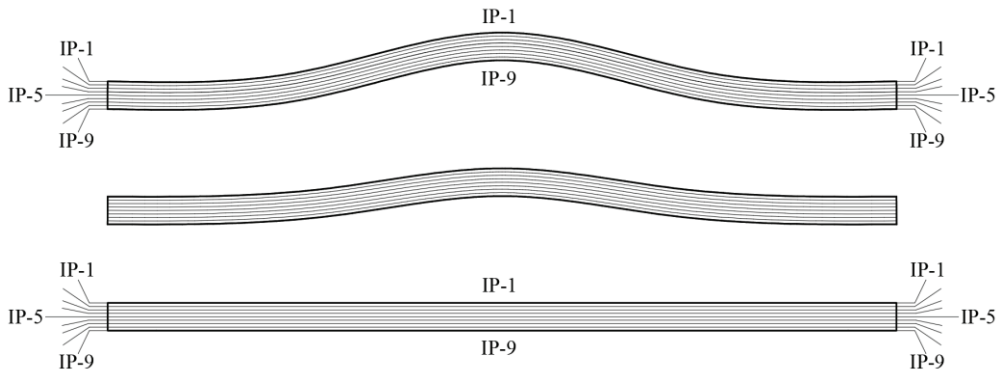


**Fig. 3.6.** Integration points in finite elements models

The analysis of column 2-WO is presented in this chapter. The steel profile of this column is the most slender of all the columns that were tested. Thus, this specimen was selected for detailed analysis.

Steel profiles of all the columns have initial imperfections. The surface of the concrete core matches the surface of the steel profile initially. As the column is loaded, gradual separation of the steel flange from the concrete core is observed. This kind of steel-concrete separation at the ultimate load stage in the column 2-WO model is presented in Fig. 3.7.

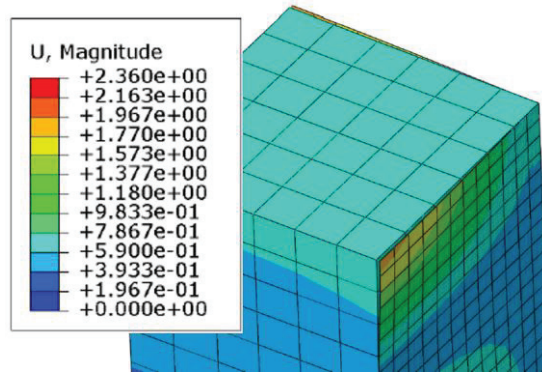


**Fig. 3.7.** Column 2-WO steel-concrete separation at the ultimate load stage

Numerical normal stress distributions at all the integration points at the ultimate load stage of the column 2-WO flange are presented in Fig. 3.8. It can be seen in Fig. 3.8 that the middle of the flange is undergoing bending as the first integration point (IP-1) and the second integration point (IP-2) are in tension. At the same time, the corner finite elements methods have a reverse curvature and are under eccentric compression.

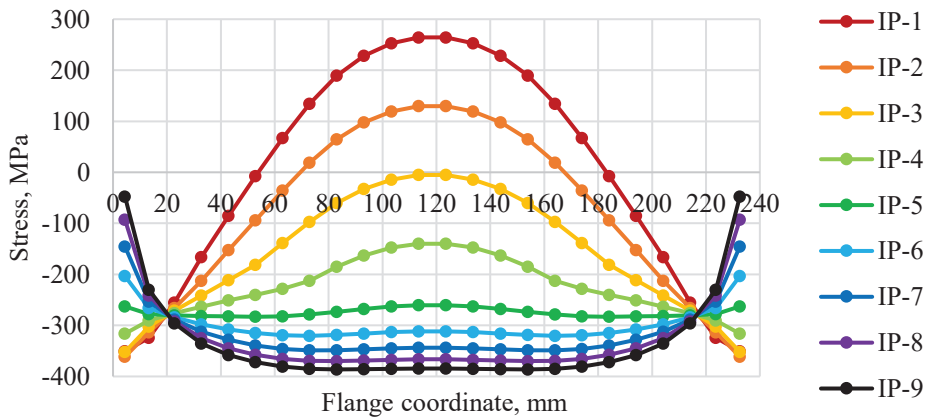


**Fig. 3.8.** Ultimate load stage normal stress distributions in column 2-WO flange

In the FE models, the failure occurs in the middle cross-section of each column. Therefore, this cross-section is analysed in detail. The normal stress distributions in MPa in the outer integration points of the steel profile of column 2-WO at the ultimate load and the 0.02 longitudinal strain are presented in Fig. 3.9. It can be seen that high level tensile stresses are present in the outer layer of the mid-panel areas. Furthermore,



when analysing the von Mises stress, it should be observed that the final failure occurs due to the yielding of the non-buckled corner regions.

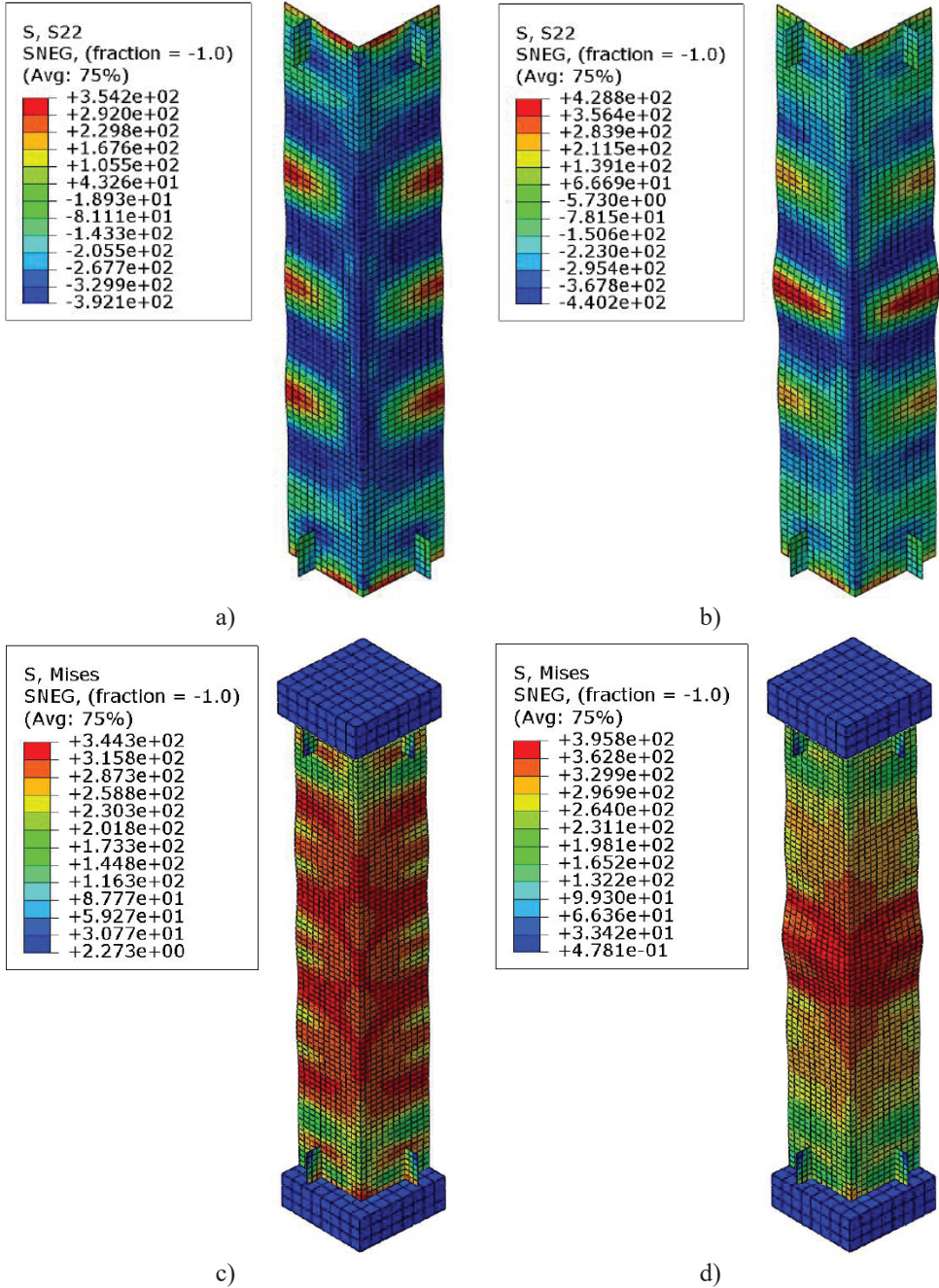


**Fig. 3.9.** Column 2-WO steel stress (MPa) distributions at outer integration points: a) longitudinal stress at the ultimate load; b) longitudinal stress at 0.02 strain; c) von Mises stress at the ultimate load; d) von Mises stress at 0.02 strain

The normal stresses of the nine integration points of the finite element were recalculated into a single axial force resultant. Consequently, this resultant force was recalculated into the average normal stress of the finite element. The average normal stress distribution and development of the column 2-WO flange is presented in Fig. 3.10. It can be seen that, from the initial loading stages, there is a small stress variation through the width of the flange due to the existence of the initial geometrical imperfections. This variation is getting increasingly more significant when increasing the load. The local buckling wave is developing. The stresses in the mid-flange area are increasing at a lower rate. From the 1840 kN load, the average stress increase in the middle finite elements stops, and the onset of the stress decrease is observed when the column is compressed further. The ultimate strength of the column is reached, and the strength starts to decrease. The ineffective flange cross-sectional area is gradually becoming wider, while the average normal stress of the corner elements is still increasing.

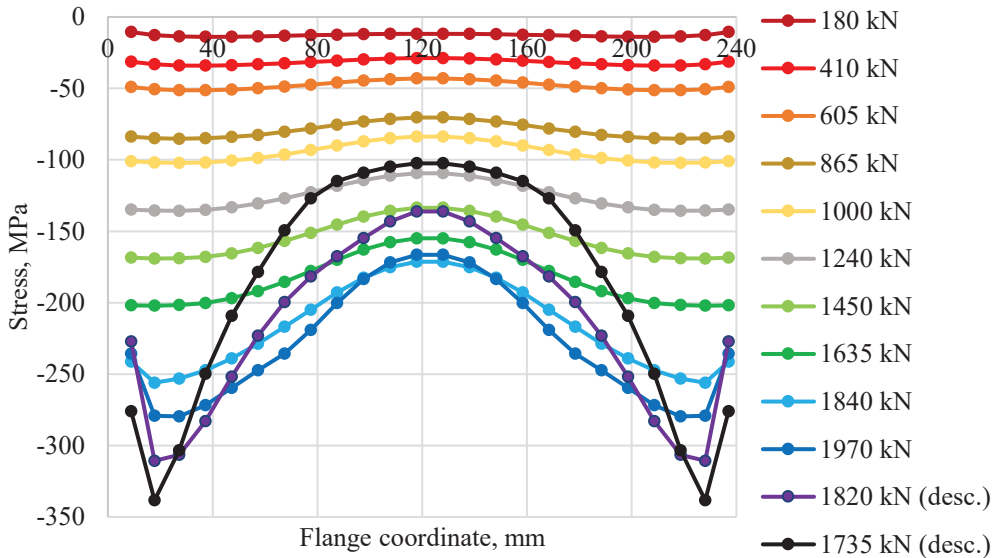


**Fig. 3.10.** Normal stress development in the flange of column 2-WO

The average normal stresses of the finite elements of the flange were recalculated into the single axial load resultant of the whole flange. Furthermore, the average normal stress of the flange was obtained. This kind of the average stress-strain curves was plotted for all of the steel panels of the analysed columns, and the curves are presented in Fig. 3.11. The highest point of such a curve can be set as the ultimate flange stress. It is obvious that the shape of the average stress-strain curve depends on the  $b/t$  ratio of the panel. It is also found during the further analysis that it also depends on the yield strength of the steel.

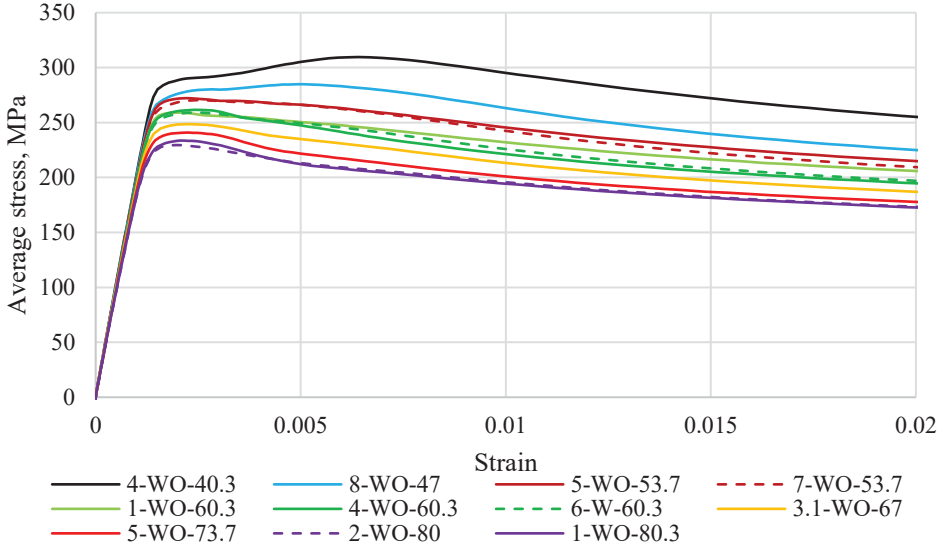


**Fig. 3.11.** Average normal stress-strain curves of column flanges

The critical stress values of the analysed column steel panels were found via the method of Liang *et al.* [53] by plotting the  $w/\sigma_1$ - $w/t$  curves obtained from the results of the FE analysis. Such curves of some of the analysed experimental column steel panels with different  $b/t$  ratios are presented in Fig. 3.12, where the lowest point of each curve corresponds to the onset of local buckling.

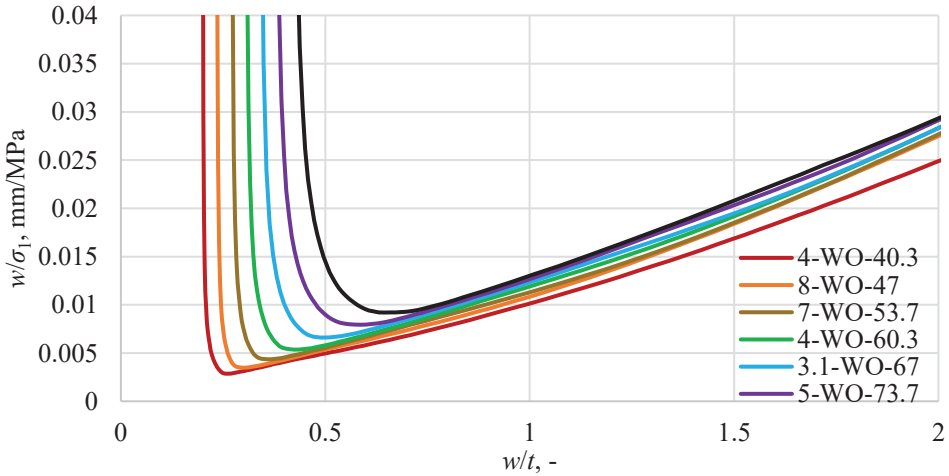


**Fig. 3.12.**  $w/\sigma_1$ -  $w/t$  curves of column flanges

In order to expand the range of results, columns 2-WO, 4-WO, 5-WO and 8-WO were also modelled via the finite element method with the steel yield strengths of 335.9 MPa and 428.5 MPa, as the latter yield strengths were obtained during the experimental campaign of the beams. The additional columns had the same concrete



properties of the respective experimental columns. The critical and ultimate stress results of the steel panels of all columns are presented in Chapter 3.3.

By analysing the average normal stresses of the steel panels and the concrete core, contributions of the different materials to the strength of the composite member can be obtained. The load-strain curves of the whole composite column 2-WO and the separate structural parts of the same column are presented in Fig. 3.13. The specific loading points shown in Fig. 3.10 are marked by using the dashed lines in Fig. 3.13. The steel profile of column 2-WO is wide and slender. Therefore, the local buckling is very significant for this type of cross-section. On the other hand, the concrete core is large. Thus, it can be seen that the axial strength contribution of the concrete is more than two times higher compared to the steel profile. It is also important to note that the maximum axial strength contribution of the steel profile and the concrete core are obtained at similar strain levels as there is no significant reduction of the steel profile resistance within the analysed range. Thus, in this case, the ultimate strength of the composite steel-concrete column has a similar value as the sum of the maximum loads resisted by the two materials.

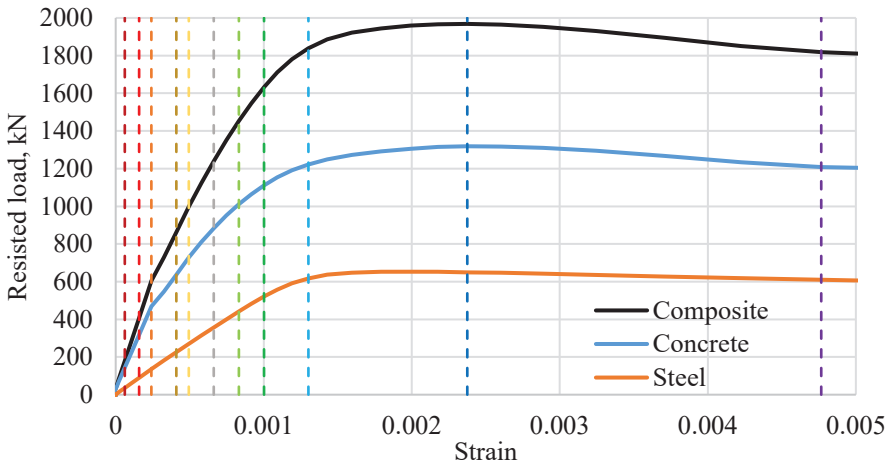


**Fig. 3.13.** Resisted load-strain dependencies of column 2-WO

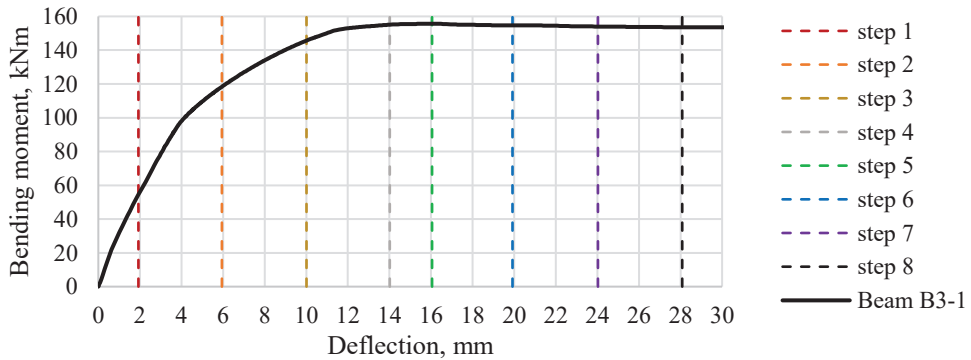
### 3.2.5. Numerical analysis of thin-walled composite steel-concrete beams

In this chapter, the finite element models of all the four experimental beams were created and analysed. The experimental campaign included three beams of the 335.9 MPa yield strength and one beam of the 428.5 MPa yield strength. To expand the  $b/t$  ratio range for the panels of the 428.5 MPa yield strength, two additional beams (B-5 and B-6) were modelled by using the same material properties and the steel profile thickness of beam B-1. The properties of the analysed FE models are summarised in Table 3.3. The marking of the dimensions is in accordance with Chapter 2.2.

**Table 3.3.** Dimensions and material properties of beam models

Beam marking	$b$ , mm	$h$ , mm	$t$ , mm	$L$ , mm	$p$ , mm	$a$ , mm	$v$ , mm	$e$ , mm	$f_{c,avg}$ , MPa	$f_{y,avg}$ , MPa	$E_{c,avg}$ , MPa
B-1	236	240	4	2110	8	20.0	25	645	34.43	428.5	33.25
B-2	200	200	3	1750	7	20.0	25	525	39.83	335.9	35.31
B-3	240	240	3	2110	7	20.0	25	645	38.43	335.9	35.14
B-4	180	240	3	2110	7	20.0	25	645	35.75	335.9	32.90
B-5	320	320	4	2950	8	20.0	0	950	34.43	428.5	33.25
B-6	280	280	4	2950	8	20.0	0	950	34.43	428.5	33.25

The numerical moment-deflection curve of beam B3-1 with the initial imperfections (residual stresses and geometrical imperfections of the  $B/200$  amplitude) is presented in Fig. 3.14. Specific loading steps (1–8) are marked with the dashed lines. Step 2 represents the loading stage when the maximum  $b_{eff}/b$  ratio of the compressed flange was obtained. Step 5 is the loading stage when the ultimate bending moment was observed. Other loading steps are non-characteristic, but they are required in order to track the changes of the beam parameters during the loading procedure.

**Fig. 3.14.** Bending moment-deflection curve of beam B3-1

Normal stress distributions through the width of the top flange of beam B3-1 at the load corresponding to the maximum effective cross-sectional flange area are presented in Fig. 3.15. The results of all nine integration points through the thickness of the shell are shown. The aforementioned stress distributions represent the loading step 2. In this step, the middle area of the flange is undergoing bending where the integration points IP-1 and IP-2 are in tension. The first and the last finite elements are under concentric compression. The latter two elements represent the top flange ledges on the opposite sides. The aforementioned elements are not susceptible to local buckling and are not used for the calculation of the effective area and the average stress of the compressed flange.

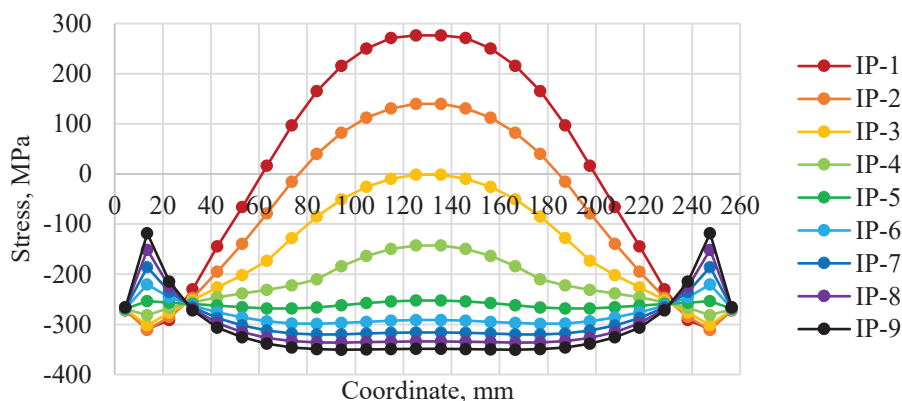


**Fig. 3.15.** Beam B3-1 top flange normal stress distributions at the load corresponding to the maximum effective area of the flange

Similarly to the column analysis, the resultant forces of each finite element are calculated, and the average normal stresses are obtained. The stress development of the compressed flange of beam B3-1 is shown in Fig. 3.16. When disregarding the two finite elements of the ledges, the stress development is similar to that of the previously analysed column 2-WO. However, small differences of the average normal stress-strain behaviour are observed due to the curvature of the flexural beam element.

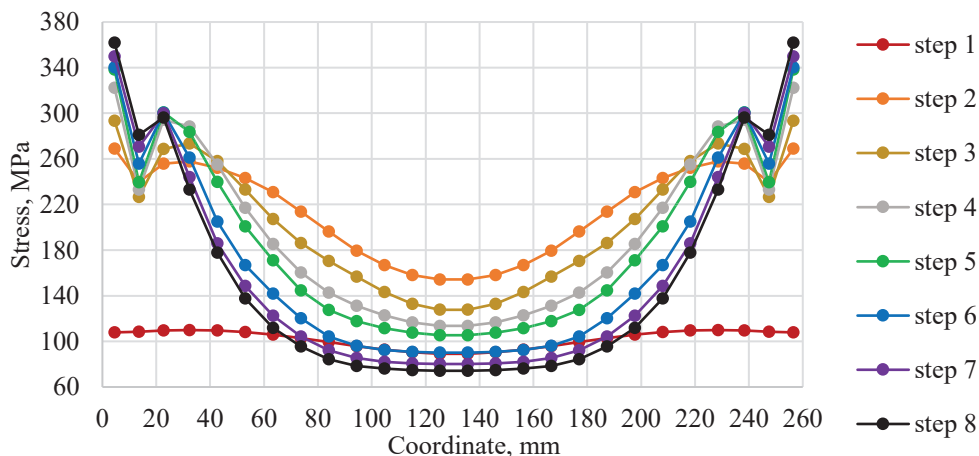


**Fig. 3.16.** Normal stress development in the top flange of beam B3-1

The normal stress distribution and development of the beam B3-1 web is presented in Fig. 3.17 a). From step 2 onwards, the breaking points in the tensile and compressive areas due to the existence of residual stresses are observed. However, the web stress reduction due to the local buckling is only more significant from step 7 onwards. This step represents a very advanced loading stage when the beam is already failing in the ductile manner. The maximum bending moment value was reached at step 5, whereas the bending moments in steps 6–8 are slightly lower. This kind of decrease is observed mainly due to the reduction of the effective area of the top flange.

The normal stress distribution and development of the beam B3-1 concrete core is presented in Fig. 3.17 b). Each marker represents the average normal stress when considering all the finite elements at the respective cross-section height coordinate. The maximum concrete stress considering the analysed steps is reached at step 3. However, despite the small reduction of the maximum stress, the stress distribution is gradually becoming more even in the further steps.

The normal stress distribution in the steel and concrete parts of the cross-section at step 8 is presented in Fig. 3.18. At the height of approximately 170 mm (as it was shown in Fig. 3.17), there is a significant concrete stress reduction. As the web buckles at a specific height, it does not provide effective support for the concrete anymore. Once the confinement effect has been lost in this area, the concrete stress reduces significantly.

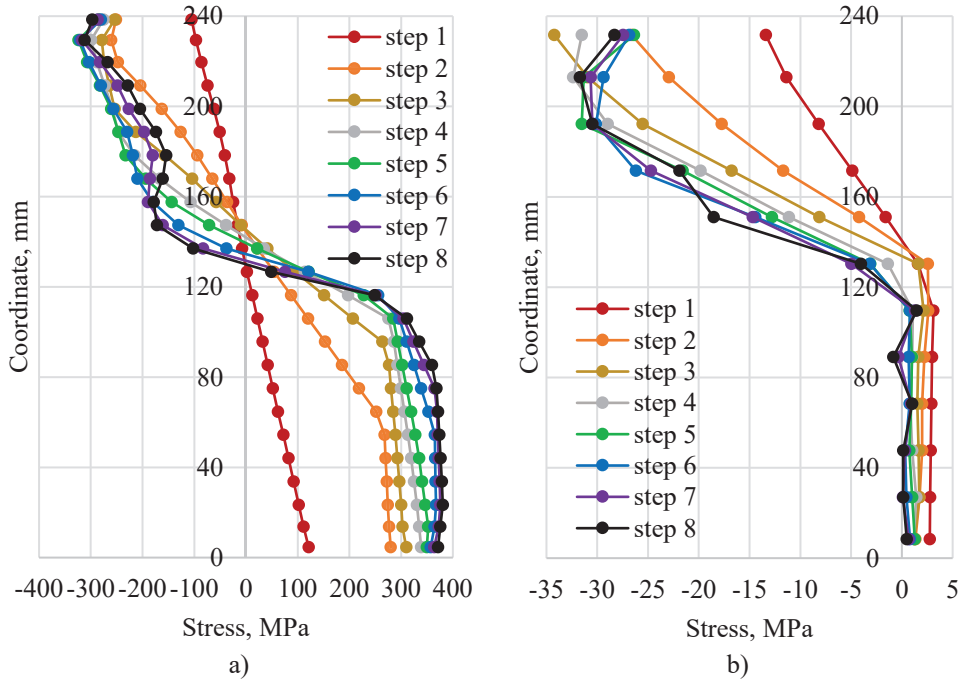


**Fig. 3.17.** Normal stress development of beam B3-1: a) web; b) concrete core

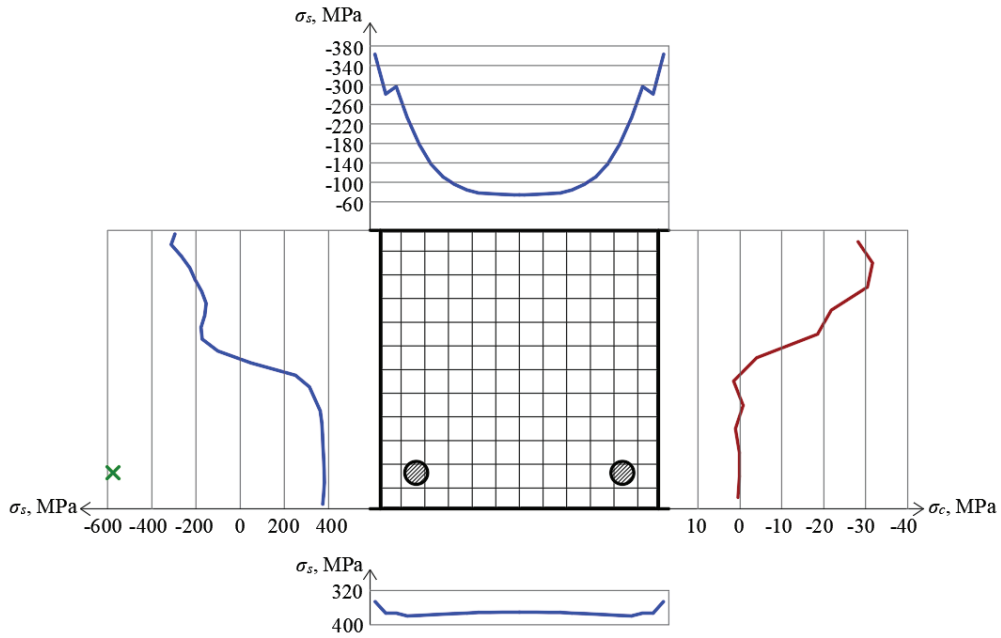


**Fig. 3.18.** Normal stress distribution in beam B3-1 at loading step 8

The values of the bending moment, the top flange effective width ratio, the average compressive concrete normal stress and the reinforcement stress at the different loading steps are presented in Table 3.4. The maximum effective width of the compressed flange was reached at step 2, which is a relatively early loading stage. At this stage, the bending moment value was 76% of the bending moment resistance. Furthermore, at step 2, the reinforcement and the compressive concrete stresses were 54% and 71% of the maximum respective values. In the further steps, the reduction of the effective flange width was observed. Once the maximum bending moment had been obtained, the effective width ratio value was 84% of the ultimate value. On the other hand, the flange strength loss was compensated by the increased stresses of the reinforcement and concrete. The average compressive concrete stress remained relatively constant across the whole range between steps 3 and 6. The effective flange width reduced further in the last steps (steps 7 and 8). Similarly, a decrease of the average compressive concrete stress was observed in the final steps as well. However, throughout the entire loading procedure, the concrete stresses were becoming more and more evenly distributed. A small increase of the compressed concrete height was observed as well. Thus, even though the effective width of the flange was decreasing significantly, only a very small bending moment decrease was observed from step 5 onwards.

**Table 3.4.** Bending moment, top flange effective width, average concrete stress and reinforcement stress development in beam B3-1 at different loading steps

Step	Note	Bending moment, kNm	Flange $b_{eff}/b$	Reinforcement stress, MPa	Avg. concrete stress, MPa
1	-	54.8	0.303	102.7	7.7
2	Max. $b_{eff}/b$	119.3	0.630	308.7	16.2
3	-	146.8	0.589	506.0	22.7
4	-	156.3	0.556	568.9	20.5
5	Max. moment	156.8	0.528	572.6	21.0
6	-	156.4	0.470	573.6	21.5
7	-	156.1	0.438	575.7	18.8
8	-	156.1	0.418	576.2	19.1

Von Mises stress and normal stress distributions at the load corresponding to the maximum top flange effective area (step 2) are presented in Fig. 3.19 and Fig 3.20, respectively. The concrete in Fig. 3.20 is excluded for the clarity of presentation.

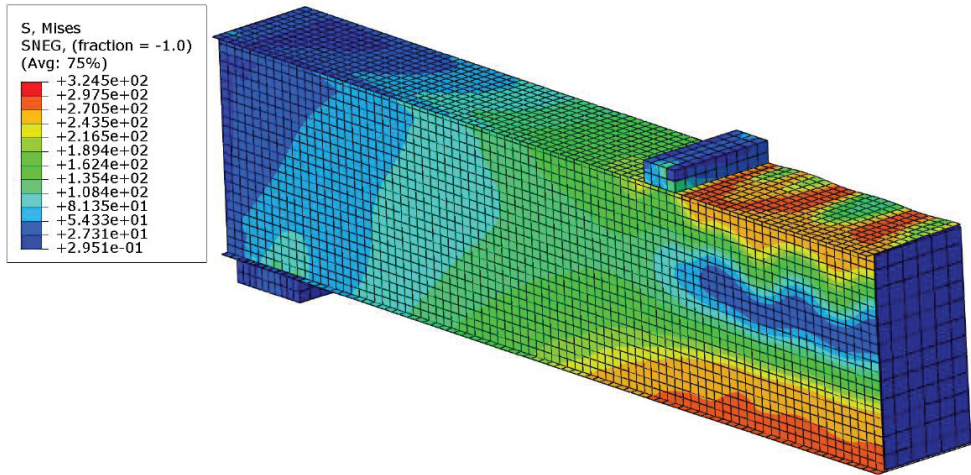


**Fig. 3.19.** Beam B3-1 Von Mises stress (MPa) distributions (outer steel integration points) at the maximum top flange effective area

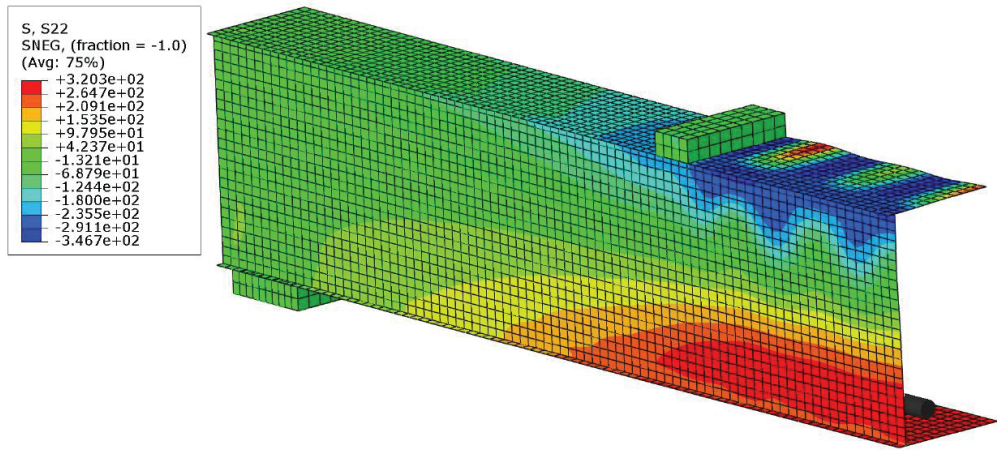


**Fig. 3.20.** Beam B3-1 normal stress (MPa) distributions (outer steel integration points) at the maximum top flange effective area

Von Mises stress distribution at the maximum bending moment (step 5) is presented in Fig. 3.21. The normal stress distribution at the same load is presented in Fig. 3.22.

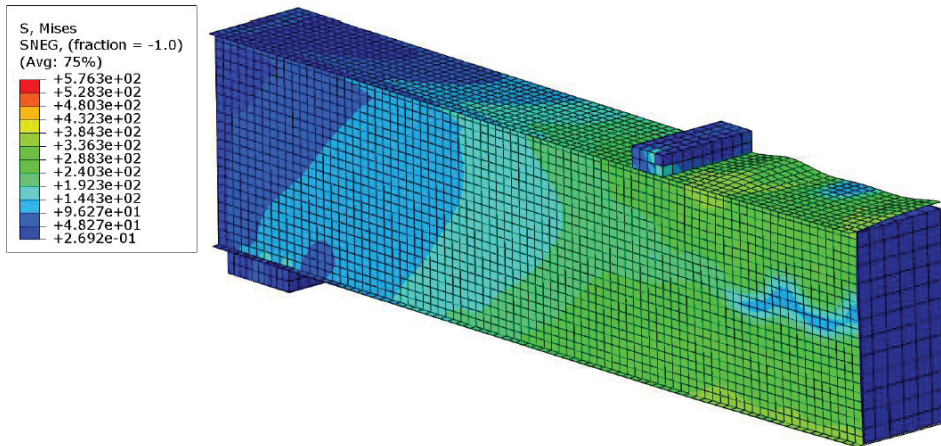


**Fig. 3.21.** Beam B3-1 Von Mises stress (MPa) distributions (outer steel integration points) at the maximum bending moment



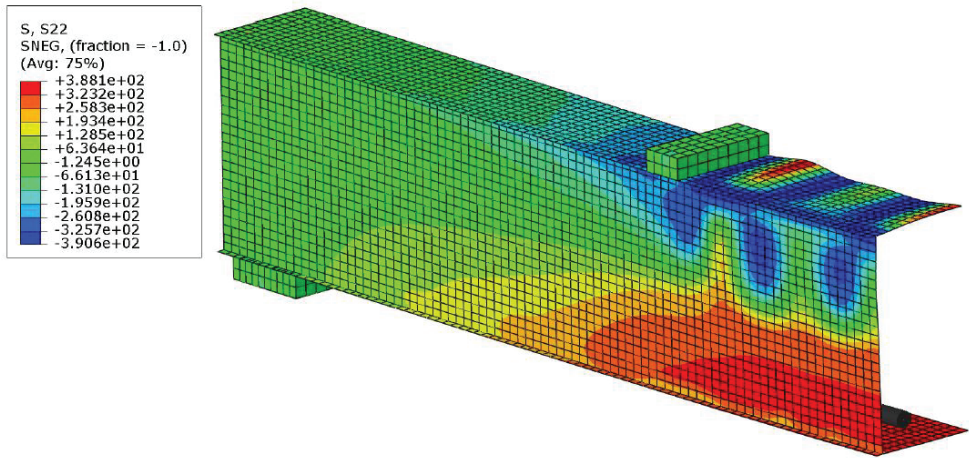


**Fig. 3.22.** Beam B3-1 normal stress (MPa) distributions (outer steel integration points) at the maximum bending moment

Similarly to the columns, steel-concrete separation is observed in the beam models as well. This kind of separation at the maximum bending moment is presented in Fig. 3.23. In this figure, the vertical displacements are plotted.

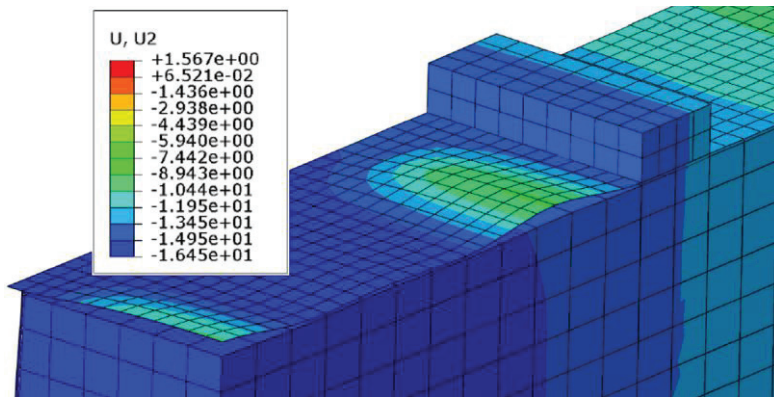


**Fig. 3.23.** Beam B3-1 steel-concrete separation at the ultimate bending moment

Displacements at the ultimate load at the critical section close to the loading plate are plotted in Fig. 3.24. Web separation from the concrete core is visible, but it is less significant than the separation of the compressed flange.



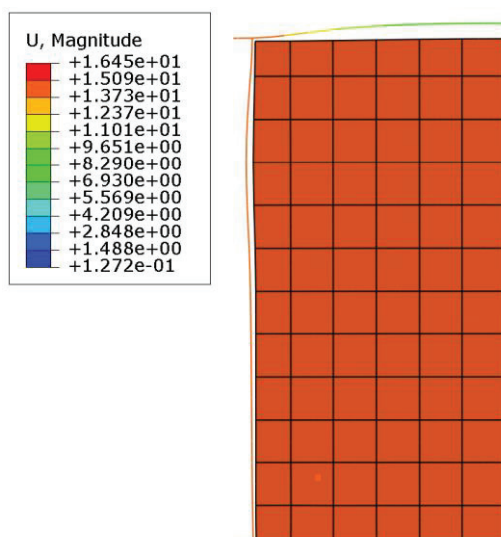


**Fig. 3.24.** Displacements at the critical cross-section of beam B3-1

In order to evaluate the effects of the imperfections for the local buckling behaviour of the compressed flanges, three alternative FE models were created and analysed for each of the beams B3-1 and B4-1. Beam B3-1 had the most slender top flange, while the flange of beam B4-1 was the most compact from the experimentally tested beams. For model type 1, residual stresses were not introduced, and the minimum geometrical imperfection amplitude value of  $B/500$  was used. In model type 2, residual stresses were introduced by using the same  $B/500$  geometrical imperfection amplitude. Model type 3 had residual stresses and a geometrical imperfection amplitude of  $B/200$ . The average normal stress-strain curves of the compressed steel flanges of beams B3-1 and B4-1 are presented in Fig. 3.25 and Fig 3.26, respectively. The results were extracted from the two sections of each model. As the beams had five initial geometrical imperfection half-waves, the results from the middle of the third half-wave in the middle of the beam (section 1) and the first half-wave next to the loading plate (section 2) were analysed. The aforementioned two areas were the main places where the largest buckling waves were observed during the experimental campaign. In order to understand the level of steel panel strength reduction due the local buckling, the idealised bilinear stress strain curves of steel were plotted in the same graphs.

Generally, the results of each pair of two sections from the same model were similar. However, when comparing the different models, the differences of the average normal stress-strain behaviour were obvious. The ultimate average stresses of the top flanges from beam B3-1 models 1, 2 and 3 were 77%, 67% and 62% of the yield strength, respectively. Similarly, the ultimate average stresses of the beam B4-1 top flanges were 92%, 73% and 68% for the different models. As expected, the local buckling was more severe for the more slender flange ( $b/t=79.7$ ) of beam B3-1. When comparing the results of models 1, 2 and 3, the ultimate average normal stresses of the beam B4-1 top flange ( $b/t=59.8$ ) were higher than the respective stresses of the

beam B3-1 top flange by 19%, 9% and 9.5%. It was also determined that the local buckling behaviour was more sharp and sudden for the models with lower level or no imperfections. On the other hand, while the ultimate strength was reduced significantly for model type 3, the strength decrease in the descending branch of the average normal stress-strain curve was very slow and gradual. The high initial geometrical imperfection amplitude of model type 3 ( $B/200$ ) means that the local buckling of the mid-panel area is early, and the edges of this panel are not able to develop high stresses at such low strains. However, in the strain range between 0.01 and 0.02, the differences between the curves of the different models were negligible. At such a high strain, the edges of the panel develop yield stress and, thus, the difference between model types 2 and 3 is negligible within this range.

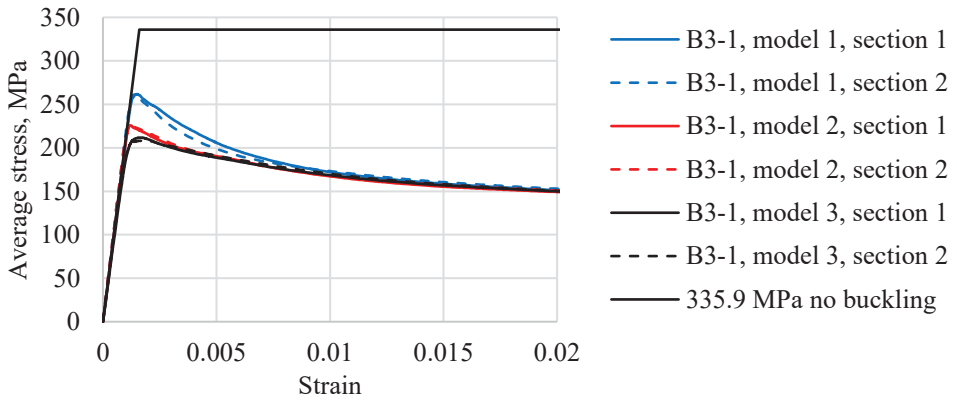


**Fig. 3.25.** Average normal stress-strain curves of beam B3-1 top flange

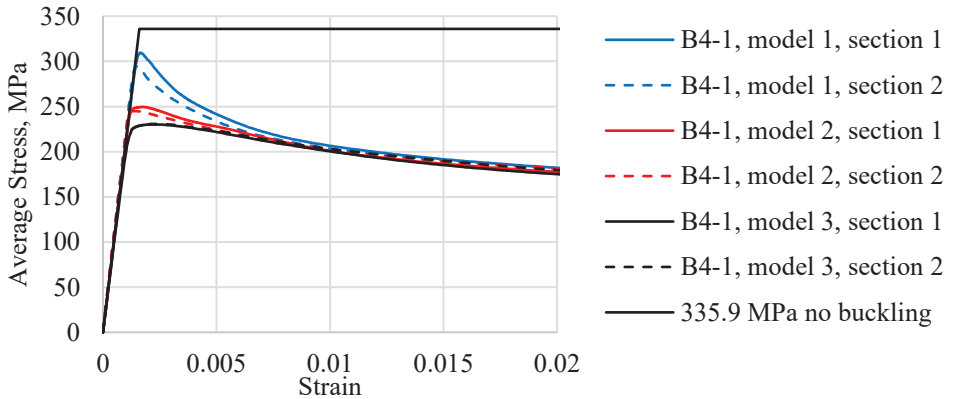


**Fig. 3.26.** Average normal stress-strain curves of beam B4-1 top flange

The compressed flanges of all the six beam types were analysed based on model type 3, which represents the most severe case of initial imperfections. The average normal stress-strain curves were obtained in the two sections of each model and are presented in Fig. 3.27. Similarly to the columns, the shape of such a curve depends on the  $b/t$  ratio of the panel and the yield strength of the steel.

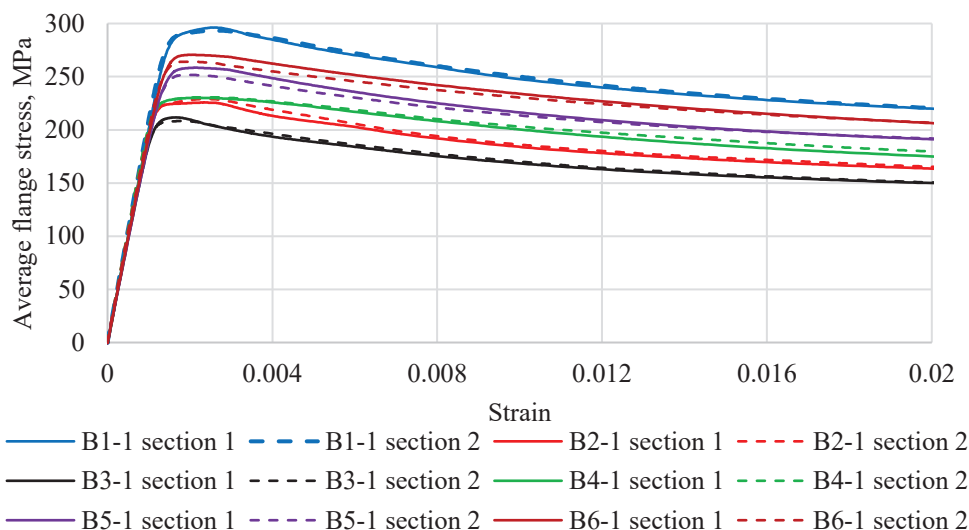


**Fig. 3.27.** Average top flange stress-strain curves of the beams

### 3.3. Proposed average normal-stress strain model for compressed steel flanges in concrete-filled steel structures

Based on the results of the numerical research and experimental observations, an idealised average normal stress-strain model is proposed and presented in Fig. 3.28. In this model, the stress-strain dependency is linear until the critical buckling stress is reached (range 0–A). Furthermore, in the range A–B between the critical stress and the reduced ultimate stress, a reduced stiffness level equal to  $0.6E_s$  can be assumed. In the following range B–C, a reduced ultimate stress level can be assumed as constant. The exact maximum stress is reached in a small interval of strains in the FE analysis. Therefore, this reduction is necessary in order to be able to assume a wider constant stress range. This range is followed by the negative exponential average stress decrease in the range C–D.

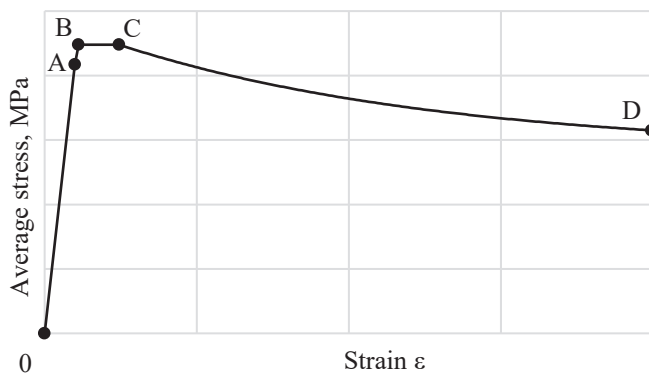


**Fig. 3.28.** Proposed average normal stress-strain model for compressed steel panels

Numerical critical buckling stress results of the columns with three different yield strengths are marked in Fig. 3.29. The proposed critical stress values are plotted as continuous lines. The critical stress values of the panels with intermediate yield strengths are interpolated.

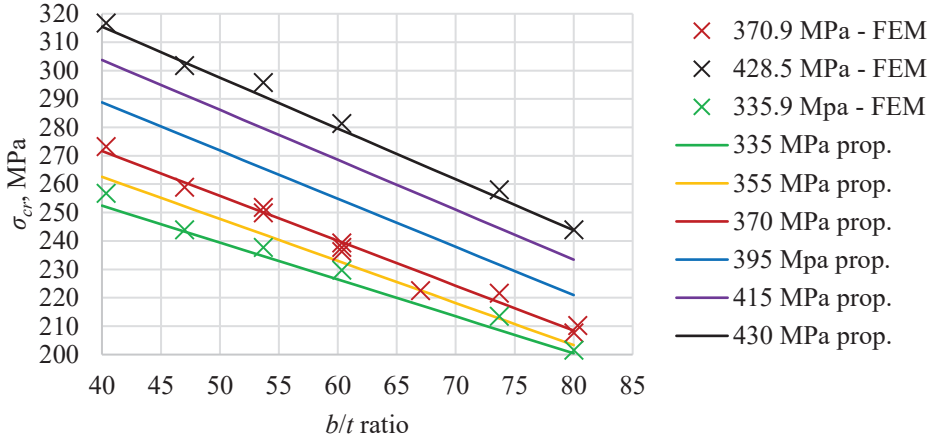


**Fig. 3.29.** Column critical stress- $b/t$  ratio results and proposed curves

The critical stress values for steel panels in concrete-filled thin-walled steel columns can be calculated by using the proposed Expression (3.6). This expression is valid for steel panels with the yield strength in the range between 335 MPa and 430 MPa having the  $b/t$  ratios in the range between 40 and 81.

$$\sigma_{cr,c} = a_{cr,c} \left( \frac{b}{t} \right) + c_{cr,c} \quad (3.6)$$

where:  $a_{cr,c}$  and  $c_{cr,c}$  are the variables in MPa for the critical stress calculation obtained from the proposed Expressions (3.7) and (3.8), respectively.

$$a_{cr,c} = \left( -1.9 + 0.6 \cdot e^{-0.018(f_y - 335)} \right) \cdot 1 \text{ MPa} \quad (3.7)$$

where:  $f_y$  is the yield strength of steel in MPa.

$$c_{cr,c} = 0.87 \cdot f_y + 13 \text{ MPa} \quad (3.8)$$

where:  $f_y$  is the yield strength of steel in MPa.

The ultimate stress results of the analysed panels are marked in Fig. 3.30. The proposed values are plotted by using the continuous lines. It can be seen that two ranges can be distinguished. In the initial  $40 \leq b/t \leq 60$  range, the  $\sigma_u$ - $b/t$  dependency is a negative exponential, whereas a linear dependency is observed in the  $60 < b/t \leq 81$  range.

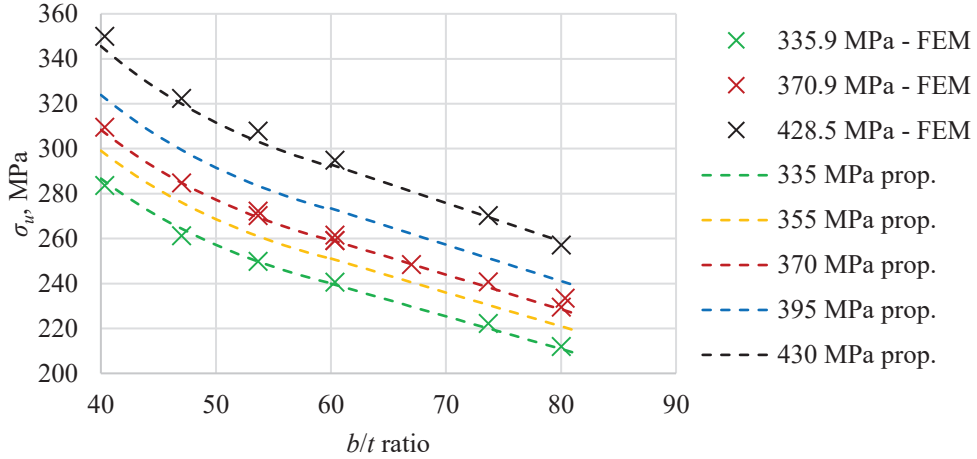


**Fig. 3.30.** Column ultimate stress– $b/t$  ratio results and proposed curves

The ultimate stress values for steel panels in concrete-filled thin-walled steel columns having width-to-thickness ratios in the range between  $40 \leq b/t \leq 60$  can be calculated by using the proposed Expression (3.9).

$$\sigma_{u,c} = a_{u,c} \cdot e^{-0.055\left(\frac{b}{t}-40\right)} + c_{u,c} \quad (3.9)$$

where:  $a_{u,c}$ , is the variable in MPa calculated from the proposed Expression (3.10);  $c_{u,c}$  is the variable in MPa calculated from the proposed Expression (3.11).

$$a_{u,c} = 0.11 \cdot f_y + 33 \text{ MPa} \quad (3.10)$$

where:  $f_y$  is the yield strength of steel in MPa.

$$c_{u,c} = 0.51 \cdot f_y + 46 \text{ MPa} \quad (3.11)$$

where:  $f_y$  is the yield strength of steel in MPa.

Alternatively, a different maximum stress expression is proposed for column panels having width-to-thickness ratios in the range between  $60 < b/t \leq 81$ :

$$\sigma_{u,c} = a_{u,c,l} \left( \frac{b}{t} \right) + c_{u,c,l} \quad (3.12)$$

where:  $a_{u,c,l}$  and  $c_{u,c,l}$  are the variables in MPa calculated from the proposed Expressions (3.13) and (3.14), respectively.

$$a_{u,c,l} = -0.0027 \cdot f_y - 0.55 \text{ MPa} \quad (3.13)$$

where:  $f_y$  is the yield strength of steel in MPa.

$$c_{u,c,l} = 0.72 \cdot f_y + 86 \text{ MPa} \quad (3.14)$$

where:  $f_y$  is the yield strength of steel in MPa.

The calculated ultimate average stress value must be reduced when calculating the idealised average normal stress-strain curve. The maximum stress is reached at a specific strain value. However, there is a strain range where the stress close to the ultimate stress value can be assumed as constant. This strain range can be marked as  $\varepsilon_{u,1} < \varepsilon \leq \varepsilon_{u,2}$ . The strain values  $\varepsilon_{u,1}$  and  $\varepsilon_{u,2}$  correspond to points B and C of the proposed idealised model, respectively. Therefore, in order to obtain the reduced constant ultimate stress value for this range, the ultimate strength value  $\sigma_{u,c}$  has to be reduced via the use of the reduction factor  $k_{red}$ . According to the results of the FE analysis, as shown in Fig. 3.27, the stress reduction in the post-maximum stress range was found to be sharper and more sudden for steel panels featuring a high width-to-thickness ratio. On the other hand, the panels with low  $b/t$  ratios maintained higher stress values across a relatively broad range. Therefore, the values of the reduction factor are lower for the steel panels with high  $b/t$  ratios. This leads to a higher reduction of the ultimate stress. The reduction factor and the reduced ultimate stress can be calculated from the proposed Expressions (3.15) and (3.16), respectively.

$$k_{red} = \begin{cases} 0.975 & \text{for } 40 \leq \frac{b}{t} \leq 51 \\ -0.00035 \left( \frac{b}{t} \right) + 0.988 & \text{for } 51 < \frac{b}{t} \leq 81 \end{cases} \quad (3.15)$$

$$\sigma_{u,c,red} = \sigma_{u,c} \cdot k_{red} \quad (3.16)$$

Strain  $\varepsilon_{u,1}$  can be obtained once the critical and reduced ultimate stresses are known. Strain  $\varepsilon_{u,2}$  can be calculated from the proposed Expression (3.17).

$$\varepsilon_{u,2} = \varepsilon_{u,1} \cdot k_s \quad (3.17)$$

where:  $k_s$  is the strain ratio calculated from the proposed Expression (3.18) for steel panels having width-to-thickness ratios in the range between  $40 \leq b/t < 81$ .

$$k_s = \begin{cases} -0.005 \left( 60 - \frac{b}{t} \right)^2 + 0.225 \left( 60 - \frac{b}{t} \right) + 2.34 & \text{for } 40 \leq \frac{b}{t} < 60 \\ -0.007 \left( \frac{b}{t} \right) + 2.76 & \text{for } 60 \leq \frac{b}{t} \leq 81 \end{cases} \quad (3.18)$$

Once the strain value  $\varepsilon_{u,2}$  is exceeded, the average stress of the steel panel decreases. The stresses in the descending branch of the proposed model can be calculated by using the proposed Expression (3.19).

$$\sigma(\varepsilon) = (\sigma_{u,red} - j_2) + j_2 \cdot e^{j_1(\varepsilon - \varepsilon_{u,2})} \quad (3.19)$$

where:  $j_1$  is a variable in MPa taking into account the specific  $b/t$  ratio of a steel panel calculated from the proposed Expression (3.20);  $j_2$  is the variable in MPa taking into account the effects of the specific yield strength of a steel panel calculated from the proposed Expression (3.21).

$$j_1 = \begin{cases} -70 \text{ MPa} & \text{for } 40 \leq \frac{b}{t} \leq 56 \\ \left(-13.9 - \frac{b}{t}\right) \cdot 1 \text{ MPa} & \text{for } 56 < \frac{b}{t} \leq 81 \end{cases} \quad (3.20)$$

$$j_2 = 75 \text{ MPa} + \frac{20(f_y - 335 \text{ MPa})}{95} \quad (3.21)$$

where:  $f_y$  is the yield strength of steel in MPa.

Due to the curvature of the flexural beam elements, different expressions for the critical stress and the ultimate average stress calculation are proposed for this case. The following expressions are valid for the steel yield strengths in the range between 335–430 MPa and panels with  $b/t$  ratios in the range between 60–81.

Similarly to the columns, critical stress values of the analysed steel panels were found via the method of Liang *et al.* [53] based on the results of the finite element analysis. The results are summarised in Fig. 3.31. In this case, the beams with the yield strengths equal to 335.9 MPa and 428.5 MPa were analysed, and the results of such beams are marked. The proposed critical stress values are plotted as continuous lines. Critical stress values of the panels with intermediate yield strengths are interpolated.

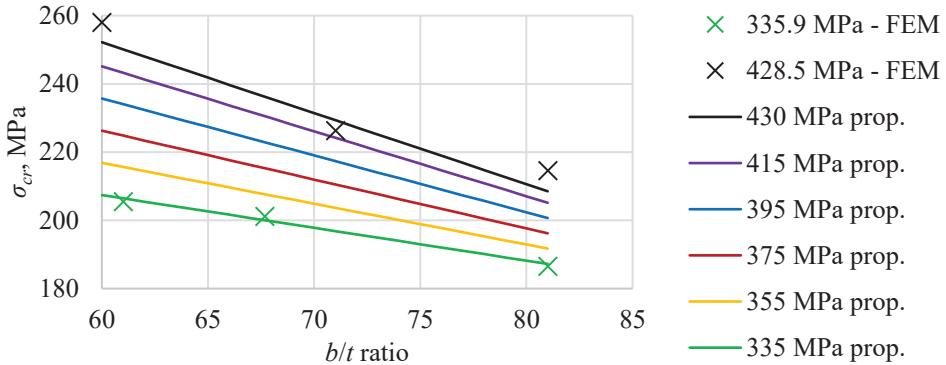


**Fig. 3.31.** Beam critical stress- $b/t$  ratio results and proposed curves

The critical stress values for compressed steel panels in concrete-filled thin-walled welded steel beams can be calculated by using the proposed Expression (3.22). This expression is only valid within the previously shown model validity limits.

$$\sigma_{cr,b} = a_{cr,b} \left( \frac{b}{t} \right) + c_{cr,b} \quad (3.22)$$

where:  $a_{cr,b}$  and  $c_{cr,b}$  are variables in MPa calculated from the proposed Expressions (3.23) and (3.24), respectively.

$$a_{cr,b} = -0.96 \text{ MPa} - \frac{1.12(f_y - 335 \text{ MPa})}{95} \quad (3.23)$$

where:  $f_y$  is the yield strength of steel in MPa.

$$c_{cr,b} = 265 \text{ MPa} + \frac{112(f_y - 335 \text{ MPa})}{95} \quad (3.24)$$

where:  $f_y$  is the yield strength of steel in MPa.

The ultimate stress results of compressed flanges are marked in Fig. 3.32. The proposed values are plotted by using the continuous lines. The ultimate stress values of panels with intermediate yield strengths are interpolated.

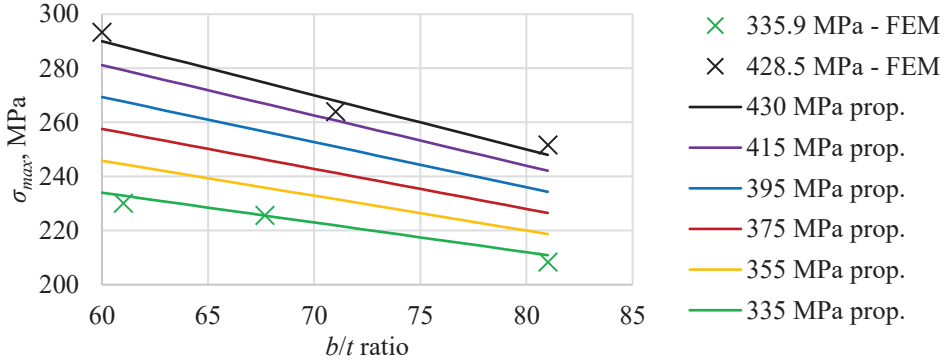


**Fig. 3.32.** Beam ultimate stress- $b/t$  ratio results and proposed curves

The ultimate stress values for steel panels in concrete-filled thin-walled welded steel beams can be calculated by using the proposed Expression (3.25). This expression is only valid within the previously shown model validity limits.

$$\sigma_{u,b} = a_{u,b} \left( \frac{b}{t} \right) + c_{u,b} \quad (3.25)$$

where:  $a_{u,b}$  and  $c_{u,b}$  are variables in MPa calculated from the proposed Expressions (3.26) and (3.27), respectively.

$$a_{u,b} = -1.1 \text{ MPa} - \frac{0.9(f_y - 335 \text{ MPa})}{95} \quad (3.26)$$

where:  $f_y$  is the yield strength of steel in MPa.

$$c_{u,b} = 300 \text{ MPa} + \frac{110(f_y - 335 \text{ MPa})}{95} \quad (3.27)$$

where:  $f_y$  is the yield strength of steel in MPa.

The values of the reduction factor  $k_{red}$ , the reduced ultimate stress, the strain ratio  $k_s$ , and the descending branch of the average normal stress-strain curve are calculated in the same way as in the previously proposed model for columns.



### 3.4. Iterative layer method for stress-strain analysis of thin-walled steel-concrete beams

In-depth analysis of structural beam members requires iterative methods to be used. As an alternative for the finite element method, one of the general methods that is applicable for this case is the iterative layer method. The original version of this method was proposed in a publication of Augonis and Zadlauskas [5]. This method was originally used for the analysis of the flexural behaviour of reinforced concrete elements. In this research, this method was adapted for the case of concrete-filled steel beams. The general expression of the iterative layer method is presented as follows:

$$[E]\{\varepsilon\} = \{F\} \quad (3.28)$$

where:  $[E]$  is the stiffness matrix of the cross-section assembled as shown in Expression (3.29);  $\{\varepsilon\}$  is the vector of deformations assembled as shown in Expression (3.30);  $\{F\}$  is the load vector assembled as shown in Expression (3.31).

$$[E] = \begin{bmatrix} 1 & -2 & 1 & 0 & \dots & 0 & 0 & 0 \\ 0 & 1 & -2 & 1 & \dots & 0 & 0 & 0 \\ 0 & 0 & 1 & -2 & \dots & 0 & 0 & 0 \\ \dots & \dots & \dots & \dots & \dots & \dots & \dots & \dots \\ 0 & 0 & 0 & 0 & \dots & -2 & 1 & 0 \\ 0 & 0 & 0 & 0 & \dots & 1 & -2 & 1 \\ (EA)_1 & (EA)_2 & (EA)_3 & (EA)_4 & \dots & (EA)_{n-2} & (EA)_{n-1} & (EA)_n \\ 0 & (EA)_2 d & 2(EA)_3 d & 3(EA)_4 d & \dots & (n-3)(EA)_{n-2} d & (n-2)(EA)_{n-1} d & (n-1)(EA)_n d \end{bmatrix} \quad (3.29)$$

where:  $(EA)_i$  is the sum of axial stiffness of the different materials constituting the layer;  $d$  is the height of one layer.

$$\{\varepsilon\} = \{\varepsilon_1 \quad \varepsilon_2 \quad \varepsilon_3 \quad \varepsilon_4 \quad \varepsilon_5 \quad \varepsilon_6 \quad \dots \quad \varepsilon_n\}^T \quad (3.30)$$

where:  $\varepsilon_i$  is the strain of the layer.

$$\{F\} = \{0 \quad 0 \quad 0 \quad 0 \quad 0 \quad 0 \quad \dots \quad M\}^T \quad (3.31)$$

where:  $M$  is the external bending moment.

The thickness of a layer was assumed to be equal to the flange thickness. The experimental beams were analysed in this chapter. Thus, the layer thickness was assumed as 3 mm or 4 mm. The height of the beam analysed via the layer method was assumed as the multiple of the layer height  $d$ . Initially, different thicknesses of the layers were tested. However, no strong result dependency on the layer thickness was observed.

Furthermore, three expressions for the calculation of the axial stiffness sum  $(EA)_i$  of the different layers were used. Expression (3.32) was used for the first layer from the top and the bottom of the beam. Expression (3.33) was used for the intermediate layers consisting of concrete and steel webs. Expression (3.34) was used for the layer where the centre of the reinforcement was placed:

$$(EA)_i = W \cdot d \cdot E_s \quad (3.32)$$

where:  $W$  is the full width of a beam including the steel ledges.

$$(EA)_i = d(2 \cdot t \cdot E_s + b \cdot E_c) \quad (3.33)$$

where:  $A_{sr}$  is the sum of the cross-sectional areas of reinforcement bars.

$$(EA)_i = d(2 \cdot t \cdot E_s + b \cdot E_c) + A_{sr} \cdot E_{sr} \quad (3.34)$$

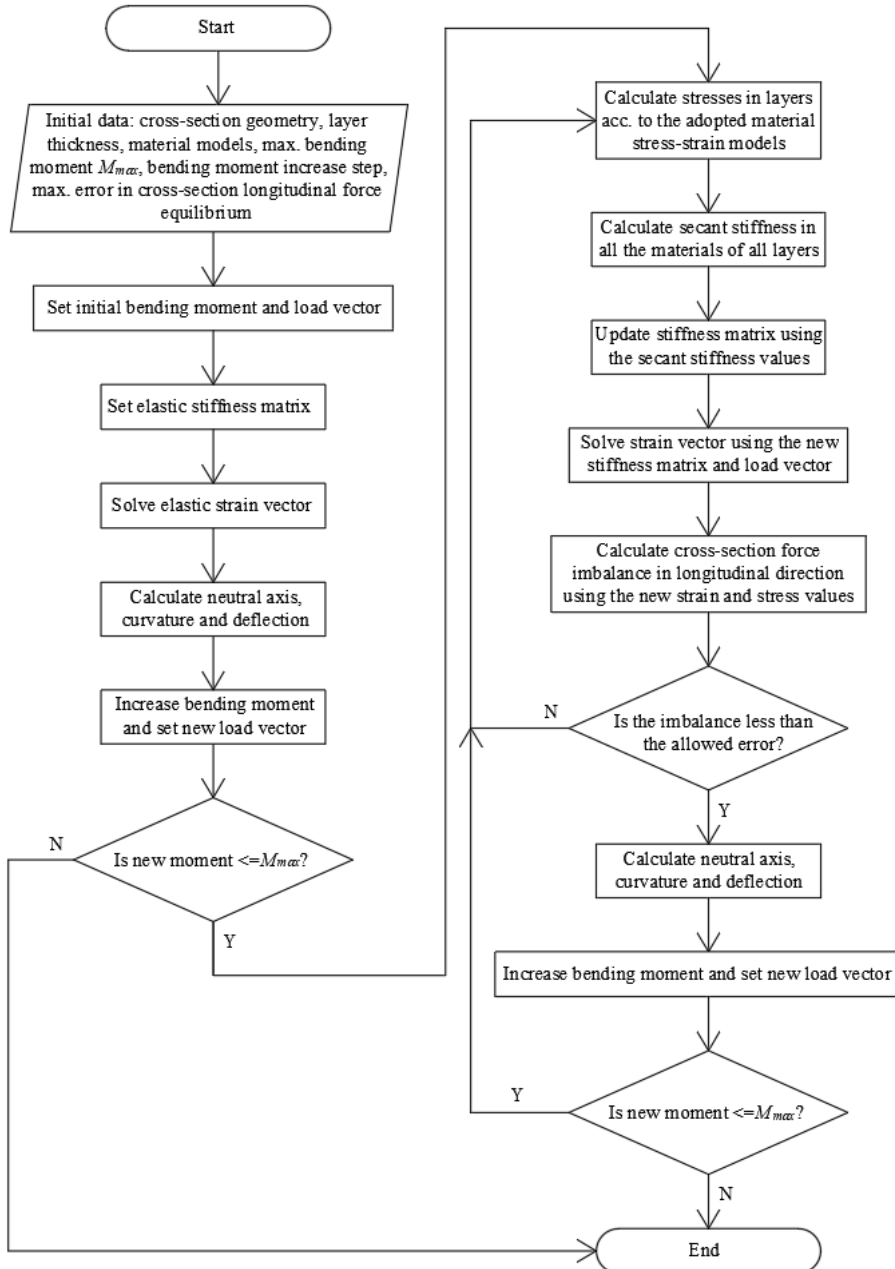


Fig. 3.33. Algorithm of the calculations via the iterative layer method

The iterative layer method is based on the following assumption. When analysing the three adjacent layers, the average strain of the outer layers is equal to the strain of the middle layer. The iterations are repeated, and the strains of the layers are recalculated in every iteration. The stresses of the materials and the corresponding resultants of the axial forces are subsequently recalculated in every layer in accordance with the recalculated values of strains. At the end of every iteration, the axial force equilibrium is checked. The maximum allowed value of error is set initially, and the iterations are stopped once this error becomes lower than the set value. In order to obtain the bending moment-displacement curve with multiple points, the bending moment is increased by 2–4% of the initially set maximum bending moment value in every course of iterations. Expressions of the iterative layer method were inserted into the software *Mathcad*. The algorithm of this method is shown in Fig. 3.33.

In order to model the stress-strain behaviour of reinforcement, the idealised bilinear elastoplastic stress-strain curve with no strain hardening was adopted. The stress-strain model of structural steel modified according to Song *et al.* [82] in order to take into account the residual stresses was used for the webs and the bottom flange in tension. The general shape of this model was presented in Fig. 3.1 a). The idealised stress-strain model for compressed flanges undergoing local buckling was developed in Chapter 3.3. This model is also used for the calculations using the iterative layer method.

The stress-strain model for the compressive and tensile behaviour of concrete is presented in Fig. 3.34. The effects of concrete confinement due to passive pressure provided by the steel profile have to be taken into account when analysing the compressive stress-strain behaviour of concrete. A combination of two confined concrete models according to Liang [49] was used in this case. The initial compressive part 0A of the curve was modelled according to the model of Mander *et al.* [58]. The remaining part of the stress strain curve was based on the model of Tomii and Sakino [85]. The tensile strength of concrete was calculated by using the following Expression (3.35) from Eurocode 2 [26]:

$$f_{ctm} = 0.3(f_{cm} - 8)^{(2/3)} \quad (3.35)$$

The following Expression (3.36) from Eurocode 2 [26] was used to calculate the 95% percentile of concrete tensile strength:

$$f_{ctk,0.95} = 1.3f_{ctm} \quad (3.36)$$

The ultimate tensile strain  $\varepsilon_{tu}$  was assumed to be 10 times higher than the concrete strain at cracking  $\varepsilon_{ct}$  based on the research of Liang [49].

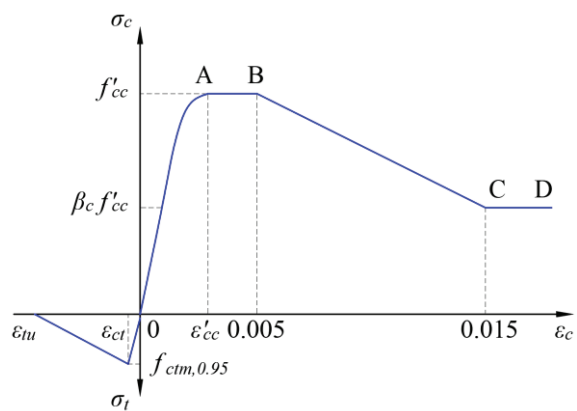


**Fig. 3.34.** Material model of confined concrete according to Liang [49]

### 3.5. Conclusions of Chapter Three

1. The theoretical ultimate strength results of the columns showed great agreement with the experimental results. The average experimental to theoretical ultimate strength ratios  $N_{u,ex}/N_u$  varied in the range between 0.95–0.97 for the W type columns, while the average values of 0.98–1.02 were obtained for the WO type columns. The best agreement with the experimental results was obtained when using the method of Liang and Uy where the average strength overestimation was the lowest for the W type columns, and the moderate strength reserve was obtained for the WO type columns.
2. The average normal stress-strain curves were obtained via FE analysis. The shape of such a curve depends on the width-to-thickness ratio of the panel and the initial imperfections. Based on the results of beams B3-1 and B4-1, compressed beam flanges with a low level of imperfections had 24–35% higher ultimate strength than those with a high level of imperfections. More slender panels with a lower level of imperfections buckled more suddenly. However, in the strain range between 0.01–0.02, the descending branches of such curves of the same beams were similar, independently from the level of the initial imperfections. Finally, panels with large imperfections and  $b/t$  ratios of 59.8 and 79.7 had ultimate stresses equal to 68% and 62% of the steel yield strength, respectively.
3. The average normal stress-strain model for compressed steel panels in concrete-filled welded steel structures was proposed. Two separate cases for the calculation of the critical buckling stress and the ultimate stress are distinguished: compressed flanges of columns and beams. When using the set of proposed expressions, the idealised average normal stress-strain curve can be obtained. Specific ranges of the proposed curve are distinguished: the linear pre-buckling range, the reduced stiffness range between the critical buckling stress and the ultimate stress, the constant ultimate stress-range, and the negative exponential descending branch.
4. The ultimate axial strength contribution of the steel profile and the concrete core of column 2-WO ( $b/t=77$ ) was obtained at a similar strain. When analysing beam B3-1 ( $b/t=80$ ), the ultimate average normal stress of the compressed flange was obtained at 76% of the ultimate bending moment. The average stress of this flange decreased to 84% of the ultimate average normal stress at the maximum bending moment. Thus, the proposed average normal stress-strain model is very beneficial for the in-depth analysis of such structures.

## IV. RESULTS

### 4.1. Results of thin-walled steel-concrete columns

The theoretical and experimental results of steel-concrete columns are compared in this chapter. The experimental results, the theoretical results based on the method of Liang and Uy [48], the theoretical results based on the expressions proposed in Chapter 3.3, and the numerical results of the ultimate column strengths are summarised in Table 4.1. Generally, the ultimate strengths obtained via finite element analysis were slightly higher compared to the experimental results. It is also obvious that the numerical and theoretical ultimate strengths were relative to each other. It can be explained by the fact that the theoretical results are based on the experimentally obtained material parameters. On the other hand, the experimental results depend on a variety of random factors: concrete strength and imperfection shape uncertainty, small random load eccentricities, etc. Protrusions of the concrete surface above the steel edges may also lead to pre-stressing of concrete before loading the steel profile. This could lead to a small reduction of the column ultimate strength, as reported by Martinavičius *et al.* [64]. The set of the aforementioned factors leads to the differences between the experimental and the theoretical results. In some cases, the experimental strength was overestimated by up to 9%, while, in other cases, the strength was underestimated by up to 11% compared to the theoretical results.

**Table 4.1.** Comparison of experimental, numerical and theoretical ultimate strength results of the columns

Column marking	$N_{u,ex}$ , kN	$N_{u,FE}$ , kN	$N_{u,Liang,Uy}$ , kN	$N_{u,proposed}$ , kN	$N_{u,ex}/N_{u,FE}$	$N_{u,ex}/N_{u,Liang,Uy}$	$N_{u,ex}/N_{u,proposed}$
1-WO	1682.6	1724.0	1684.4	1668.2	0.98	1.00	1.01
2-WO	1930.5	1974.2	1886.4	1880.5	0.98	1.02	1.03
3.1-WO	1612.1	1696.6	1663.2	1623.0	0.95	0.97	0.99
4-WO	1184.2	1117.9	1120.6	1106.2	1.06	1.06	1.07
5-WO	1543.7	1643.1	1587.9	1586.9	0.94	0.97	0.97
6-W	1358.4	1498.0	1458.9	1427.9	0.91	0.93	0.95
7-WO	1343.2	1213.0	1216.5	1184.5	1.11	1.10	1.13
8-WO	1112.0	999.3	1011.6	993.6	1.11	1.10	1.12

The results of Table 4.1 are also presented as a chart in Fig. 4.1. It was determined that the experimental ultimate strengths of the columns consisting of the most slender steel panels (1-WO, 2-WO, 3-WO, 5-WO) were slightly lower than the numerical ultimate strengths. On the other hand, the most compact columns (7-WO, 8-WO) had higher experimental ultimate strengths compared to the results of the theoretical research. It is likely that the confinement effect for the slender cross-sections is slightly overestimated during the numerical analysis, while, for the most compact cross-sections, a slight underestimation is observed. Similar tendencies were observed when comparing the experimental results and the theoretical calculation results. The ultimate strengths of the most slender columns were predicted very accurately. On the other hand, the theoretically calculated ultimate strengths of the most compact columns tend to be slightly conservative. Thus, it is expected that the

most compact columns analysed in this research had a slightly increased concrete strength due to confinement, although it is usually assumed that no concrete strength increase should be present in the cross-section  $b/t$  range analysed in this research. It was also determined that the results obtained via the proposed method were relatively accurate in comparison to the other methods. The results were in most cases similar to the results obtained via the method of Liang and Uy [48], but were found to be slightly more conservative.

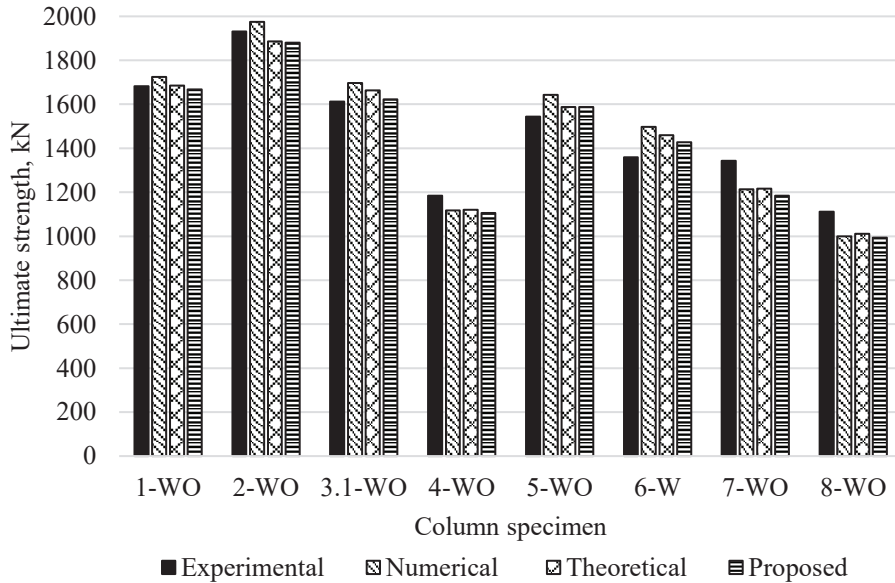


**Fig. 4.1.** Comparison of column ultimate strength results

The critical stresses of the theoretical steel panels with different  $b/t$  ratios were calculated by using the method of Liang *et al.* [53] according to Expression (1.23). Alternatively, the critical stresses were also calculated by using the proposed Expression (3.6). Various yield strengths of steel were used. Such results and ratios between the critical stresses obtained by using different methods are presented in Table 4.2. The graphical presentation of Table 4.2 results is shown in Fig. 4.2. It is obvious that the method of Liang *et al.* [53] is very conservative in comparison to the proposed method. The ratios of critical stresses obtained by the method of Liang *et al.* [53] and the critical stresses obtained by the proposed method varied within the range between 0.55–0.75 for the panels of the 335 MPa yield strength. On the other hand, such ratios were in the range between 0.69–0.83 for the 430 MPa yield strength panels. The critical stress ratios were the highest for the steel panels having a low  $b/t$  ratio. Such result differences may be explained by the fact that the two methods were created very differently. In the research of Liang *et al.* [53], clamped steel panels with 0.1*t* imperfection amplitudes were analysed. The method was created based on those results. In this research, three-dimensional steel-concrete models were created, and the imperfection amplitude of  $B/200$  was adopted. It was shown in this research that the shape of the stress-strain curve of the steel panel depends on the level of initial

imperfections. Furthermore, it is expected that the results of the full steel-concrete models would be more accurate. The statement that the behaviour of the clamped steel panel represents the behaviour of the steel panel in the steel-concrete structure is merely an assumption in order to simplify the analysis.

**Table 4.2.** Comparison of critical stress results

$b/t$	$\sigma_{cr,imp}$ , MPa	$\sigma_{cr,prop}$ , MPa	$\sigma_{cr,imp}/$ $\sigma_{cr,prop}$	$\sigma_{cr,imp}$ , MPa	$\sigma_{cr,prop}$ , MPa	$\sigma_{cr,imp}/$ $\sigma_{cr,prop}$	$\sigma_{cr,imp}$ , MPa	$\sigma_{cr,prop}$ , MPa	$\sigma_{cr,imp}/$ $\sigma_{cr,prop}$
	$f_y=335$ MPa			$f_y=370$ MPa			$f_y=430$ MPa		
40	199.9	267.9	0.75	224.7	272.3	0.83	260.5	315.4	0.83
45	195.6	263.8	0.74	219.9	264.4	0.83	254.9	306.5	0.83
50	189.9	259.8	0.73	213.5	256.5	0.83	247.5	297.5	0.83
55	182.9	255.8	0.72	205.7	248.5	0.83	238.4	288.6	0.83
60	174.6	251.8	0.69	196.3	240.6	0.82	227.6	279.6	0.82
65	165.1	247.7	0.67	185.6	232.7	0.80	215.1	270.7	0.80
70	154.3	243.7	0.63	173.4	224.7	0.77	201.0	261.7	0.77
75	142.2	239.7	0.59	159.9	216.8	0.74	185.3	252.7	0.74
80	129.0	235.6	0.55	145.1	208.9	0.69	168.1	243.8	0.69

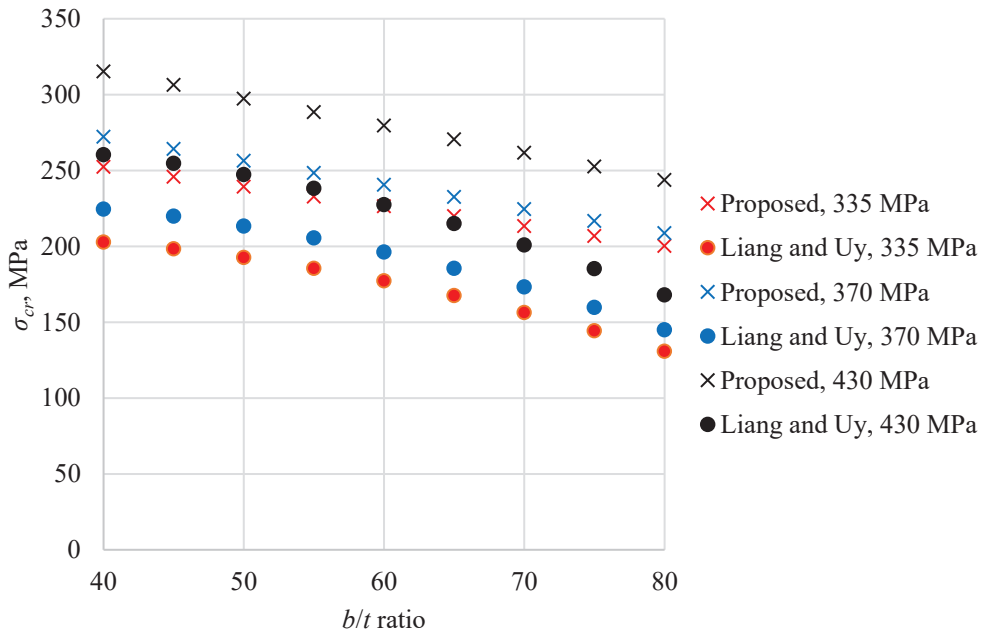


**Fig. 4.2.** Critical stress results

Based on the proposed model, the average normal stress-strain curves were obtained for column flanges with the yield strength of 370 MPa and the  $b/t$  ratios in the range between 40–80. The latter curves are presented in Fig. 4.3. However, it is important to note that the proposed model is also valid for the steel panels having  $b/t$  ratios in the range between 40–81 and the steel yield strengths in the range between 335–430 MPa.



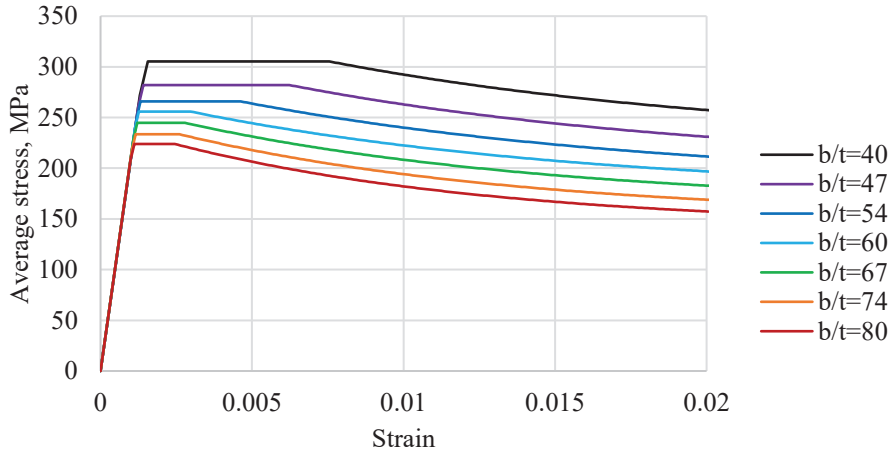


**Fig. 4.3.** Idealised average normal stress-strain curves of column flanges ( $f_y=370$  MPa)

#### 4.2. Results of thin-walled steel-concrete beams

In this chapter, the results obtained via the iterative layer method and the finite element analysis are compared to the experimental results. Based on the proposed model, the average normal stress-strain curves are obtained for the steel grades S355 and S420 and are presented in Fig. 4.4. It can be seen that the normal stress-strain behaviour of the S355 grade panel with the  $b/t$  ratio equal to 60 is very similar to the behaviour of the S420 grade panel with the  $b/t=80$  until the end of the ultimate stress range. However, the descending branch of the more slender panel with the higher steel grade showed a more sudden decrease of the average stress.

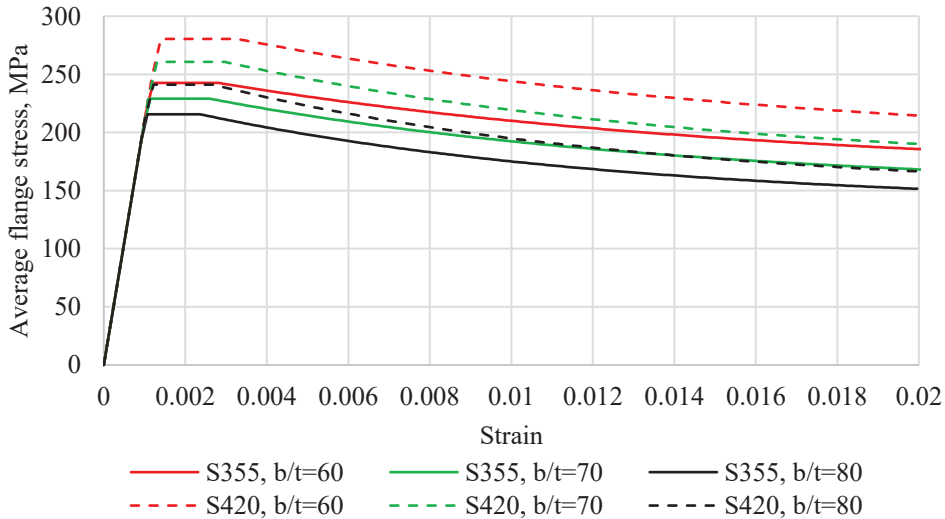


**Fig. 4.4.** Idealised average top flange stress-strain curves of beams

The finite element and the iterative layer methods were used to obtain the moment-deflection curves of the four experimental beams. The aforementioned

results are shown and compared to the experimental results in Fig. 4.5. In this figure, the results of the two alternative FE models for every beam are presented. The first FE model included the geometrical imperfections with the amplitude  $B/200$  and the effects of residual stresses. In the second FE model of every beam, the residual stresses were not considered, and the imperfection amplitude value of  $B/500$  was used. Due to the low level of geometrical imperfections and the residual stresses not being considered, the second FE model is referred to as the model with no imperfections. For the analysis via the iterative layer method, the average normal stress-strain curve of the compressed flange proposed in this chapter was used. For the remaining steel cross-section elements, the stress-strain curve presented in Fig. 3.1 a) was used.

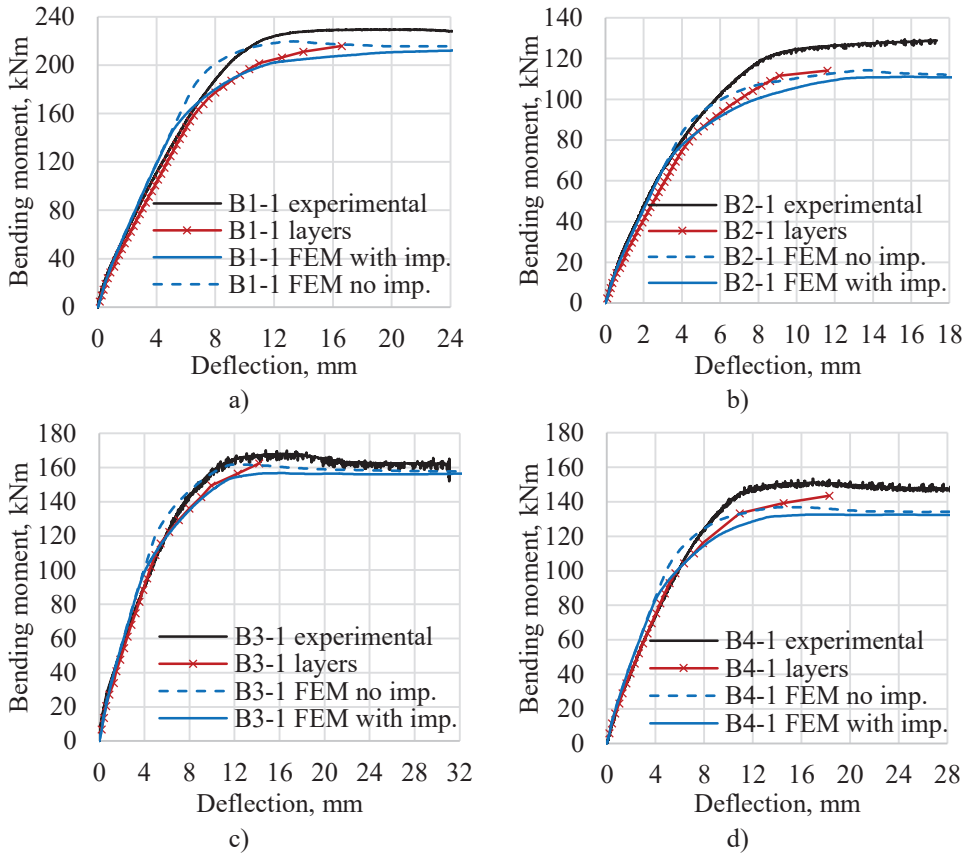


**Fig. 4.5.** Bending moment-deflection curves of the experimental beams: a) B1-1; b) B2-1; c) B3-1; d) B4-1

The theoretical moment-deflection curves of the beams showed good overall agreement with the experimental results. In some cases, the theoretical ultimate bending moment values were slightly conservative with the experimental values being up to 15% higher. As expected, the introduction of residual stresses led to an early decrease of the beam stiffness. However, even the FE models with no imperfections had a slightly lower resistance compared to the experimental resistance values. Therefore, it is likely that the main reason for the relatively high experimental

strengths may be the concrete confinement. The uniaxial confined concrete model used for the iterative layer method assumes that the confinement provided by the rectangular steel cross-section does not increase the concrete strength effectively. During the finite element analysis, the tri-axial behaviour of concrete is accounted for by the use of the plasticity parameters of the CDP model. However, it is possible that the concrete of the experimental beams may reach higher stress values than those provided by the aforementioned models.

The maximum bending moments of the beams are summarised in Table 4.3, where  $M_{u,ex}$  is the experimental maximum bending moment,  $M_{u,FE,imp}$  is the numerical maximum bending moment with the initial imperfections taken into account,  $M_{u,FE}$  is the numerical maximum bending moment without the initial imperfections, and  $M_{u,it}$  is the maximum bending moment obtained via the iterative layer method. The ratios between the experimental and the theoretical maximum bending moments are presented. The average ratios are calculated for the different methods. It was found that the maximum average ratio of 1.11 was obtained when using the FE analysis without the initial imperfections. A slight increase of accuracy and the ratio of 1.08 was obtained by taking into account the imperfections via FE analysis. The most accurate method was found to be the iterative layer method, where the proposed average normal stress-strain model for the compressed flanges was used. The average experimental maximum bending moment to the theoretical maximum bending moment ratio was 1.07. The graphical presentation of the bending moment results is shown in Fig. 4.6

**Table 4.3.** Comparison of the experimental, numerical and iterative layer method maximum bending moment results of the beams

	$M_{u,ex}$ , kNm	$M_{u,FE,imp}$ , kNm	$M_{u,FE}$ , kNm	$M_{u,it}$ , kNm	$M_{u,ex}/$ $M_{u,FE,imp}$	$M_{u,ex}/$ $M_{u,FE}$	$M_{u,ex}/$ $M_{u,it}$
B1-1	229.6	212.3	219.7	216.0	1.08	1.04	1.06
B2-1	131.1	111.1	114.3	114.1	1.15	1.13	1.12
B3-1	170.2	156.8	161.8	162.4	1.08	1.05	1.05
B4-1	153.3	133.1	136.9	143.5	1.13	1.11	1.06
Average ratio					1.11	1.08	1.07

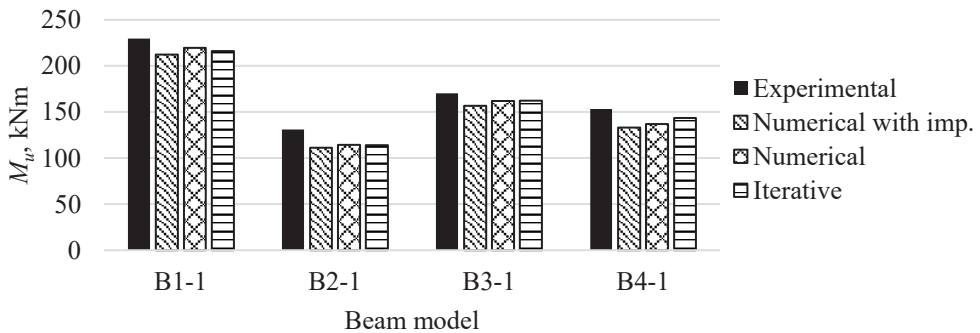


**Fig. 4.6.** Maximum bending moments of the beams obtained via the experimental, numerical and iterative layer methods

### 4.3. Conclusions of Chapter Four

1. The experimental column ultimate strengths corresponded well to the theoretical results. In separate cases, the experimental to numerical ultimate strength ratios varied in the range between 0.91–1.11. Similarly, the experimental to theoretical Liang and Uy method ultimate strength ratios varied in the range between 0.93–1.06, while the experimental to theoretical proposed method ratios were in the range between 0.95–1.07. While the results obtained when using the proposed method were more conservative in separate cases in comparison to the other methods, the lowest strength overestimation level was observed.
2. The ratios between the critical stress obtained via the method of Liang and Uy and the critical stress calculated when using the proposed method were 0.55–0.75 for the steel panels of the 335 MPa yield strength, while the 0.69–0.83 ratios were obtained for the 430 MPa yield strength steel panels. Such stress ratios were higher for the steel panels having a low width-to-thickness ratio.
3. The experimental, numerical and iterative layer method bending moment-deflection curves corresponded well. The least accurate method to predict the maximum bending moment was the numerical analysis without the evaluation of the initial imperfections. The experimental maximum bending moment values on average were 11% higher than the values obtained when using this method. The evaluation of the initial imperfections reduced this difference to 8%. However, the most accurate method to predict the maximum bending moment was the iterative layer method which takes into account the proposed average normal stress-strain model for the compressed flanges. The experimental values were 7% higher on average compared to the results obtained when using this method.

## CONCLUSIONS

1. It was found during the literature review that the newest research of concrete-filled steel structures is heavily focused on the use of high strength materials, the structural behaviour in elevated temperatures, the development of new types of cross-sections where some cross-section parts are susceptible to local buckling, and specific parts of the concrete core remain effectively confined. Such structures require the iterative methods to be used. The critical buckling stress, the ultimate stress and the effective width expressions for steel panels in steel-concrete structures were proposed by different authors. However, those expressions cannot be applied for the iterative methods easily. Effective width development is usually assumed to be linear from the critical stress to the ultimate stress, and the effective width decrease is usually not considered. It does not correspond to the exact behaviour of thin-walled steel panels.
2. Based on the experimental results of the steel-concrete columns and beams, it was found that:
  - a) the average column steel profile  $A_{eff}/A_s$  ratio reduction due to the poor bond conditions was 12%.
  - b) the failure of the columns was mainly ductile. Local buckling was followed by the stress redistribution to the corner regions. Some columns failed more suddenly due to the corner fillet welds failure in the post-ultimate loading stage.
  - c) the failure of the beams was ductile. No significant strength reduction was observed. Two or three local buckling waves at the top flange of every beam developed. Top flange buckling was followed by web buckling.
3. Numerical models of the WO type columns with the  $B/200$  geometrical imperfection amplitude and residual stresses were created. Based on the numerical results of the column models:
  - a) it was found that the ultimate average stress of the  $b/t=40$  ratio panel was 33% higher than that of the  $b/t=80$  ratio panel. The ultimate average stresses of those panels were 83% and 63% of the steel yield strength, respectively.
  - b) the average normal stress of the more slender panels decreased more suddenly, while the more compact panels buckled very slowly and gradually.
  - c) the critical stresses were decreasing linearly with the increase of the  $b/t$  ratio in the  $b/t$  range between 40–80. The ultimate average stress decrease was negative exponential in the range between 40–60 and linear in the range between 60–80.
4. All the experimental beams and two additional numerical models were analysed via the finite element method. Based on the numerical beam results:
  - a) B3-1 ( $b/t=79.7$ ) and B4-1 ( $b/t=59.8$ ) beam models showed that the ultimate average stress of the compressed beam flanges was 24–35% higher for the beams with a low level of imperfections. The ultimate average stresses of those beams considering a high level of imperfections were 62% and 68% of the yield strength, respectively. However, at the strains higher than 0.01, a high level of imperfections had a minor effect on the stress-strain behaviour.
  - b) models with residual stresses and the  $B/200$  geometrical imperfection amplitude showed that the critical buckling stress of the 428.5 MPa yield

strength panel was higher than that of the 335.9 MPa yield strength panel by 26% and 15% for the panels with the  $b/t$  ratios equal to 60 and 80, respectively. The ultimate average stress of the 428.5 MPa yield strength panel was higher than that of the 335.9 MPa yield strength panel by 27% and 21% for the respective aforementioned panel  $b/t$  ratios.

- c) the maximum beam B3-1 top flange average normal stress was reached prior to reaching the ultimate bending moment. Once the ultimate bending moment had been reached, significant average stress reduction of the flange was observed.
5. An idealised average normal stress-strain model for the compressed flanges in steel-concrete structures was proposed identifying several characteristic ranges: the linear pre-buckling range, the reduced stiffness range between the critical buckling stress and the ultimate stress, the constant ultimate stress-range and the negative exponential descending branch. Different expressions were proposed for the calculation of the critical stress and the ultimate stress of columns and beams.
  6. The proposed average normal stress-strain model was adopted in the beam analysis via the iterative layer method. Full bending moment-deflection curves were obtained. The experimental ultimate bending moment values were higher than those obtained via the iterative layer method by 5–12%. Thus, it is likely that the confinement provided by the slender steel profile could increase the strength of concrete. However, this type of strength increase was not taken into account by the confined concrete model adopted for the iterative layer method.

## FUTURE DEVELOPMENTS

The local buckling behaviour was found to be an important factor for defining the ultimate strength of compressed steel panels. The strength of such panels was also found to be highly dependent on the level of the initial imperfections assumed for the analysis. While the strength of the columns is almost equal to the maximum strength contribution of the concrete core and the steel profile, the behaviour of the beams is more complicated, and it requires to use the iterative methods to obtain the exact structural response. The proposed average normal stress-strain model for compressed steel panels is suitable for such analysis.

On the other hand, the local buckling of steel webs was only significant at the very advanced loading stages, i.e., when the beams were already failing. Therefore, a separate stress-strain model was not proposed for this case. It was also observed that once the web buckles at a specific height of the profile, the loss of the concrete strength at the same height is evident. Thus, it is possible that the local buckling of the web would have more impact in the earlier loading stages for the beams with higher height-to-thickness ratios. Analysis of such slender webs could be the highlight of the future developments.

One of the main focus points in the current study was the structural behaviour of simply supported beams. In the future, the formulation of the finite layer method could also be adapted for the case of a continuous beam. In this case, the beams with non-symmetric flanges could be analysed, as the bottom flange of the composite beam could also be used as the support for the reinforced concrete slab.

Fin plate connections of such thin-walled steel-concrete structures also present additional considerations. As the flange of the column is susceptible to buckling, the rotational capacity of such a connection is expected to be very low. Theoretically, semi rigid connections might be economical when selecting the optimum cross-sections. However, the possibility and costs of producing such connections could be analysed in the future.

## SANTRAUKA

### Tyrimo aktualumas

Naudojant kompozitines plieno-betono konstrukcijas, išnaudojami tiek plieno, tiek betono konstrukcijų privalumai. Jos pasižymi didesniu standumu bei gaisrinio atsparumu, palyginus su plieninėmis konstrukcijomis, ir yra liaunesnės nei gelžbetoninės konstrukcijos. Uždaras plieninis profilis taip pat atlieka klojinio funkciją betonui. Taip sumažinamas konstrukcijų surinkimo laikas.

Stori lakštai, turintys mažą pločio ir storio santykį, projektuojami nesudėtingai, kadangi jie gali pasiekti gniuždomąją plastinę laikomąją galią. Kita vertus, kai kuriais atvejais plieninio profilio pločio ir storio santykis gali būti didelis, kadangi plonesni profiliai paprastai būna pigesni. Tokie profiliai yra jautrūs vietiniam klupumui. Tokiu atveju paprastai yra skaičiuojamas efektyvusis skerspjūvio plotas. Kita vertus, plieniniai lakštai betonu užpildytoje konstrukcijoje yra mažiau jautrūs vietiniam klupumui, kadangi betono šerdis suvaržo klupumą viena kryptimi.

Kai kurios plačiai pasaulyje naudojamos projektavimo normos, tokios kaip EN 1994-1-1, neturi atskirų projektavimo taisyklių ir išraiškų plienbetoninių skerspjūvių vietinio klupumo skaičiavimams. Dėl šios priežasties paprastų plieninių skerspjūvių projektavimo taisyklės ir išraiškos taip pat yra naudojamos ir plieniniams lakštams plienbetoninėse konstrukcijose. Tokiu atveju plieninio skerspjūvio atsparumas plienbetoninėje konstrukcijoje yra nepakankamai įvertinamas ir plieninis profilis yra parenkamas neekonomiškai.

Nors įvairūs mokslininkai yra atlikę plienbetoninių konstrukcijų vietinio klupumo tyrimus, supaprastinti projektavimo metodai buvo sukurti tik centriško ir ekscentriško gniuždymo atvejams. Atskiri metodai nebuvo sukurti lenkimo atvejui ir todėl nėra žinoma, kaip reikėtų įvertinti vietinį klupumą plienbetoninėse sijose.

Pagal jau sukurtus projektavimo metodus ir modelius paprastai yra skaičiuojami plieninio lakšto kritiniai klupumo įtempiai, susiję su vietinio klupumo pradžia, ir efektyvusis skerspjūvio plotas, susijęs su lakšto laikomąja galia. Kita vertus, tokiuose modeliuose tikslus efektyviojo skerspjūvio ploto arba vidutinių normalinių įtempių vystymasis paprastai nėra aprašomas. Tai reikalinga, kadangi lakšto stipris pradeda mažėti po to, kai jis pasiekia maksimalią laikomąją galią. Be to, tokius supaprastintus modelius yra sunku taikyti, naudojant iteracinius plienbetoninių konstrukcijų skaičiavimo metodus.

Taigi, tam, kad vietinio klupumo reiškinys tokiose konstrukcijose būtų suvokiamas pilnai, ir tam, kad plienbetoninės konstrukcijos būtų projektuojamos ekonomiškai, vidutinių normalinių įtempių būvio vystymosi, priklausomai nuo deformacijų, modelis su atitinkamomis analitinėmis išraiškomis turėtų būti pasiūlytas.



## **Tyrimų objektas**

Šiame darbe yra analizuojamos suvirintos plonasienės plieninės betonu užpildytos trumpos kolonos ir sijos. Pagrindinis šio tyrimo objektas yra vietinio klupumo reiškinyje tokiose konstrukcijose.

## **Darbo tikslas**

Disertacijos tyrimo tikslas sukurti plonasienių plieninių betonu užpildytų konstrukcijų gniuždomų plieno lakštų vidutinių normalinių įtempių-deformacijų modelį, įvertinant vietinio klupumo poveikį, ir panaudoti šį modelį, apskaičiuojant plonasienių plieninių betonu užpildytų sijų momentų-įlinkių priklausomybes.

## **Darbo uždaviniai**

1. Atlikti literatūros apžvalgą apie plonasienes plienines konstrukcijas ir daugiaašio gniuždymo veikiamo betono mechanines savybes.
2. Atlikti plonasienių plieninių betonu užpildytų trumpų kolonų gniuždymo ir sijų lenkimo eksperimentus.
3. Sukurti plonasienių plieninių betonu užpildytų trumpų kolonų ir sijų baigtinių elementų modelius ir gauti gniuždomų plieninių lakštų vidutinių normalinių įtempių-deformacijų kreives.
4. Sukurti vidutinių normalinių įtempių-deformacijų modelį gniuždomiems plieno lakštams betonu užpildytose plonasienėse plieninėse konstrukcijose.
5. Sluoksnių metodu gauti sijų lenkimo momentų-įlinkių kreives, panaudojant sukurtą vidutinių normalinių įtempių-deformacijų modelį.

## **Tyrimo metodai**

1. Eksperimentiniai kolonų gniuždymo ir sijų lenkimo tyrimai, panaudojant hidraulinį 500 tonų galios presą. Deformacijų jutikliai ir poslinkių matuokliai naudojami deformacijų ir įlinkių matavimui atitinkamai.
2. Teoriniai metodai kritinių įtempių, maksimalių įtempių ir efektyviojo pločio skaičiavimui. Iteracinis sluoksnių metodas sijų lenkimo momentų-įlinkių analizei.
3. Skaitinė analizė, naudojant baigtinių elementų programą „Abaqus“.

## **Mokslinis naujumas**

Remiantis gautais plonasienių plieninių betonu užpildytų konstrukcijų eksperimentiniais ir skaitinio modeliavimo rezultatais, pasiūlytas naujas analitinis modelis kolonų ir sijų gniuždomų plieno lakštų vidutinių normalinių įtempių būvio, priklausomai nuo gniuždymo deformacijų, skaičiavimui.

## **Praktinė tyrimo reikšmė**

Siūlomas analitinis modelis gniuždomų plieno lakštų plienbetoninėse kolonose ir sijose vidutinių normalinių įtempių būvio, priklausomai nuo gniuždymo deformacijų, skaičiavimui gali būti naudojamas iteraciniuose skaičiavimo metoduose tam, kad būtų gaunamos suvirintų plonasienių plieninių betonu užpildytų konstrukcijų ašinės jėgos-sutrumpėjimo arba lenkimo momentų-įlinkių kreivės. Siūlomos kritinių klupumo įtempių ir maksimalių įtempių skaičiavimo matematinės išraiškos taip pat

gali būti naudojamos supaprastintiems rankiniams kolonų kritinės klupumo jėgos ir laikomosios galios skaičiavimams. Tokiu būdu gali būti įvertinamas laikomosios galios sumažėjimas dėl vietinio klupumo.

### **Ginamieji teiginiai**

1. Siūlomas analitinis modelis gniuždomų plieno lakštų plienbetoninėse kolonose ir sijose vidutinių normalinių įtempių būvio, priklausomai nuo gniuždymo deformacijų, skaičiavimui yra tinkamas naudoti iteraciniuose skaičiavimo metoduose tam, kad būtų galima gauti ašinės jėgos-sutrumpėjimo arba lenkimo momentų-įlinkių kreives.
2. Kompozitinių konstrukcijų gniuždomi plieno lakštai, neturintys arba turintys mažus pradinius nuokrypius, pasižymi didesniais maksimaliais įtempiais, tačiau įtempių mažėjimas, lakštui jau pasiekus maksimalią laikomąją galią, yra staigesnis, o plieniniai lakštai, turintys žymius pradinius nuokrypius, pasižymi mažesniais maksimaliais įtempiais, tačiau įtempių mažėjimas, lakštui jau pasiekus maksimalią laikomąją galią, vyksta labai palaipsniui.

## **4. I. LITERATŪROS APŽVALGA**

### **1.1. Plienbetoninių konstrukcijų privalumai ir praktinis panaudojimas**

Poreikis projektuoti betonu užpildytas plienines konstrukcijas yra paremtas ribotais medžiagų ištekliais, poveikiu aplinkai ir technologine konkurencija, kuri lemia, kad yra reikalingos lengvos, pigios, aukštas charakteristikas turinčios konstrukcijos [50]. Tokios konstrukcijos statybos aikštelėje gali būti sparčiai sumontuotos, naudojant varžtus ir montažines virintines siūles. Plieninis profilis taip pat atlieka betono klojinio funkciją. Dėl šių priežasčių yra galima greita ir ekonomiška statyba. Nors plieninės plonasiinės betonu užpildytos kolonos yra projektuojamos rečiau, vietinį klupumą taip pat gali reikėti įvertinti tam tikrais ypatingais atvejais, pavyzdžiui, analizuojant betonu užpildytus plieninius polius, kurių sienelės storis, bėgant laikui, palaipsniui mažėja dėl korozijos [47].

Aplinkai kenksmingų padangų atliekų turinčių betonu užpildytų plieninių kolonų elgseną gniuždant analizavo Duarte ir kt. [21]. Šios atliekos padidino kolonų plastiškumą, tačiau buvo užfiksuotas nedidelis kolonų standumo ir laikomosios galios sumažėjimas. Tokių kolonų tvarumą analizavo Duarte ir kt. [19]. Atliekų turinčių ir įprastu betonu užpildytų plieninių kolonų suminė energija 50 metų laikotarpiu buvo 25 % didesnė nei gelžbetoninių kolonų.

Plienbetoninės konstrukcijos dėl skerspjūvio viduje esančios betono šerdies turi didesnę gaisrinį atsparumą už plienines. Tokių konstrukcijų gaisrinio projektavimo principai yra aprašyti Eurokode 4, 1–2 dalyje [30]. Remiantis šiais principais, Wang [90] pasiūlė supaprastintą tokio tipo kolonų gaisrinio projektavimo metodą.

### **1.2. Gniuždomo betono plienbetoninėse konstrukcijose elgsena**

Vienas iš plačiausiai naudojamų betono įtempių-deformacijų modelių yra pateiktas Eurokode 2 [26]. Kita vertus, daugiaašio gniuždymo veikiamo betono įtempių-deformacijų elgsena yra kitokia. Pagrindinius tokio reiškinio principus aprašė Johansson ir Akesson [41]. Vieni iš pirmųjų įtempių-deformacijų modelių betonui, veikiamam daugiaašio gniuždymo dėl skersinės armatūros, buvo pasiūlyti Kent ir Park [45], Mander ir kt. [58]. Dėl plieninio profilio slėgio daugiaašio gniuždymo veikiamo betono modelį pasiūlė Tomii ir Sakino [85]. Liang [49] savo tyrimuose panaudojo Mander ir kt. [58] modelio bei Tomii ir Sakino [85] modelio kombinaciją. Reikšmingus tyrimus apie daugiaašio gniuždymo veikiamą betoną plienbetoninėse kolonose atliko Schneider [76], Huang ir kt. [38]. Remiantis Huang ir kt. [38], šoninis slėgis, sukeltas kvadratinio plieninio skerspjūvio, turinčio pločio ir storio santykį, kuris yra didesnis nei 29,2, buvo santykinai mažas.

### **1.3. Geometriniai nuokrypiai**

Geometriniai nuokrypiai yra konstrukcijų gamybos, transportavimo ir surinkimo rezultatas, todėl jie gali turėti bet kokią formą. Analizei priimti geometriniai nuokrypiai turėtų atspindėti klupumui pavojingiausią atvejį. Liang ir Uy [48] naudojo klupumo formas, gautas tiesinės klupumo analizės metu, o Wright [93] pasiūlė naudoti idealizuotas nuokrypių formas. Nuokrypių amplitudės Liang ir Uy [48] tyrime buvo priimtos santykinai pagal analizuojamų lakštų storį, nustatant bazinę

reikšmę 0,1  $t$ . Kita vertus, Eurokode 3, 1–5 dalyje [28] geometrinių nuokrypių amplitudės yra priimtoms santykinės lakštų pločiui, nustatant bazinę reikšmę  $B/200$ .

#### 1.4. Liekamieji įtempiai

Žymūs liekamieji įtempiai plieniniuose lakštuose atsiranda suvirinimo metu. Jie gali būti išmatuoti, naudojant deformacijų jutiklius. Tokius matavimus atliko Uy [86]. Supaprastintus liekamųjų įtempių modelius pasiūlė Uy [87], Shi ir kt. [78], Young [97], Szalai ir Papp [84], Barth ir White [7], Bjorhovde ir kt. [10], Somodi ir Kövesdi [80]. Tokie modeliai gali būti tiesiogiai panaudoti baigtinių elementų (BE) analizės metu. Liekamuosius įtempius taip pat galima įvertinti, modifikuojant plieno įtempių-deformacijų kreivę. Tokias modifikacijas pasiūlė Song ir kt. [82], Ramberg ir Osgood [72].

#### 1.5. Vietinis klupumas plienbetoninėse konstrukcijose

Plieninių skerspjūvių, turinčių didelį pločio ir storio santykį  $b / t$ , lakštai gali prarasti pastovumą. Skerspjūvio plotas, nepaveiktas vietinio klupumo, yra vadinamas efektyviuoju skerspjūvio plotu. Skaiciavimo modelis, priimtas Eurokode 3, 1–5 dalyje [28] ir Eurokode 4 [29], yra paremtas būtent šiuo principu, tačiau jis neįvertina papildomų kraštinių sąlygų lakštui dėl konstrukcijoje esančio betono.

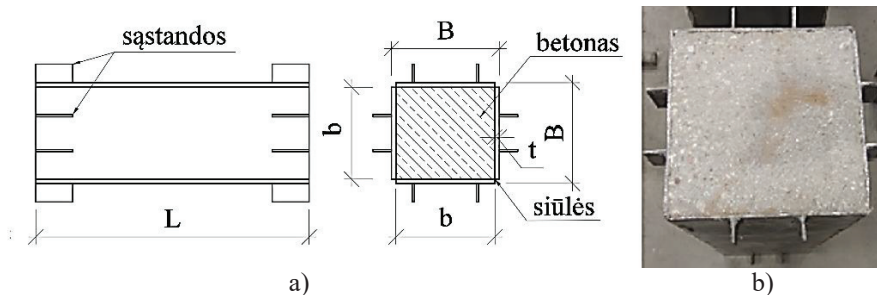
Vietinis klupumas plienbetoninėse konstrukcijose buvo tyrinėtas skirtingų mokslininkų. Reikšmingus kolonų ir sijų tyrimus atliko Uy [86–88]. Analitinę plieninių lakštų su pradiniais nuokrypiais plienbetoninėse konstrukcijose kritinių klupumo įtempių skaičiavimo išraišką pasiūlė Liang ir kt. [53]. Efektyviojo pločio išraiškas pasiūlė Bradford ir kt. [12], Liang ir Uy [48]. Maksimalių įtempių skaičiavimo formules pasiūlė Liang ir kt. [53], Ge ir Usami [34], Nakai ir kt. [66]. Liang [49] plienbetonines kolonas analizavo iteraciniu analitiniu metodu. Tarp kritinių klupumo įtempių ir maksimalių įtempių efektyvusis skerspjūvio plotas buvo interpoliuojamas tiesiškai. Kita vertus, remiantis Song ir kt. [82] tyrimu, galima teigti, kad efektyviojo pločio arba vidutinių įtempių vystymasis yra sudėtingesnis ir Liang [49] tyrime buvo neįvertintas efektyviojo ploto mažėjimas. Taigi, turėtų būti pasiūlytas modelis, skirtas gniuždomiems lakštams betonu užpildytose konstrukcijose ir įvertinantis vidutinių normalinių įtempių būvį, priklausomai nuo gniuždymo deformacijų.

## II. EKSPERIMENTINIAI PLONASIENIŲ PLIENBETONINIŲ KONSTRUKCIJŲ TYRIMAI

### 2.1. Eksperimentiniai betonu užpildytų plieninių kolonų tyrimai

#### 2.1.1. Kolonų bandinių paruošimas ir savybės

Šešiolika keturkampių kolonų, turinčių aštuonis skirtingus skerspjūvius, buvo suvirinta iš plonasienių plieninių lakštų. Kolonų schema ir vaizdas yra pateikti 1 pav. Siekiant įvertinti plieno-betono sukibimo įtaką, buvo pagaminta po du vienodus bandinius kiekvienam (išskyrus vieną) skerspjūvio tipui. Vienas iš dviejų vienodų bandinių turėjo normalias sukibimo sąlygas (WO tipas), o kitame bandinyje buvo įdėta polietileninė plėvelė (W tipas). Betonui į kolonas buvo pilamas po 2–3 kartus ir sutankinamas giluminiu betono vibratoriumi.



1 pav. a) kolonų schema, b) kolonos vaizdas

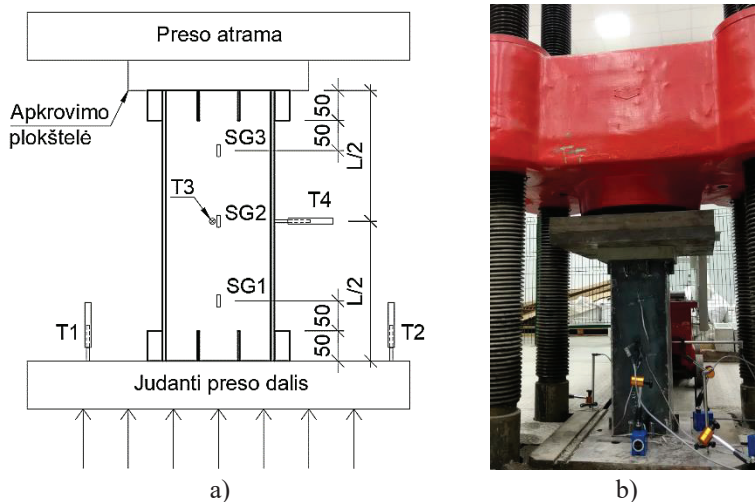
1 lentelė. Kolonų bandinių matmenys ir medžiagų savybės

Kolonos žymėjimas	Vidinis plotis $b$ , mm	Vidinis aukštis $h$ , mm	Storis $t$ , mm	$b/t$	$h/t$	Ilgis $L$ , mm	Vidutinis betono stipris $f_{c,avg}$ , MPa	Vidutinė takumo riba $f_{y,avg}$ , MPa
1-WO	238,4	178,8	3,12	76,4	57,3	719,3	29,97	370,85
1-W	238,5	178,7	3,05	78,2	58,6	718,5	31,82	370,85
2-WO	237,0	237,6	3,09	76,7	76,9	718,0	26,79	370,85
2-W	238,0	237,7	3,14	75,8	75,7	719,0	25,93	370,85
3-W	198,1	198,1	3,09	64,1	64,1	598,8	32,10	370,85
3.1-WO	198,4	198,4	3,02	65,7	65,7	599,5	32,10	370,85
3.2-WO	199,0	199,6	3,10	64,2	64,4	598,3	33,59	370,85
4-W	178,6	116,9	3,15	56,7	37,1	539,0	30,41	370,85
4-WO	178,3	119,0	3,10	57,5	38,4	537,3	33,59	370,85
5-W	217,4	157,2	3,07	70,8	51,2	659,3	35,13	370,85
5-WO	218,9	158,4	3,07	71,3	51,6	659,0	35,13	370,85
6-W	178,5	179,4	2,98	59,9	60,2	539,5	33,57	370,85
7-W	158,7	158,7	3,07	51,7	51,7	479,0	31,66	370,85
7-WO	158,6	159,2	3,08	51,5	51,7	479,0	31,66	370,85
8-W	138,7	138,7	3,09	44,9	44,9	419,0	31,66	370,85
8-WO	139,2	139,5	3,06	45,5	45,6	419,0	31,66	370,85

Siekiant nustatyti medžiagų stiprius, buvo išbandyti 100 x 100 x 100 mm betono kubeliai, 100 x 100 x 300 betono prizmės ir frezuoti plieno bandiniai. Kolonų bandinių matmenys ir medžiagų savybės pateiktos 1 lent.

### 2.1.2. Kolonų gniuždymo bandymo įranga ir eiga

Kolonų apkrovimui buvo naudojamas hidraulinis 500 tonų presas. Eksperimento schema ir vaizdas pateikti 2 pav. Trys deformacijų jutikliai (SG1–SG3) buvo priklijuoti ant kiekvienos kolonos vienos sienutės. Poslinkio matuokliai T1 ir T2 buvo panaudoti kolonos bazės poslinkiui matuoti, o poslinkio matuokliai T3 ir T4 buvo naudojami sienučių šoninio poslinkio matavimui. Priimtas 10 kN/s apkrovimo greitis.



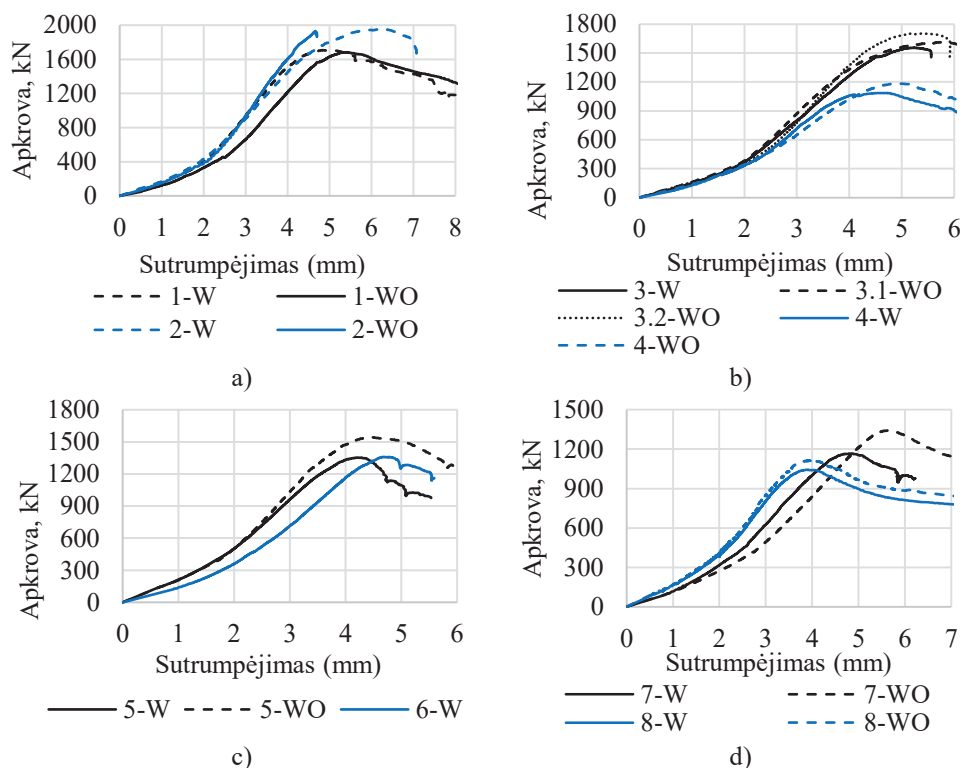
2 pav. a) kolonų eksperimento schema, b) kolonų eksperimento vaizdas

### 2.1.3. Plonasienių plienbetoninių kolonų eksperimento rezultatai

Kolonų vaizdai, įvykus klupumui pateikti 3 pav. Klupumas visais atvejais įvyko kolonos viduryje arba 4–6 cm nuo sąstandų. Kolonų apkrovos-sutrupėjimo kreivės pateiktos 4 pav. Eksperimentiškai gautas kolonų sutrupėjimas buvo didesnis negu prognozuota. Panašūs skirtumai taip pat buvo užfiksuoti Hu ir kt. [38], Duarte [20], Ellobody ir Young [22] tyrimuose. Remiantis Duarte [20] tyrimu, galimos to priežastys buvo tokios: tarpeliai tarp kontaktinių paviršių; pradiniai nuokrypiai; atsitiktinis apkrovos ekscentricitetas; mikroplyšiai dėl betono traukumo uždaramė profilyje. Betono paviršiaus išsikišimas virš plieno profilio gali lemti tai, kad betonas yra apkraunamas pirmiau, o pilnas kolonos standumas nebus pasiektas. Eksperimento metu nematuotas viršutinės preso dalies nuosėdis gali lemti didesnius kolonų sutrupėjimo rezultatus.



3 pav. Kolonų vaizdai, įvykus klupumui



4 pav. Kolonų apkrovos-sutrupėjimo kreivės: a) 1-W, 1-WO, 2-W ir 2-WO; b) 3-W, 3.1-WO, 3.2-WO, 4-W ir 4-WO; c) 5-W, 5-WO ir 6-W; d) 7-W, 7-WO, 8-W ir 8-WO

Kolonų eksperimento rezultatai pateikti 2 lent. Kritinių įtempių reikšmės buvo nustatytos pagal deformacijų daviklių rodmenis, papildomai remiantis apkrovos-sienutės poslinkio rezultatais. Daugeliu atvejų kritinių įtempių reikšmės skirtinguose kolonų aukščiuose buvo skirtingos. Galima to priežastis yra geometriniai nuokrypiai, dėl kurių klupimo bangos centras gali nesutapti su deformacijų daviklio vieta. Be to, deformacijos buvo matuojamos tik vienoje kiekvienos kolonos sienutėje, o dėl

atsitiktinio ekscentriciteto įtempiai skirtingose sienutėse gali vystytis netolygiai. Taigi, kritiniai įtempiai turėjo didelį išsibarstymą.

## 2 lentelė. Eksperimentiniai kolonų rezultatai

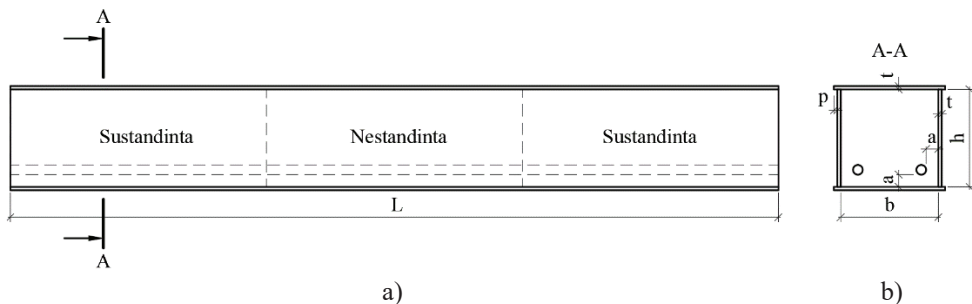
Kolonos žymėjimas	$b/t$	$h/t$	Eksp. kritinė jėga $N_{cr,ex}$ , kN	Eksp. laikomoji galia $N_{u,ex}$ , kN	Eksp. kritiniai įtempiai $\sigma_{cr,ex}$ , MPa	Eksp. maksimalūs įtempiai $f_{u,ex}$ , MPa	$\sigma_{cr,ex}/f_{y,avg}$	$f_{u,ex}/f_{y,avg}$ ( $A_{eff}/A_s$ )
1-W	78,2	58,6	1350,0	1706,6	157,5	242,3	0,42	0,65
1-WO	76,4	57,3	975,0	1682,6	149,1	253,9	0,40	0,68
2-W	75,8	75,7	1400,0	1957,0	165,9	263,1	0,45	0,71
2-WO	76,7	76,9	1750,0	1930,5	228,3	246,4	0,62	0,66
3-W	64,1	64,1	600,0	1554,9	127,1	223,5	0,34	0,60
3.1-WO	65,7	65,7	600,0	1612,1	130,0	251,7	0,35	0,68
3.2-WO	64,2	64,4	700,0	1701,9	204,8	256,5	0,55	0,69
4-W	56,7	37,1	900,0	1085,3	240,2	306,2	0,65	0,83
4-WO	57,5	38,4	800,0	1184,2	192,2	328,5	0,52	0,89
5-W	70,8	51,2	750,0	1352,7	154,4	168,1	0,42	0,45
5-WO	71,3	51,6	1300,0	1543,7	210,0	244,8	0,57	0,66
6-W	59,9	60,2	950,0	1358,4	85,3	233,7	0,23	0,63
7-W	51,7	51,7	1025,0	1167,2	204,8	268,1	0,55	0,72
7-WO	51,5	51,7	1100,0	1343,2	228,9	356,4	0,62	0,96
8-W	44,9	44,9	900,0	1043,4	263,3	320,1	0,71	0,86
8-WO	45,5	45,6	1000,0	1112,0	207,9	358,6	0,56	0,97

WO tipo kolonų santykis  $A_{eff}/A_s$  tarp efektyviojo skerspjūvio ploto ir viso skerspjūvio ploto dauguma atvejų buvo didesnis (iki 47 %) nei W tipo kolonų. Vienintelė W tipo kolona, turinti didesnę (9 %)  $A_{eff}/A_s$  santykį buvo 2-W. Taip galėjo nutikti dėl betono stiprio neapibrėžtumo arba skirtingų pradinių nuokrypių.

## 2.2. Eksperimentiniai betonu užpildytų plieninių sijų tyrimai

### 2.2.1. Sijų bandinių paruošimas ir savybės

Ketrios kvadratinės plieninės sijos buvo suvirintos iš plonasienių lakštų. Sijų schema pateikta 5 pav. Armavimui panaudota po du B500B klasės ( $E_{sr}=200$  GPa) 20 mm armatūros strypus. Betonas į sijas buvo pilamas po 2–3 kartus ir sutankinamas.



5 pav. Plienbetoninių sijų: a) vaizdas iš šono, b) pjūvis A-A



Sijų bandinių matmenys ir medžiagų savybės pateiktos 3 lent. Matmenų žymėjimai pateikti 6 pav.

**3 lentelė.** Sijų bandinių matmenys ir medžiagų savybės

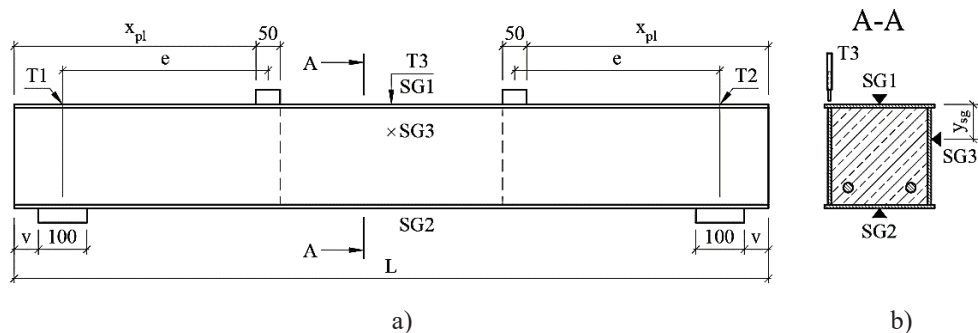
Sijos žymėjimas	$b$ , mm	$h$ , mm	$t$ , mm	$b/t$	$h/t$	$L$ , mm	$p$ , mm	$a$ , mm	$f_{c,avg}$ , MPa	$f_{y,avg}$ , MPa
B-1	236,0	240,0	4,02	58,7	59,7	2110,0	8,0	20,0	34,43	428,52
B-2	200,0	200,0	3,01	66,4	66,4	1750,0	7,0	20,0	39,83	335,86
B-3	240,0	240,0	3,01	79,7	79,7	2110,0	7,0	20,0	38,43	335,86
B-4	180,0	240,0	3,01	59,8	79,7	2110,0	7,0	20,0	35,75	335,86

## 2.2.2. Sijų lenkimo bandymo įranga ir eiga

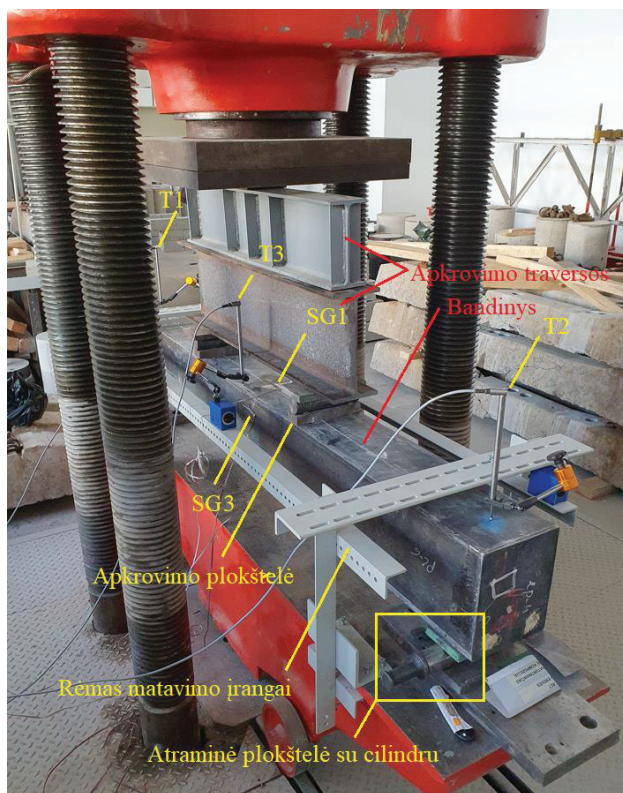
Sijų apkrovimui panaudotas hidraulinis 500 tonų presas. Įlinkių ir nuosėdžių matavimui panaudoti trys poslinkių matuokliai (T1, T2, T3). Deformacijų matavimui panaudoti deformacijų jutikliai (SG1, SG2, SG3). Eksperimento matmenys nurodyti 4 lent. Eksperimento schema pateikta 6 pav., o eksperimento vaizdas – 7 pav. Apkrovimas atliktas 10 kN/s greičiu.

**4 lentelė.** Sijų eksperimento matmenys

Sijų žymėjimas	$L$ , mm	$v$ , mm	$x_{pl}$ , mm	$e$ , mm	$y_{sg}$ , mm
B1	2110,0	25	695	645	70
B2	1750,0	25	575	525	65
B3	2110,0	25	695	645	60
B4	2110,0	25	695	645	60



**6 pav.** Sijų lenkimo eksperimento: a) schema, b) pjūvis A-A



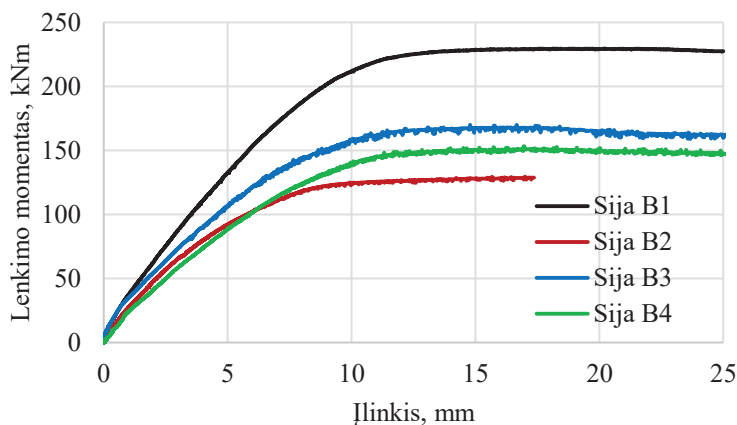
7 pav. Sijų lenkimo eksperimento vaizdas

### 2.2.3. Plonasienių plienbetoninių sijų eksperimento rezultatai

Sijų vaizdai po klupumo pateikti 8 pav. Viršutinėje juostoje visais atvejais susiformavo kelios klupumo bangos, o tuomet prasidėdavo sienutės klupumas. Sijų lenkimo momento-įlinkio kreivės pateiktos 9 pav. Suirimas buvo labai plastiškas. Žymus laikomosios galios mažėjimas neužfiksuotas.



8 pav. Sijų vaizdas po klupumo



9 pav. Sijų lenkimo momento-įlinkio kreivės

### III. TEORINIAI PLONASIENIŲ KOMPOZITINIŲ PLIENBETONINIŲ KONSTRUKCIJŲ TYRIMAI

#### 3.1. Plonasienių plienbetoninių kolonų skaičiavimo metodai

##### 3.1.1. Skaičiavimo metodai ir pagrindinės išraiškos

Plieno lakštų su pradiniais nuokrypiais kritiniai įtempiai buvo skaičiuojami pagal Liang ir kt. [53] išraišką. Liang ir Uy [48], Bradford ir kt. [12] išraiškos buvo naudojamos efektyviojo pločio skaičiavimui. Liang ir kt. [53], Ge ir Usami [34], Nakai ir kt. [66] formulės panaudotos lakštų maksimalių įtempių skaičiavimui. Kolonų kritinės jėgos  $N_{cr}$  buvo apskaičiuojamos pagal kritinius plieno lakšto įtempius, gautus pagal Liang ir kt. [53] išraišką, ir betono įtempius, atitinkančius santykinę deformaciją, kuriai esant pasiekiami kritiniai plieno lakšto įtempiai. Betono įtempiai buvo apskaičiuojami pagal Eurokodo 2 [26] netiesinį įtempių-deformacijų modelį. Kolonų teorinės laikomosios galios  $N_u$  buvo nustatytos, apskaičiuojant betono stiprį ir plieninio profilio laikomąją galią, nustatytą susumavus atskirų lakštų laikomąsias galias. Lakštų laikomosios galios buvo nustatytos, remiantis Liang ir kt. [53], Ge ir Usami [34], Nakai ir kt. [66] išraiškomis.

##### 3.1.2. Plonasienių plienbetoninių kolonų teorinių skaičiavimo metodų palyginimas

Plienbetoninių kolonų eksperimentinių tyrimų ir teorinių skaičiavimų rezultatai pateikti 5 lent. Eksperimentiniai rezultatai pažymėti indeksu „ex“, o teorinių skaičiavimų rezultatai pažymėti indeksais, atitinkančiais skirtingų autorių metodus.

## 5 lentelė. Kolonų eksperimentinių tyrimų ir teorinių skaičiavimų rezultatai

Kolonos žyma	$N_{cr,ex}$ kN	$N_{u,ex}$ kN	$N_{cr,Liang}$ kN	$N_{u,Liang,Uy}$ kN	$N_{u,Liang}$ kN	$N_{u,Br}$ kN	$N_{u,Ge}$ kN	$N_{u,Nakai}$ kN
1-W	1350,0	1706,6	1136,1	1730,7	1762,2	1700,7	1714,9	1759,4
1-WO	975,0	1682,6	1132,9	1684,4	1718,5	1660,9	1672,7	1715,0
2-W	1400,0	1957,0	1350,6	1868,4	1916,8	1818,8	1849,2	1912,7
2-WO	1750,0	1930,5	1344,4	1886,4	1933,1	1835,1	1866,2	1930,8
3-W	600,0	1554,9	1236,0	1681,7	1688,4	1634,7	1643,4	1677,0
3.1-WO	600,0	1612,1	1209,9	1663,2	1665,8	1607,9	1619,2	1654,5
3.2-WO	700,0	1701,9	1273,6	1747,3	1753,5	1698,6	1707,8	1742,0
4-W	900,0	1085,3	793,3	1065,6	1084,2	1166,0	1109,6	1113,9
4-WO	800,0	1184,2	827,9	1120,6	1139,2	1208,0	1163,1	1164,6
5-W	750,0	1352,7	1087,0	1576,9	1612,9	1586,9	1584,9	1612,8
5-WO	1300,0	1543,7	1090,4	1587,9	1623,8	1595,5	1594,6	1623,4
6-W	950,0	1358,4	1096,8	1458,9	1473,4	1443,0	1442,5	1465,9
7-W	1025,0	1167,2	936,7	1214,3	1239,5	1262,8	1239,4	1247,8
7-WO	1100,0	1343,2	938,3	1216,5	1241,9	1266,7	1242,5	1250,7
8-W	900,0	1043,4	788,6	1011,0	1035,5	1119,8	1070,6	1065,6
8-WO	1000,0	1112,0	788,5	1011,6	1036,1	1112,4	1066,9	1063,3

Vidutinės eksperimentinių tyrimų ir teorinių skaičiavimų rezultatų santykių reikšmės pateiktos 6 lent. Vertinant vidutinius WO tipo kolonų  $N_{u,ex}/N_u$  santykius, teorinės laikomosios galios reikšmės buvo iki 2 % mažesnės už eksperimentines, o W tipo kolonų – iki 5 % didesnės. Atskirų bandinių teorinių skaičiavimų reikšmės tam tikrais atvejais buvo iki 10 % mažesnės, o kitais atvejais – iki 14 % didesnės. Kita vertus, remiantis vidutinėmis reikšmėmis, galima teigti, kad prastas sukibimas turi neigiamos įtakos kolonos stipriui. Kolonai pasiekus laikomąją galią, vidurinė lakšto dalis atsiskiria nuo betono, tačiau kolonos kampuose sukibimas išlieka. Tai gali nulemti, kad kolona, turinti įprastą sukibimą, turi didesnę efektyvųjį plieninio skerspjūvio plotą. Vertinant vidutinius visų kolonų  $N_{u,ex}/N_u$  santykius, geriausias eksperimentinių ir teorinių rezultatų sutapimas buvo gautas, skaičiuojant pagal Liang ir Uy [48] metodiką. Remiantis ja, buvo gautas mažiausias laikomosios galios pervertinimas W tipo kolonomis ir išlaikoma nedidelė atsarga WO tipo kolonomis.

**6 lentelė.** Kolonų eksperimentinių tyrimų ir teorinių skaičiavimų rezultatų santykių vidurkiai

Kolonų tipas	$N_{cr,ex}/N_{cr,Liang}$	$N_{u,ex}/N_{u,Liang,Uy}$	$N_{u,ex}/N_{u,Liang}$	$N_{u,ex}/N_{u,Br}$	$N_{u,ex}/N_{u,Ge}$	$N_{u,ex}/N_{u,Nakai}$
W	0,95	0,97	0,95	0,95	0,96	0,95
WO	0,98	1,02	1,01	1,01	1,02	1,00
Visi	0,97	1,00	0,98	0,98	0,99	0,97

## 3.2. Skaitinis plonasienių plienbetoninių konstrukcijų modeliavimas

### 3.2.1. Skaitinių plonasienių plienbetoninių konstrukcijų modelių parametrai

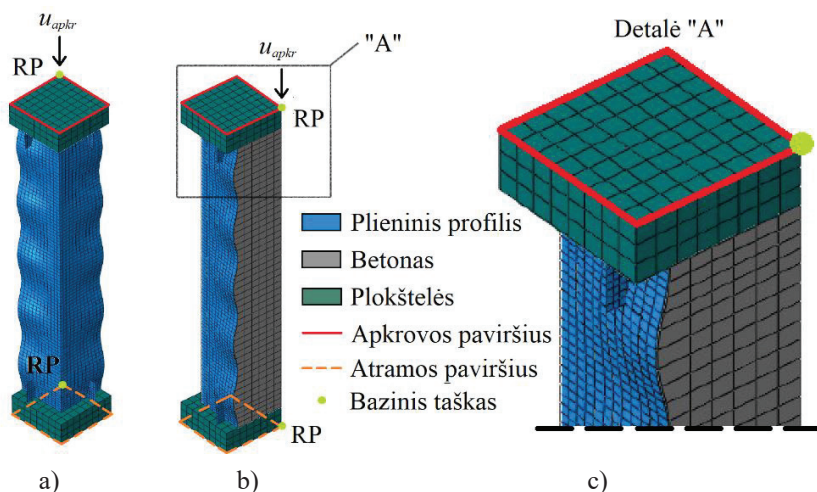
Kolonų ir sijų modeliai buvo sudaryti baigtinių elementų (BE) programa „Abaqus“. Lakštiniam plienui panaudoti dvimačiai keturių mazgų sumažintos

integracijos plokštieji elementai S4R, betonui ir plokštelėms – trimačiai aštuonių mazgų sumažintos integracijos elementai C3D8R, armatūrai – dviejų mazgų strypiniai elementai T3D2.

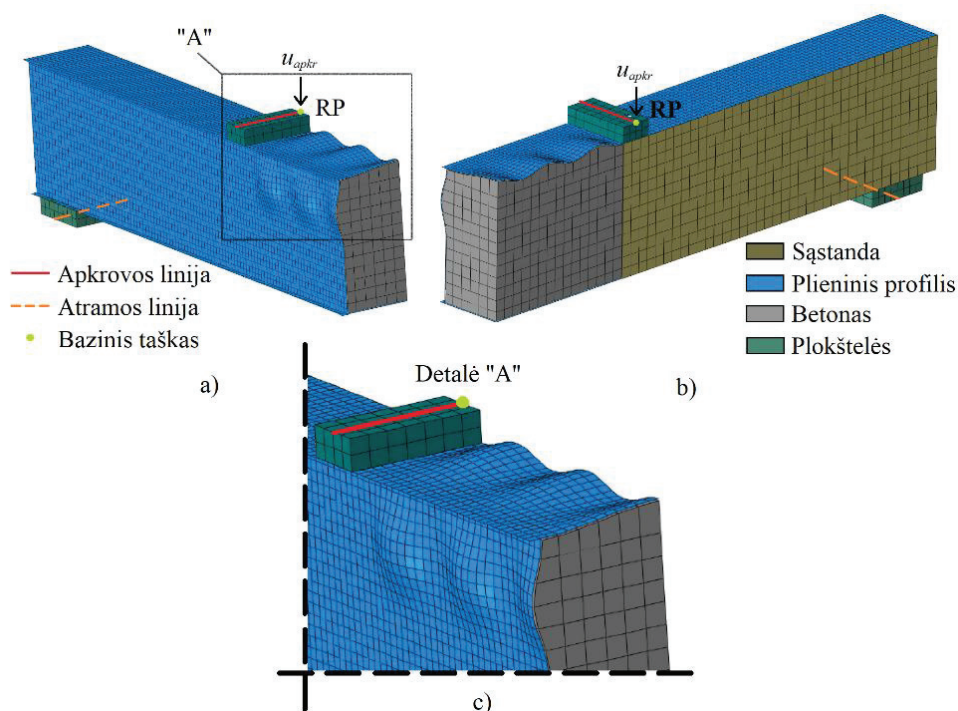
Kolono plieninio profilio baigtinių elementų tinklelio dydis buvo priimtas lygus  $B/24$ ,  $H/24$  ir  $L/100$  išilgai kolonos skerspjūvio pločio, kolonos skerspjūvio aukščio ir kolonos ilgio atitinkamai. Kolonos betono tinklelio dydis buvo dvigubai didesnis. Šie dydžiai priimti, remiantis Duarte ir kt. [21] tyrimu, ir patvirtinti bandomaisiais baigtinių elementų skaičiavimais.

Geometriniai nuokrypiai gniuždomose lakštų dalyse įvertinti, panaudojant Wright [93] išraišką. Liekamieji įtempiai įvertinti, modifikuojant plieno įtempių-deformacijų kreivę pagal Song ir kt. [82]. Gniuždomam betonui panaudotas netiesinis Eurokodo 2 [26] modelis, o „Abaqus“ programoje pritaikytas plastiškojo irimo (angl. *concrete damaged plasticity*, CDP) modelis. Armatūrai priimta bilinijinė elastoplastinė įtempių-deformacijų priklausomybė. Tempiamo betono elgsena aprašyta pagal suirimo energiją.

Plieno ir betono kontaktui aprašyti panaudotas trinties koeficientas 0,57 pagal Rabbat ir Russell [70]. Apkrova perduodama per plokšteles, nustatant joms tam tikrą poslinkį. Kolonos modelio vaizdai ir detalė pateikta 10 pav., o sijos – 11 pav.



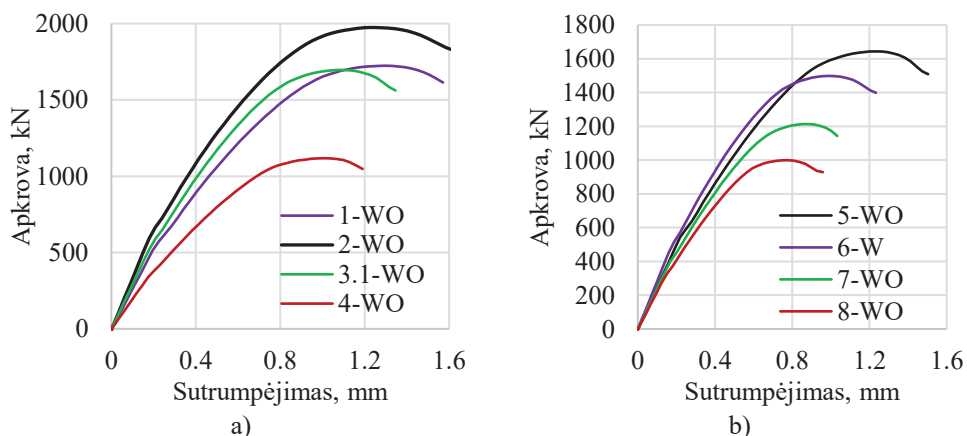
**10 pav.** Kolonos modelio: a) izometrinis kampinis vaizdas, b) izometrinis vaizdas į bandinio simetrijos plokštumą, c) detalė „A“



11 pav. Sijos modelio: a) izometrinis vaizdas iš kairės, b) izometrinis vaizdas iš dešinės, c) detalė „A“

### 3.2.2. Skaitinė plonasienių plienbetoninių kolonų analizė

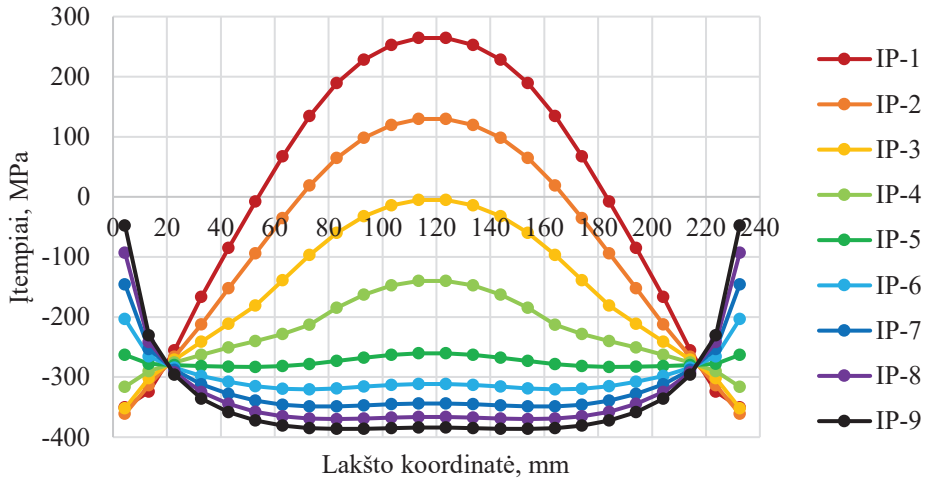
Visų WO tipo kolonų (išskyrus koloną 3.2-WO) ir kolonos 6-W modeliai su geometriniais nuokrypiais (amplitudė  $B/200$ ) buvo sumodeliuoti ir išanalizuoti BE metodu. Ašinės jėgos-sutrumpėjimo kreivės, gautos skaitinės analizės metu, pateiktos 12 pav.



12 pav. Skaitinės kolonų apkrovas-sutrumpėjimo kreivės: a) 1-WO, 2-WO, 3.1-WO ir 4-WO; b) 5-WO, 6-W, 7-WO ir 8-WO

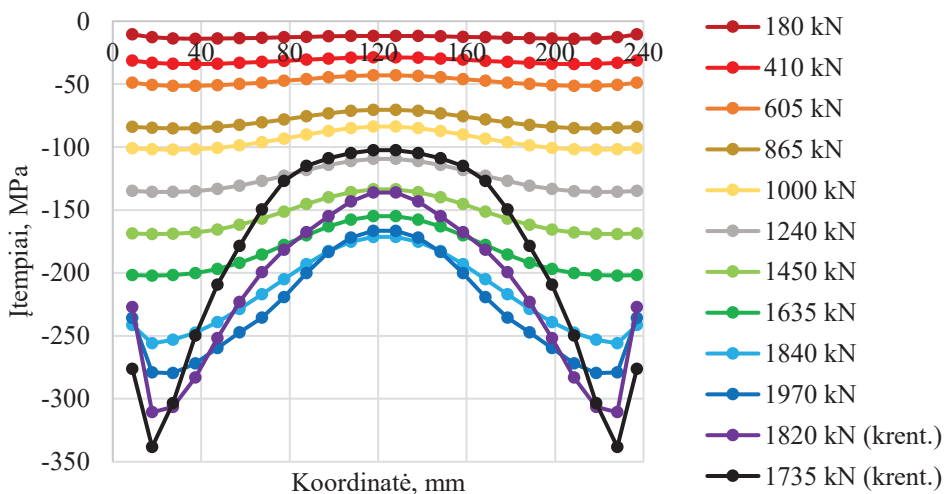


Lakštų normalinių įtempių vystymasis, priėmus devynis integravimo taškus (IP) per lakštų storį, buvo išanalizuotas BE metodu. Kolonos 2-WO lakšto įtempių pasiskirstymas, bandiniui pasiekus laikomąją galią, pateiktas 13 pav. Matomas klumpumas, kadangi lakšto viduryje yra lenkiamas.



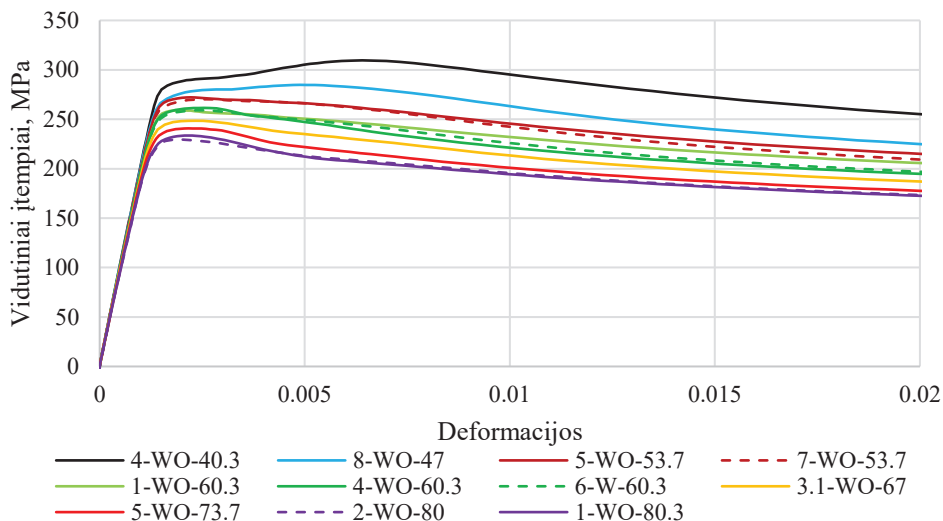
**13 pav.** Kolonos 2-WO plieninio lakšto normalinių pasiskirstymas, kolonai pasiekus maksimalią laikomąją galią

Kiekviename kiekvieno plieno lakšto baigtiniame elemente buvo gauti vidutiniai įtempiai. Tokiu būdu buvo gaunami vidutinių lakšto įtempių pasiskirstymai kiekviename apkrovimo žingsnyje. Tokie kolonos 2-WO lakšto normalinių įtempių pasiskirstymo ir vystymosi rezultatai pateikti 14 pav. Didinant apkrovą, įtempiai pasiskirsto vis netolygiau. Kadangi lakštas klumpa, įtempiai palaipsniui koncentruojasi kraštuose.



**14 pav.** Kolonos 2-WO plieninio lakšto normalinių įtempių vystymasis

Vidutiniai kiekvieno lakšto kiekvieno baigtinio elemento įtempiai buvo perskaičiuojami į vidutines įtempių reikšmes visame lakšte. Tokios kolonų lakštų vidutinių normalinių įtempių-deformacijų kreivės pateiktos 15 pav., o jų forma priklauso nuo  $b/t$  santykio ir plieno takumo ribos.



**15 pav.** Kolonų lakštų vidutinių normalinių įtempių-deformacijų kreivės

Norint išplėsti tyrimo rezultatų pritaikymo ribas, kolonos 2-WO, 4-WO, 5-WO ir 8-WO taip pat buvo sumodeliuotos ir išanalizuotos, priimant 335,9 MPa ir 428,5 MPa plieno takumo ribas, kadangi šios takumo ribų reikšmės buvo gautos eksperimentinių sijų tyrimų metu. Šioms papildomoms kolonomis buvo priimtos eksperimentiškai ištirtų kolonų betono savybės. Šių kolonų rezultatai panaudojami tolesniuose skyriuose, kuriant naują vidutinių normalinių įtempių-deformacijų modelį gniuždomiems plonasieniams plieniniams lakštams kompozitinėse konstrukcijose.

### 3.2.3. Skaitinė plonasienių plienbetoninių sijų analizė

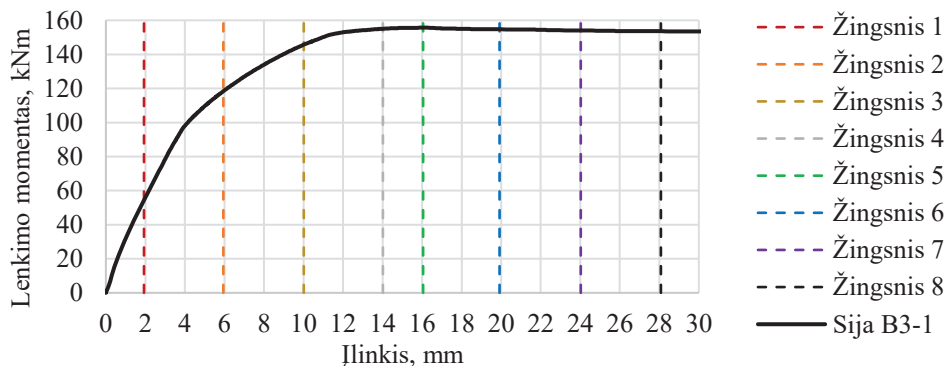
Šiame skyriuje BE metodu metodu buvo išanalizuotos eksperimentinės plienbetoninės sijos. Papildomai sukurti 428,5 MPa takumo ribos sijų B-5 ir B-6 modeliai. Visų šių sijų modelių parametrai pateikti 7 lent. Čia  $E_{c,avg}$  yra vidutinis betono tamprumo modulis.

**7 lentelė.** Sijų modelių matmenys ir medžiagų savybės

Sijos žymėjimas	$b$ , mm	$h$ , mm	$t$ , mm	$L$ , mm	$p$ , mm	$a$ , mm	$v$ , mm	$e$ , mm	$f_{c,avg}$ , MPa	$f_{y,avg}$ , MPa	$E_{c,avg}$ , MPa
B-1	236	240	4	2110	8	20	25	645	34,43	428,5	33,25
B-2	200	200	3	1750	7	20	25	525	39,83	335,9	35,31
B-3	240	240	3	2110	7	20	25	645	38,43	335,9	35,14
B-4	180	240	3	2110	7	20	25	645	35,75	335,9	32,90
B-5	320	320	4	2950	8	20	0	950	34,43	428,5	33,25
B-6	280	280	4	2950	8	20	0	950	34,43	428,5	33,25

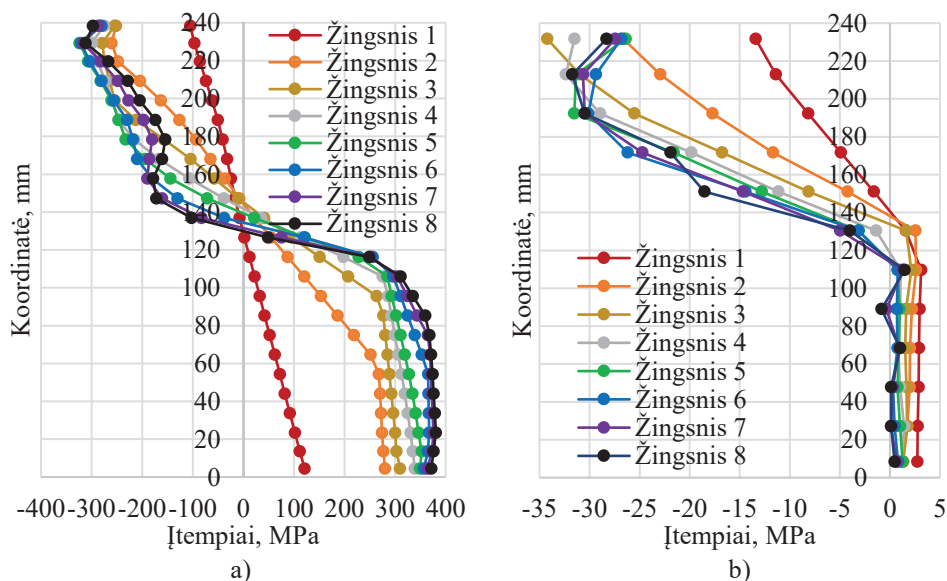


BE metodu gauta sijos B3-1 (su liekamaisiais įtempiais ir  $B/200$  amplitudės geometriniais nuokrypiais) lenkimo momento-įlinkio kreivė pateikta 16 pav. Apkrovimo žingsnyje Nr. 2 gautas maksimalus gniuždomos juostos  $b_{eff}/b$  santykis, o žingsnyje Nr. 5 pasiektas maksimalus lenkimo momentas.



16 pav. Sijos B3-1 lenkimo momento-įlinkio kreivė

Sijos B3-1 sienelės ir betono šerdies normalinių įtempių vystymasis pateiktas 17 pav. Įtempių sumažėjimas sienelėje dėl vietinio klupumo labiau matomas tik nuo 7 žingsnio, sijoms jau pradėjus irti. Nuo šio žingsnio betono šerdyje tame pačiame aukštyje, kuriame prasideda sienelės klupimas, taip pat yra matomas nežymus įtempių sumažėjimas. To priežastis yra tai, jog išklupus sienelei, betonas, esantis šioje zonoje, netenka atramos ir yra neveikiamas daugiaašio gniuždymo. Įtempių vystymasis gniuždomoje sijos juostoje yra analogiškas įtempių vystymuisi gniuždomos kolonos lakštuose. Kita vertus, dėl lenkiamos sijos kreivio, gniuždomos sijos juosta yra vertinama kaip atskiras atvejis.



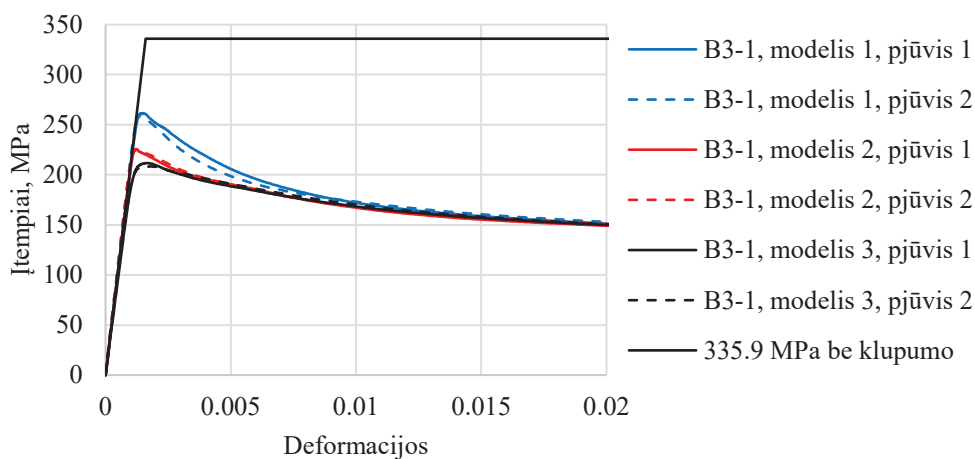
17 pav. Sijos B3-1 normalinių įtempių vystymasis: a) sienelėje, b) betono šerdyje

Pagrindinių sijos B3-1 parametrų reikšmės skirtinguose apkrovimo žingsniuose pateiktos 8 lent. Maksimalus gniuždomos juostos efektyviojo ploto santykis pasiektas 2 žingsnyje, lenkimo momentui sudarant tik 76 % maksimalios reikšmės. Armatūros ir gniuždomo betono įtempiai sudarė 54 % ir 71 % maksimalių reikšmių. Tolesniuose žingsniuose efektyvusis gniuždomos juostos plotis mažėjo ir sudarė 84 % maksimalios reikšmės, sijai pasiekus maksimalų lenkimo momentą.

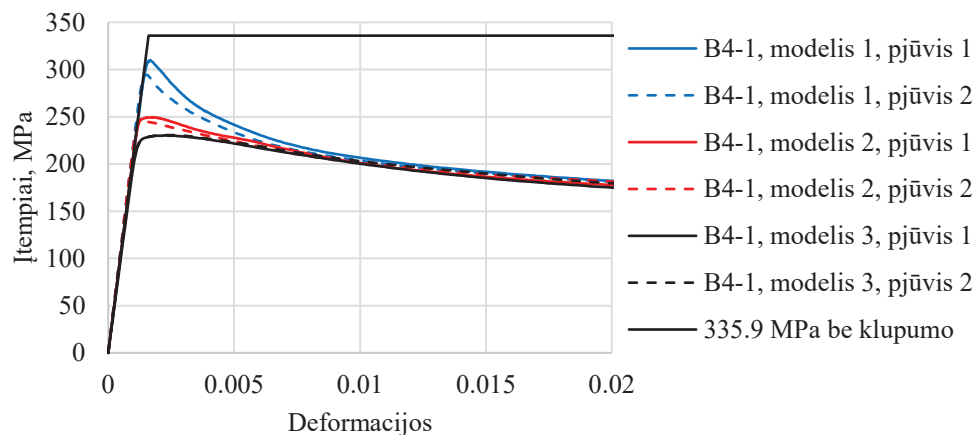
**8 lentelė.** B3-1 sijos parametrų vystymasis

Žingsnis	Pastabos	Lenkimo momentas, kNm	Juostos $b_{eff}/b$	Armatūros įtempiai, MPa	Vid. betono įtempiai, MPa
1	-	54,8	0,303	102,7	7,7
2	Maks. $b_{eff}/b$	119,3	0,630	308,7	16,2
3	-	146,8	0,589	506,0	22,7
4	-	156,3	0,556	568,9	20,5
5	Maks. momentas	156,8	0,528	572,6	21,0
6	-	156,4	0,470	573,6	21,5
7	-	156,1	0,438	575,7	18,8
8	-	156,1	0,418	576,2	19,1

Norint įvertinti pradinių nuokrypių įtaką gniuždomiems lakštams, sukurta po tris skaitinius modelius sijoms B3-1 ir B4-1. Pirmajame modelyje liekamieji įtempiai buvo neįvertinti, o geometriniams nuokrypiams priskirta  $B/500$  amplitudė. Antrajame modelyje papildomai įvertinti liekamieji įtempiai. Trečiajame modelyje geometrinių nuokrypių amplitudė padidinta iki  $B/200$ , įvertinant ir liekamuosius įtempius. Šių sijų vidutinių normalinių įtempių-deformacijų kreivės pateiktos 18 pav. ir 19 pav. atitinkamai. Kiekvienas modelis buvo analizuojamas dviejuose kritiniuose skerspjuvniuose: sijos viduryje (1 pjūvis) ir klupumo bangos, esančios šalia apkrovimo plokštelės, viduryje (2 pjūvis). Maksimalūs sijos B3-1 gniuždomos juostos ( $b/t=79,7$ ) vidutiniai normaliniai įtempiai pirmo, antro ir trečio tipo modeliuose sudarė 77 %, 67 % ir 62 % plieno takumo ribos atitinkamai. Analogiškai sijos B4-1 gniuždomos juostos ( $b/t=59,8$ ) įtempiai sudarė 92 %, 73 % ir 68 % plieno takumo ribos. Lyginant pirmojo, antrojo ir trečiojo modelio rezultatus, maksimalūs sijos B4-1 gniuždomos juostos vidutiniai normaliniai įtempiai buvo didesni už sijos B3-1 gniuždomos juostos įtempius 19 %, 9 % ir 9,5 % atitinkamai. Klupumas staigiau vyko modeliuose su mažesniais nuokrypiais, tačiau pasiekus 0,01–0,02 deformacijas, įtempių-deformacijų skirtumai buvo nežymūs.

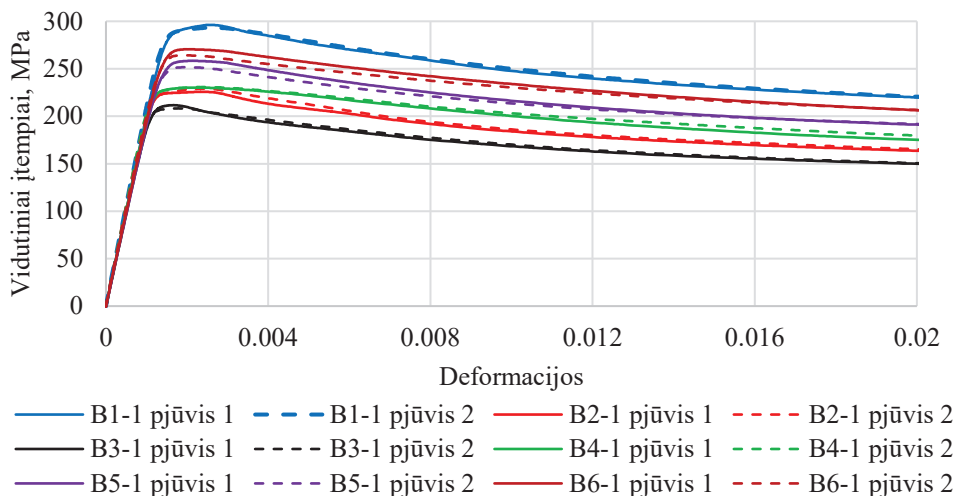


**18 pav.** Sijos B3-1 viršutinės juostos vidutinių normalinių įtempių-deformacijų kreivės



**19 pav.** Sijos B4-1 viršutinės juostos vidutinių normalinių įtempių-deformacijų kreivės

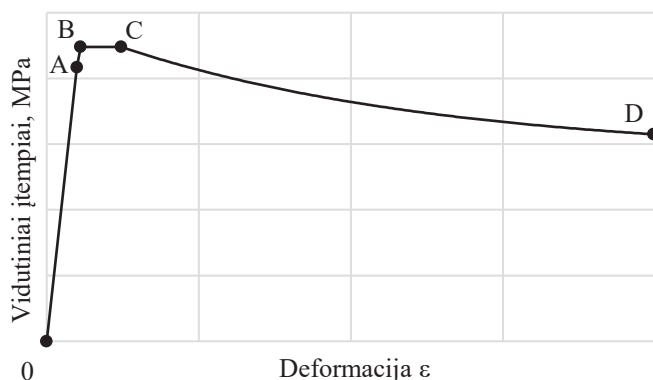
Visos šešios sijos buvo išanalizuotos pagal trečiąjį modelio tipą. Gniuždomos juostos vidutinių normalinių įtempių-deformacijų kreivės buvo gautos dviejuose sijų pjūviuose ir pateiktos 20 pav.



20 pav. Sijų gniuždomų juostų vidutinių normalinių įtempių-deformacijų kreivės

### 3.3. Siūlomas vidutinių normalinių įtempių-deformacijų modelis gniuždomiems plieno lakštams betonu užpildytose plonasienėse plieninėse konstrukcijose

Remiantis eksperimentiniais ir skaitinės analizės rezultatais, idealizuotas vidutinių normalinių įtempių-deformacijų modelis yra siūlomas ir pateikiamas 21 pav. Ruože 0–A įtempių-deformacijų priklausomybė yra tiesinė iki kritinių klupumo įtempių. Ruože A–B tarp kritinių ir maksimalių įtempių priimamas standumas lygus  $0,6E_s$ . Ruože B–C įtempiai yra pastovūs, o ruože C–D įtempiai eksponentiškai mažėja.



21 pav. Siūlomas plieninių lakštų vidutinių normalinių įtempių-deformacijų modelis

Remiantis BE analizės rezultatais, plieninių lakštų kompozitinėse kolonose kritiniai įtempiai apskaičiuojami pagal siūlomą išraišką (1), tinkamą lakštams, kurių takumo riba yra 335–430 MPa, o  $b/t$  santykis 40–81.

$$\sigma_{cr,c} = a_{cr,c} \left( \frac{b}{t} \right) + c_{cr,c}, \quad (1)$$

čia:  $a_{cr,c}$  yra koeficientas, apskaičiuojamas iš (2) išraiškos;  $c_{cr,c}$  yra y sankirtos taškas, apskaičiuojamas iš (3) išraiškos.

$$a_{cr,c} = -1.9 + 0.6 \cdot e^{-0.018(f_y - 335)}, \quad (2)$$

$$c_{cr,c} = 0.87 \cdot f_y + 13. \quad (3)$$

Kolonų lakštų, atitinkančių sąlygą  $40 \leq b/t \leq 60$ , maksimalių įtempių apskaičiavimui siūloma išraiška (4).

$$\sigma_{u,c} = a_{u,c} \cdot e^{-0.055\left(\frac{b}{t} - 40\right)} + c_{u,c}, \quad (4)$$

čia:  $a_{u,c}$ , yra koeficientas, apskaičiuojamas iš (5) išraiškos;  $c_{u,c}$  yra parametras, apskaičiuojamas iš (6) išraiškos.

$$a_{u,c} = 0.11 \cdot f_y + 33, \quad (5)$$

$$c_{u,c} = 0.51 \cdot f_y + 46. \quad (6)$$

$60 < b/t \leq 81$  ribose maksimalūs įtempiai apskaičiuojami pagal (7) išraišką:

$$\sigma_{u,c} = a_{u,c,l} \left( \frac{b}{t} \right) + c_{u,c,l}, \quad (7)$$

čia:  $a_{u,c,l}$ , yra koeficientas, apskaičiuojamas iš (8) išraiškos;  $c_{u,c,l}$  yra y sankirtos taškas, apskaičiuojamas iš (9) išraiškos.

$$a_{u,c,l} = -0.0027 \cdot f_y - 0.55, \quad (8)$$

$$c_{u,c,l} = 0.72 \cdot f_y + 86. \quad (9)$$

Apskaičiuota maksimalių įtempių reikšmė  $\sigma_{u,c}$  turi būti sumažinta, dauginant ją iš koeficiento  $k_{red}$ . Gauta įtempių reikšmė išlieka pastovi ruože  $\varepsilon_{u,1} < \varepsilon \leq \varepsilon_{u,2}$ . Deformacijos  $\varepsilon_{u,1}$  ir  $\varepsilon_{u,2}$  atitinka taškus B ir C siūlomame modelyje. Mažinimo koeficientas  $k_{red}$  ir sumažinti maksimalūs įtempiai, apskaičiuojami pagal išraiškas (10) ir (11).

$$k_{red} = \begin{cases} 0.975 & \text{for } 40 \leq \frac{b}{t} \leq 51 \\ -0.00035 \left( \frac{b}{t} \right) + 0.988 & \text{for } 51 < \frac{b}{t} \leq 81 \end{cases}, \quad (10)$$

$$\sigma_{u,c,red} = \sigma_{u,c} \cdot k_{red}. \quad (11)$$

Žinant kritinių ir maksimalių įtempių reikšmes, deformacija  $\varepsilon_{u,1}$  gali būti apskaičiuota. Deformacija  $\varepsilon_{u,2}$  apskaičiuojama pagal (12) išraišką.

$$\varepsilon_{u,2} = \varepsilon_{u,1} \cdot k_s, \quad (12)$$

čia:  $k_s$  yra deformacijų santykis pagal (13) išraišką, lakštams, kurie atitinka sąlygą  $40 \leq b/t < 81$ .

$$k_s = \begin{cases} -0.005 \left( 60 - \frac{b}{t} \right)^2 + 0.225 \left( 60 - \frac{b}{t} \right) + 2.34 & \text{for } 40 \leq \frac{b}{t} < 60 \\ -0.007 \left( \frac{b}{t} \right) + 2.76 & \text{for } 60 \leq \frac{b}{t} \leq 81 \end{cases}. \quad (13)$$

Deformacijoms viršijus  $\varepsilon_{u,2}$ , įtempiai apskaičiuojami pagal išraišką (14).

$$\sigma(\varepsilon) = (\sigma_{u,red} - j_2) + j_2 \cdot e^{j_1(\varepsilon - \varepsilon_{u,2})}, \quad (14)$$

čia:  $j_1$  yra lakšto  $b/t$  santykio koeficientas, apskaičiuojamas pagal išraišką (15);  $j_2$  yra plieno takumo ribos koeficientas, apskaičiuojamas pagal išraišką (16).

$$j_1 = \begin{cases} -70 & \text{for } 40 \leq \frac{b}{t} \leq 56 \\ -13.9 - \frac{b}{t} & \text{for } 56 < \frac{b}{t} \leq 81 \end{cases}, \quad (15)$$

$$j_2 = 75 + \frac{20(f_y - 335)}{95}. \quad (16)$$

Kadangi lenkiamos sijos turi kreivį, gniuždomi jų lakštai išskiriami kaip skirtingas atvejis. Taigi, siūlomos atskiros kritinių ir maksimalių įtempių išraiškos lakštams, kurių takumo riba 335–430 MPa, o  $b/t$  santykis 60–81. Kritiniams įtempiams siūloma (17) išraiška.

$$\sigma_{cr,b} = a_{cr,b} \left( \frac{b}{t} \right) + c_{cr,b}, \quad (17)$$

čia:  $a_{cr,b}$  yra koeficientas, apskaičiuojamas iš (18) išraiškos;  $c_{cr,b}$  yra y sankirtos taškas, apskaičiuojamas iš (19) išraiškos.

$$a_{cr,b} = -0.96 - \frac{1.12(f_y - 335)}{95}, \quad (18)$$

$$c_{cr,b} = 265 + \frac{112(f_y - 335)}{95}. \quad (19)$$

Sijų gniuždomų lakštų maksimalių įtempių skaičiavimui siūloma (20) išraiška.

$$\sigma_{u,b} = a_{u,b} \left( \frac{b}{t} \right) + c_{u,b}, \quad (20)$$

čia:  $a_{u,b}$  yra koeficientas, apskaičiuojamas iš (21) išraiškos;  $c_{u,b}$  yra y sankirtos taškas, apskaičiuojamas iš (22) išraiškos.

$$a_{u,b} = -1.1 - \frac{0.9(f_y - 335)}{95}, \quad (21)$$

$$c_{u,b} = 300 + \frac{110(f_y - 335)}{95}. \quad (22)$$

Visos kitos išraiškos, išskyrus kritinių įtempių ir maksimalių įtempių, šių atveju yra taikomos tokios pat, kaip ir kolonų atveju.

### 3.4. Iteracinis sluoksnių metodas plonasienių plienbetoninių sijų įtempių-deformacijų analizei

Eksperimentinių kompozitinių sijų analizei buvo pritaikytas iteracinis sluoksnių metodas, pasiūlytas Augonio ir Zadlauskio [5]. Bendroji šio metodo išraiška aprašoma (23) formule.

$$[E]\{\varepsilon\} = \{F\}, \quad (23)$$

čia:  $[E]$  yra skerspjūvio standumo matrica, aprašoma (24) išraiška;  $\{\varepsilon\}$  yra deformacijų vektorius, aprašomas (25) išraiška;  $\{F\}$  yra apkrovos vektorius, aprašomas (26) išraiška.

$$[E] = \begin{bmatrix} 1 & -2 & 1 & 0 & \dots & 0 & 0 & 0 \\ 0 & 1 & -2 & 1 & \dots & 0 & 0 & 0 \\ 0 & 0 & 1 & -2 & \dots & 0 & 0 & 0 \\ \dots & \dots & \dots & \dots & \dots & \dots & \dots & \dots \\ 0 & 0 & 0 & 0 & \dots & -2 & 1 & 0 \\ 0 & 0 & 0 & 0 & \dots & 1 & -2 & 1 \\ (EA)_1 & (EA)_2 & (EA)_3 & (EA)_4 & \dots & (EA)_{n-2} & (EA)_{n-1} & (EA)_n \\ 0 & (EA)_2 d & 2(EA)_3 d & 3(EA)_4 d & \dots & (n-3)(EA)_{n-2} d & (n-2)(EA)_{n-1} d & (n-1)(EA)_n d \end{bmatrix}, \quad (24)$$

čia:  $(EA)_i$  yra sluoksnio medžiagų ašinio standumo suma;  $d$  yra sluoksnio storis.

$$\{\varepsilon\} = \{\varepsilon_1 \quad \varepsilon_2 \quad \varepsilon_3 \quad \varepsilon_4 \quad \varepsilon_5 \quad \varepsilon_6 \quad \dots \quad \varepsilon_n\}^T, \quad (25)$$

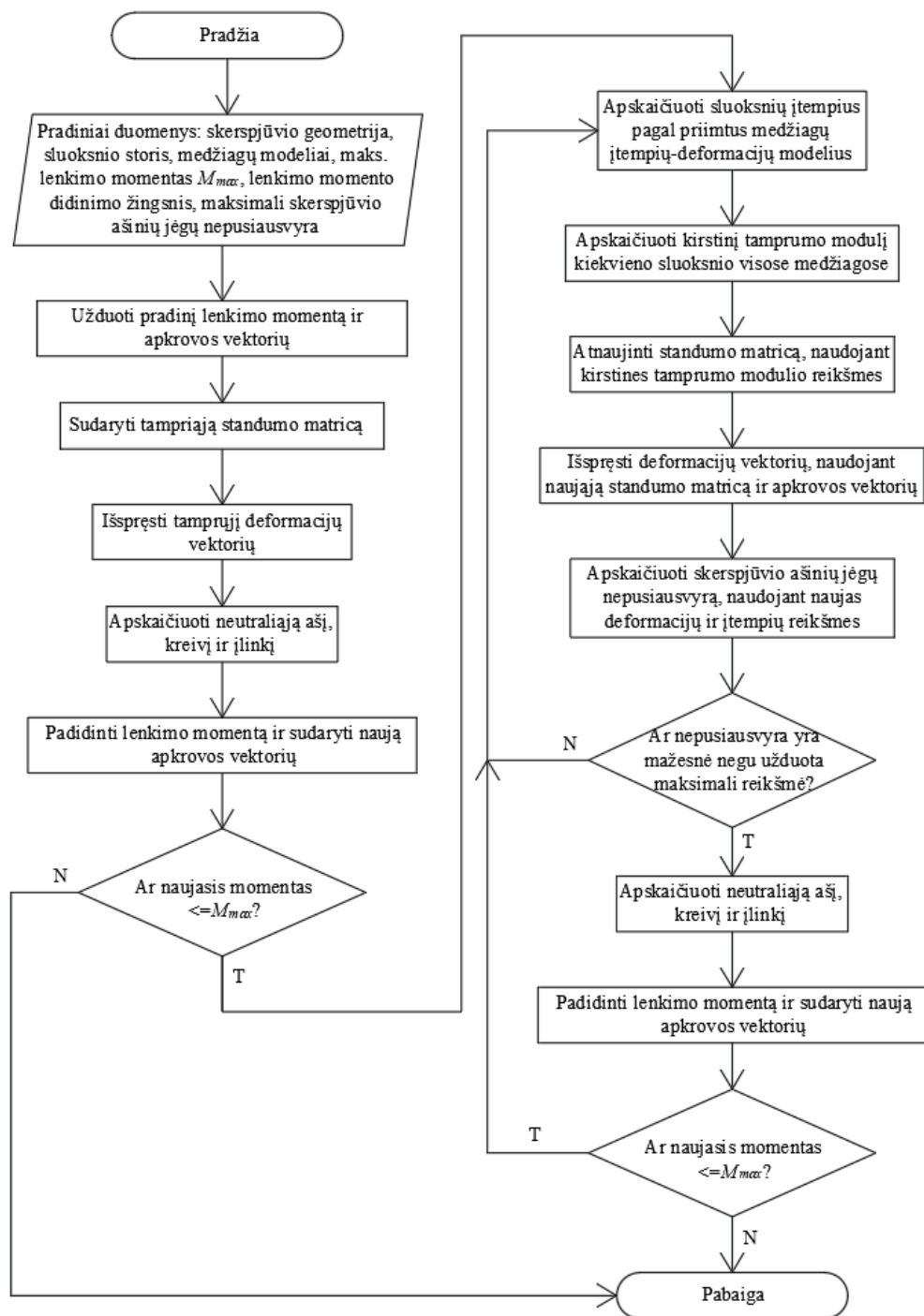
čia:  $\varepsilon_i$  sluoksnio deformacija.

$$\{F\} = \{0 \quad 0 \quad 0 \quad 0 \quad 0 \quad 0 \quad \dots \quad M\}^T. \quad (26)$$

čia:  $M$  yra išorinis lenkimo momentas.

Sluoksnio storis priimamas lygus analizuojamos sijos plieninio lakšto storiui. Analizuojant tris gretimus sluoksnius, remiamasi principu, jog vidurinio sluoksnio santykinė deformacija yra lygi išorinių sluoksnių santykinė deformacijų vidurkiui. Iteracijos yra kartojamos ir sluoksnių deformacijos yra perskaičiuojamos kiekvieną kartą. Atitinkamai kiekvienos iteracijos metu sluoksniuose yra apskaičiuojami įtempiai bei ašinių jėgų atstojamosios. Skaičiavimams nustatoma maksimali leistina ašinės jėgos nepusiausvyra, o iteracijos yra baigiamos, nepusiausvyrai nebeviršijant šios maksimalios reikšmės. Lenkimo momentas palaipsniui didinamas 2–4 % priimtos

maksimalios reikšmės. Skaičiavimai atliekami „Mathcad“ programa. Skaičiavimų iteraciniu sluoksnių metodu algoritmas pateiktas 22 pav.



22 pav. Skaičiavimo iteraciniu sluoksnių metodu algoritmas



Armatūrai buvo priimta bilininė elastoplastinė įtempių-deformacijų priklausomybė. Plieninių profilių sienutėms ir apatinėms juostoms priimta kreivė iki stiprumo ribos, modifikuota dėl liekamųjų įtempių pagal Song ir kt. [82]. Gniuždomiems plieno lakštams panaudotas siūlomas vidutinių normalinių įtempių-deformacijų modelis. Remiantis Liang [49] tyrimu, betonui aprašyti panaudota Mander ir kt. [58] bei Tomii ir Sakino [85] modelių kombinacija. Tempiamasis betono stipris apskaičiuotas pagal Eurokodą 2 [26].

## IV. REZULTATAI

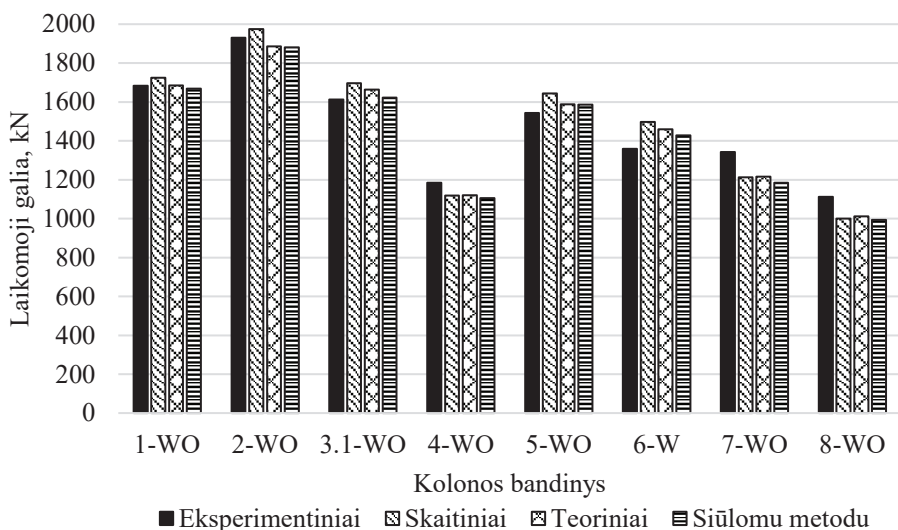
### 4.1. Plonasienių plienbetoninių kolonų rezultatai

Šiame skyriuje palyginami kolonų teoriniai ir eksperimentiniai rezultatai. Kolonų laikomosios galios rezultatai, gauti skaitinės analizės metu (indeksas „ $FE$ “), teoriniai rezultatai pagal Liang ir Uy [48] metodą (indeksas „ $Liang, Uy$ “), ir rezultatai, gauti naudojant siūlomas plieninių lakštų maksimalių įtempių reikšmes (indeksas „ $prop$ “), yra lyginami su eksperimentinėmis laikomosiomis galiomis ir yra pateikti 9 lent. Dauguma atvejų teorinės laikomosios galios reikšmės buvo šiek tiek didesnės už eksperimentines. Skaitinės ir teorinės laikomosios galios reikšmės buvo panašios tarpusavyje, kadangi jos remiasi eksperimentiškai nustatytais medžiagų parametrais, tačiau eksperimentiniai rezultatai taip pat priklauso nuo atsitiktinių veiksnių: betono stiprumo ir nuokrypių neapibrėžtumo, apkrovos ekscentriciteto, betono išsikišimų. Taigi, teorinė laikomoji galia svyravo nuo +9 % iki -11 %, lyginant su eksperimentine.

### 9 lentelė. Eksperimentiniai, teoriniai ir skaitiniai kolonų tyrimų rezultatai

Kolonos žymėjimas	$N_{u,ex}$ , kN	$N_{u,FE}$ , kN	$N_{u,Liang,Uy}$ , kN	$N_{u,prop}$ , kN	$N_{u,ex}/$ $N_{u,FE}$	$N_{u,ex}/$ $N_{u,Liang,Uy}$	$N_{u,ex}/$ $N_{u,prop}$
1-WO	1682,6	1724,0	1684,4	1668,2	0,98	1,00	1,01
2-WO	1930,5	1974,2	1886,4	1880,5	0,98	1,02	1,03
3.1-WO	1612,1	1696,6	1663,2	1623,0	0,95	0,97	0,99
4-WO	1184,2	1117,9	1120,6	1106,2	1,06	1,06	1,07
5-WO	1543,7	1643,1	1587,9	1586,9	0,94	0,97	0,97
6-W	1358,4	1498,0	1458,9	1427,9	0,91	0,93	0,95
7-WO	1343,2	1213,0	1216,5	1184,5	1,11	1,10	1,13
8-WO	1112,0	999,3	1011,6	993,6	1,11	1,10	1,12

9 lent. rezultatai taip pat pateikti grafine forma 23 pav. Pastebėta, kad kolonų, turinčių liauniausius lakštus, eksperimentinės laikomosios galios buvo šiek tiek mažesnės nei laikomosios galios, gautos skaitinės analizės metu. Kita vertus, kolonų, turinčių labiau kompaktiškus lakštus, eksperimentinė laikomoji galia buvo didesnė. Tikėtina, kad skaitinės analizės metu yra šiek tiek pervertinamas daugiaašio gniuždymo veikiamo betono stipris, analizuojant liaunus kolonų skerspjūvius, ir nepakankamai įvertinamas, kai kolonų skerspjūviai yra labiau kompaktiški. Panašūs skirtumai buvo gauti ir lyginant eksperimentinius bei teorinių skaičiavimų rezultatus. Taip pat pastebima, kad rezultatai, gauti siūlomu metodu, yra labai panašūs į rezultatus, gautus pagal Liang ir Uy [48] metodą, tačiau yra šiek tiek konservatyvesni.

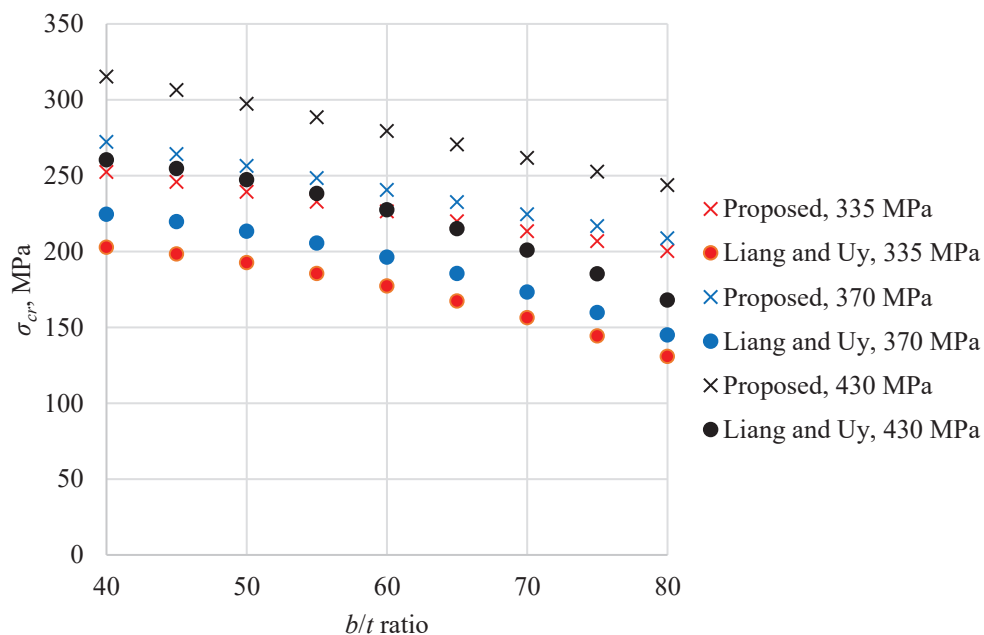


**23 pav.** Kolonų laikomosios galios rezultatų palyginimas

Kritiniai tik teoriškai analizuotų plieno lakštų, turinčių skirtingus  $b/t$  santykius, įtempiai buvo apskaičiuoti Liang ir kt. [53] metodu bei siūlomų metodu pagal išraišką (3). Panaudotos skirtingos plieno takumo ribų reikšmės. Šie rezultatai ir santykiai tarp kritinių įtempių, gautų skirtingais metodais, pateikti 10 lent. Čia  $\sigma_{cr,imp}$  yra kritiniai įtempiai, gauti pagal Liang ir kt. [53] metodą, o  $\sigma_{cr,prop}$  yra kritiniai įtempiai, gauti siūlomų metodu. Tie patys rezultatai pateikti ir grafine forma 24 pav. Pastebėta, kad rezultatai, gauti Liang ir kt. [53] metodu, yra labai konservatyvūs, lyginant su siūlomų metodu. Konservatyviausi rezultatai gauti plieno lakštams, turintiems 335 MPa takumo ribą ir didelį  $b/t$  santykį. Pabrėžtina, kad šie metodai sukurti, remiantis labai skirtingomis prielaidomis. Liang ir kt. [53] tyrime buvo analizuojami standžiai įtvirtinti plieniniai lakštai, turintys 0,1t amplitudės geometrinius nuokrypius. Siūlomas metodas sukurtas, remiantis trimačių plienbetoninių konstrukcijų modelių, turinčių  $B/200$  amplitudės geometrinius nuokrypius, analize.

**10 lentelė.** Kritinių įtempių rezultatų palyginimas

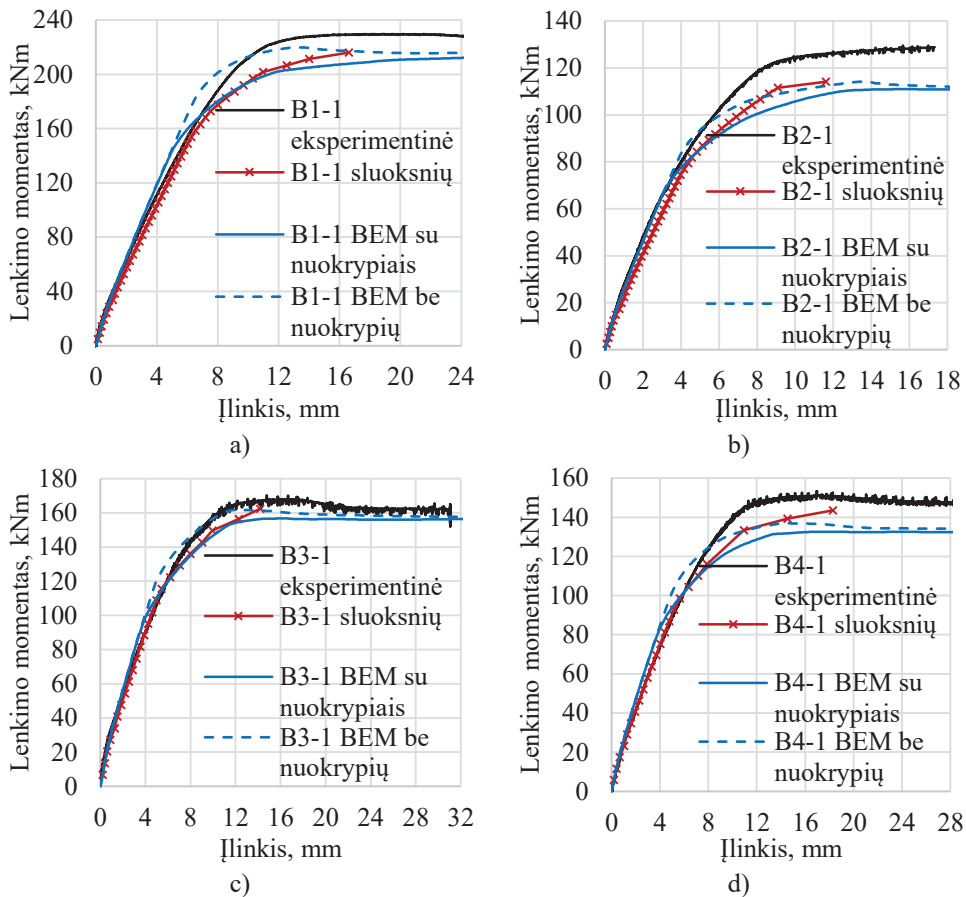
$b/t$	$\sigma_{cr,imp}$ , MPa	$\sigma_{cr,prop}$ , MPa	$\sigma_{cr,imp}/\sigma_{cr,prop}$	$\sigma_{cr,imp}$ , MPa	$\sigma_{cr,prop}$ , MPa	$\sigma_{cr,imp}/\sigma_{cr,prop}$	$\sigma_{cr,imp}$ , MPa	$\sigma_{cr,prop}$ , MPa	$\sigma_{cr,imp}/\sigma_{cr,prop}$
	$f_y=335$ MPa			$f_y=370$ MPa			$f_y=430$ MPa		
40	199,9	267,9	0,75	224,7	272,3	0,83	260,5	315,4	0,83
45	195,6	263,8	0,74	219,9	264,4	0,83	254,9	306,5	0,83
50	189,9	259,8	0,73	213,5	256,5	0,83	247,5	297,5	0,83
55	182,9	255,8	0,72	205,7	248,5	0,83	238,4	288,6	0,83
60	174,6	251,8	0,69	196,3	240,6	0,82	227,6	279,6	0,82
65	165,1	247,7	0,67	185,6	232,7	0,80	215,1	270,7	0,80
70	154,3	243,7	0,63	173,4	224,7	0,77	201,0	261,7	0,77
75	142,2	239,7	0,59	159,9	216,8	0,74	185,3	252,7	0,74
80	129,0	235,6	0,55	145,1	208,9	0,69	168,1	243,8	0,69



24 pav. Kritinių įtempių rezultatai

## 4.2. Plonasienių plienbetoninių sijų rezultatai

Lenkimo momento-įlinkio kreivės eksperimentinėms sijoms buvo gautos BE metodu (pirmas modelio tipas – su liekamaisiais įtempiais ir  $B/200$  amplitudės geometriniais nuokrypiais; antras modelio tipas – be nuokrypių: be liekamųjų įtempių, su  $B/500$  amplitudės geometriniais nuokrypiais) ir iteraciniu sluoksnių metodu. Šie teoriniai ir eksperimentiniai rezultatai pateikti 25 pav. Analizei sluoksnių metodu gniuždomiems lakštams buvo panaudotas siūlomas vidutinių normalinių įtempių-deformacijų modelis.



25 pav. Eksperimentinių sijų lenkimo momento-įlinkio kreivės

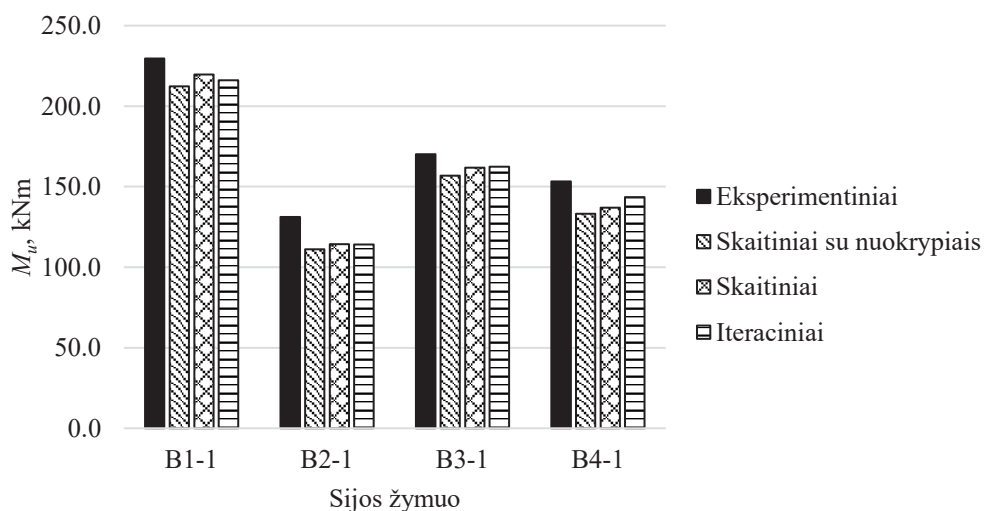
Teorinės ir eksperimentinės sijų momento-įlinkio kreivės sutapo gerai, tačiau kai kuriais atvejais eksperimentinės maksimalios lenkimo momentų reikšmės buvo iki 15 % didesnės. Liekamieji įtempiai lėmė ankstyvą sijų standumo sumažėjimą, tačiau net ir sijų, neturinčių nuokrypių, BE modeliai turėjo kiek mažesnę lenkiamąją galią. Tikėtina, kad pagrindinė šių skirtumų priežastis yra daugiaašis betono gniuždymas. Iteraciniam sluoksnių metodui panaudotas betono modelis neįvertina betono stiprumo padidėjimo. BE analizės metu daugiaašis gniuždymas įvertinamas plastiškojo irimo modelyje. Kita vertus, įmanoma, kad eksperimentinių sijų betono įtempiai gali pasiekti didesnes reikšmes nei tos, kurios gaunamos pagal minėtus skaičiavimo modelius.

Maksimalūs sijų lenkimo momentai ir eksperimentinių / teorinių maksimalių lenkimo momentų santykių reikšmės pateiktos 11 lent. Čia  $M_{u,ex}$  yra maksimalus eksperimentiškai gautas lenkimo momentas;  $M_{u,FE,imp}$  yra maksimalus momentas, gautas BE analizės metu, įvertinant pradinį nuokrypį;  $M_{u,FE}$  yra maksimalus momentas, gautas BE analizės metu, neįvertinant pradinio nuokrypio;  $M_{u,it}$  yra

maksimalus lenkimo momentas, gautas iteraciniu sluoksnių metodu. Skirtingiems metodams buvo gautos vidutinės eksperimentinio/teorinio lenkimo momento reikšmės. Remiantis šiais vidutiniais santykiais, tiksliausias skaičiavimo metodas buvo iteracinis sluoksnių metodas, kuriame buvo įvertintas siūlomas vidutinių normalinių įtempių-deformacijų modelis gniuždomiems plieno lakštams. 11 lent. rezultatai taip pat pateikti grafine forma 26 pav.

**11 lentelė.** Eksperimentinių, skaitinių ir iteracinio sluoksnių metodo maksimalių sijų lenkimo momentų rezultatų palyginimas

	$M_{u,ex}$ , kNm	$M_{u,FE,imp}$ , kNm	$M_{u,FE}$ , kNm	$M_{u,it}$ , kNm	$M_{u,ex}/$ $M_{u,FE,imp}$	$M_{u,ex}/$ $M_{u,FE}$	$M_{u,ex}/$ $M_{u,it}$
B1-1	229,6	212,3	219,7	216,0	1,08	1,04	1,06
B2-1	131,1	111,1	114,3	114,1	1,15	1,13	1,12
B3-1	170,2	156,8	161,8	162,4	1,08	1,05	1,05
B4-1	153,3	133,1	136,9	143,5	1,13	1,11	1,06
Vidutinis santykis					1,11	1,08	1,07



**26 pav.** Eksperimentinių, skaitinių ir iteracinio sluoksnių metodo maksimalių sijų lenkimo momentų rezultatai

## IŠVADOS

1. Atlikus literatūros analizę buvo nustatyta, kad naujausi plienbetoninių konstrukcijų tyrimai yra smarkiai orientuoti į itin stiprių medžiagų panaudojimą, konstrukcinę elgseną aukštesnėse temperatūrose, naujų tipų skerspjuvių, kuriuose tam tikros dalys yra jautrios vietiniam klupumui, o kitose dalyse betono šerdis yra veikiamą daugiaašio gniuždymo, vystymą. Tokių konstrukcijų analizei atlikti reikalingi iteraciniai skaičiavimo metodai. Skirtingi mokslininkai yra pasiūlę kritinių klupumo įtempių, maksimalių įtempių ir efektyviojo pločio skaičiavimo išraiškas lakštams plienbetoninėse konstrukcijose, tačiau jas sunku pritaikyti iteraciniuose skaičiavimo methoduose. Dažnai priimama, kad efektyvusis plotis vystosi tiesiškai tarp kritinių klupumo įtempių ir maksimalių įtempių, o efektyviojo pločio mažėjimas yra neįvertinamas. Tai neatitinka tikrosios tokių lakštų elgsenos.
2. Remiantis eksperimentiniais plienbetoninių kolonų ir sijų rezultatais buvo nustatyta, kad:
  - a) vidutinis kolonų plieninio profilio  $A_{eff}/A_s$  santykio sumažėjimas dėl prasto sukibimo buvo 12 %;
  - b) dauguma atvejų kolonų suirimas buvo plastiškas. Įvykus vietiniam klupumui, prasidėdavo įtempių persiskirstymas į profilio kampus. Keletas kolonų staigiau suiro dėl kampinių siūlių suirimo, jau pasiekus maksimalią laikomąją galią;
  - c) sijų suirimas buvo plastiškas. Neužfiksuotas žymus laikomosios galios mažėjimas. Gniuždomose sijų juostose išsivystydavo dvi arba trys klupumo bangos. Išklupus gniuždomai juostai, prasidėdavo sienelių klupumas.
3. Sukurti WO tipo kolonų baigtinių elementų modeliai, įvertinant  $B/200$  amplitudės geometrinius nuokrypius ir liekamuosius įtempius. Remiantis kolonų skaitinės analizės rezultatais:
  - a) nustatyta, kad lakšto, turinčio  $b/t = 40$  santykį, maksimalūs vidutiniai įtempiai buvo 33 % didesni negu lakšto, kurio  $b/t = 80$ . Šių lakštų maksimalūs vidutiniai įtempiai buvo 83 % ir 63 % plieno takumo ribos atitinkamai;
  - b) vietinis klupumas buvo staigesnis liaunesniuose plieno lakštuose, o labiau kompaktiškų lakštų klupumas vyko lėtai ir laipsniškai;
  - c) kritiniai klupumo įtempiai mažėjo tiesiškai,  $b/t$  santykiui didėjant intervale 40–80. Maksimalių vidutinių įtempių mažėjimas buvo eksponentiškas intervale 40–60 ir tiesinis intervale 60–80.
4. Visos eksperimentinės sijos ir du papildomi modeliai buvo išanalizuoti baigtinių elementų metodu. Remiantis sijų skaitinės analizės rezultatais:
  - a) sijų B3-1 ( $b/t = 79,7$ ) ir B4-1 ( $b/t = 59,8$ ) modeliai parodė, kad maksimalūs gniuždomų juostų vidutiniai įtempiai buvo 24–35 % didesni sijose su mažais pradiniais nuokrypiais. Maksimalūs vidutiniai įtempiai šiose sijose, turinčiose didelius pradinius nuokrypius, buvo lygūs 62 % ir 68 % plieno takumo ribos atitinkamai. Kita vertus, pasiekus didesnes deformacijas negu 0,01, didesni nuokrypiai turėjo labai mažą įtaką vidutinių įtempių-deformacijų būviui;
  - b) modeliai su liekamaisiais įtempiais ir geometrinių nuokrypių amplitude  $B/200$  parodė, kad 428,5 MPa takumo ribos lakštų kritiniai klupumo įtempiai buvo didesni negu 335,9 MPa takumo ribos lakštų 26 % ir 15 %, lyginant lakštus,

kurių *b/t* yra 60 ir 80 atitinkamai. 428,5 MPa takumo ribos lakštų maksimalūs vidutiniai įtempiai buvo didesni negu 335,9 MPa takumo ribos lakštų 27 % ir 21 %, lyginant lakštus, turinčius minėtus *b/t* santykius atitinkamai;

- c) maksimalūs vidutiniai normaliniai įtempiai gniuždomoje B3-1 sijos juostoje buvo pasiekti prieš sijai pasiekiant maksimalų lenkimo momentą. Pasiekus maksimalų lenkimo momentą, šios juostos vidutiniai įtempiai buvo žymiai sumažėję.
- 5. Pasiūlytas idealizuotas gniuždomų lakštų plienbetoninėse konstrukcijose vidutinių normalinių įtempių-deformacijų modelis, išskiriant kelis charakteringus ruožus: tiesinis įtempių-deformacijų ruožas prieš vietinį klupumą, sumažinto standumo ruožas tarp kritinių klupumo įtempių ir maksimalių įtempių, pastovių maksimalių įtempių ruožas ir neigiamas eksponentinis įtempių mažėjimo ruožas. Pasiūlytos skirtingos kritinių įtempių ir maksimalių įtempių skaičiavimo išraiškos gniuždomiems sijų ir kolonų lakštams.
- 6. Pasiūlytas vidutinių normalinių įtempių-deformacijų modelis buvo panaudotas sijų analizei iteraciniu sluoksnių metodu. Gautos lenkimo momento-įlinkio kreivės. Eksperimentinės lenkiamosios galios buvo 5–12 % didesnės už reikšmes, gautas iteraciniu sluoksnių metodu. Tikėtina, kad dėl plonasio plieninio profilio daugiaašio gniuždymo veikiamas betonas gali turėti didesnę stiprį. Tai nebuvo įvertinta iteraciniam sluoksnių metodui priimtame betono daugiaašio gniuždymo modelyje.

## REFERENCES

1. AHMED, M. and Q. Q. LIANG. Numerical analysis of thin-walled round-ended concrete-filled steel tubular short columns including local buckling effects. *Structures* [interactive]. Elsevier, 1 December 2020, vol. 28, 181–196. Access via doi: 10.1016/j.istruc.2020.08.051
2. AISC. *ANSI/AISC 360-05. An American National Standard. Specifications for Structural Steel Buildings*. Chicago: American Institute of Steel Construction, 2005. ISBN 0050061291.
3. AISC. *Load and Resistance Factor Design Specification for Structural Steel Buildings*. Chicago: American Institute of Steel Construction, 1999. ISBN 1-56424-041-X.
4. ÅKESSON, B. *Plate buckling in bridges and other structures*. London: Taylor & Francis, 2007. ISBN 978-0415431958.
5. AUGONIS, M. and S. ZADLAUSKAS. The elastoplastic concrete strain influence on the cracking moment and deformation of rectangular reinforced concrete elements. *Mechanika* [interactive]. Kaunas University of Technology, 27 February 2013, vol. 19, no. 1, 5–11. Access via doi: 10.5755/j01.mech.19.1.36199
6. BALTAY, P. and A. GJELSVIK. Coefficient of Friction for Steel on Concrete at High Normal Stress. *Journal of Materials in Civil Engineering* [interactive]. American Society of Civil Engineers, 1 February 1990, vol. 2, no. 1, 46–49. Access via doi: 10.1061/(asce)0899-1561(1990)2:1(46)
7. BARTH, K. E. and D. W. WHITE. Finite element evaluation of pier moment-rotation characteristics in continuous-span steel I Girders. *Engineering Structures* [interactive]. Elsevier, August 1998, vol. 20, no. 8, 761–778. Access via doi: 10.1016/S0141-0296(97)00087-4
8. BHARTIYA, R., R. M. OINAM, D. R. SAHOO and K. UTKARSH. Modified confinement model for monotonic axial behavior of concrete-filled tubular columns. *Journal of Constructional Steel Research* [interactive]. Elsevier, 1 May 2021, vol. 180. Access via doi: 10.1016/j.jcsr.2021.106570
9. BISCAYA, A, J. J. P. OLIVEIRA and U. KUHLMANN. Experimental behaviour of longitudinally stiffened steel plate girders under combined bending, shear and compression. *Engineering Structures* [interactive]. Elsevier, 1 July 2021, vol. 238, 112139. Access via doi: 10.1016/j.engstruct.2021.112139
10. BJORHOVDE, R, J. BROZZETTI, G. A. ALPSTEN and L. TALL. Residual Stresses in Thick Welded Plates A study of the cooling and we/ding residual stresses in heavy plates provides a method for estimating the residual stresses in welded built-up structural shapes. *Welding Research Supplement* [interactive]. 1972, vol. 51, no. 8, 392–405. Available via: [http://files.aws.org/wj/supplement/WJ\\_1972\\_08\\_s392.pdf](http://files.aws.org/wj/supplement/WJ_1972_08_s392.pdf)
11. BONG KWON, Y., S. JUNG SEO and D. WON KANG. Prediction of the squash loads of concrete-filled tubular section columns with local buckling. *Thin-Walled Structures* [interactive]. Elsevier, 1 January 2011, vol. 49, no. 1, 85–93. Access via doi: 10.1016/j.tws.2010.08.009
12. BRADFORD, M. A., R. Q. BRIDGE, G. J. HANCOCK, J. M. ROTTER and N. S. TRAHAIR. Australian Limit State Design Rules for the Stability of Steel Structures. In: *1<sup>st</sup> Structural Engineering Conference*, 1987, Melbourne, Australia. ISBN 0858253518. 1987, p. 209–216.
13. BULSON, P. S. *The stability of flat plates*. London: Chatto & Windus, 1970. ISBN 0701114789.
14. CAN/CSA S16-01. *Limit state design of steel structures*. Canadian Standards Association, 2001.



15. CHEN C. C., J. W. KO, G. L. HUANG and Y. M. CHANG. Local buckling and concrete confinement of concrete-filled box columns under axial load. *Journal of Constructional Steel Research* [interactive]. Elsevier, 1 November 2012, vol. 78, 8–21. Access via doi: 10.1016/j.jcsr.2012.06.006
16. CHEN, J., J. WANG, X. JUN, J. FANG and W. L. JIN. Behavior of thin-walled dodecagonal section double skin concrete-filled steel tubes under bending. *Thin-Walled Structures* [interactive]. Elsevier, 1 January 2016, vol. 98, 293–300. Access via doi: 10.1016/j.tws.2015.10.002
17. CHEN, S. J. and S. C. CHANG. Residual stresses in welded jumbo box columns. *Journal of Constructional Steel Research* [interactive]. Elsevier, 1 January 1993, vol. 25, no. 3, 201–209. Access via doi: 10.1016/0143-974X(93)90017-M
18. DUARTE, A. P. C., B. A. SILVA, N. SILVESTRE, J. DE BRITO, E. JÚLIO, E. and J. M. CASTRO. Tests and design of short steel tubes filled with rubberised concrete. *Engineering Structures* [interactive]. Elsevier, 1 April 2016, vol. 112, 274–286. Access via doi: 10.1016/j.engstruct.2016.01.018
19. DUARTE, A. P. C., N. SILVESTRE, J. DE BRITO, E. JÚLIO and J. D. SILVESTRE. On the sustainability of rubberized concrete filled square steel tubular columns. *Journal of Cleaner Production* [interactive]. Elsevier, 1 January 2018, vol. 170, 510–521. Access via doi: 10.1016/j.jclepro.2017.09.131
20. DUARTE, A. P. C. *Strength and ductility of short rubberized concrete filled steel tubes for seismic areas*. Doctoral Thesis. Universidade de Lisboa, Lisbon, Portugal, 2018.
21. DUARTE, A. P. C., B. A. SILVA, N. SILVESTRE, J. DE BRITO, E. JÚLIO, and J. M. CASTRO. Finite element modelling of short steel tubes filled with rubberized concrete. *Composite Structures* [interactive]. Elsevier, 15 August 2016, vol. 150, 28–40. Access via doi: 10.1016/j.compstruct.2016.04.048
22. ELLOBODY, E. and B. YOUNG. Nonlinear analysis of concrete-filled steel SHS and RHS columns. *Thin-Walled Structures* [interactive]. Elsevier, August 2006, vol. 44, no. 8, 919–930. Access via doi: 10.1016/j.tws.2006.07.005
23. ELLOBODY, E., B. YOUNG and D. LAM. Behaviour of normal and high strength concrete-filled compact steel tube circular stub columns. *Journal of Constructional Steel Research* [interactive]. Elsevier, 1 July 2006, vol. 62, no. 7, 706–715. Access via doi: 10.1016/j.jcsr.2005.11.002
24. EN 12390-13. *Testing hardened concrete. Part 13: determination of secant modulus of elasticity in compression*. European committee for standardisation (CEN), 2013.
25. EN 12390-3. *Testing hardened concrete. Part 3: compressive strength of test specimens*. European committee for standardisation (CEN), 2019.
26. EN 1992-1-1. *Eurocode 2: design of concrete structures - Part 1-1: general rules and rules for buildings*. European committee for standardisation (CEN), 2004.
27. EN 1993-1-1. *Eurocode 3: design of steel structures - Part 1-1: general rules and rules for buildings*. European committee for standardisation (CEN), 2005.
28. EN 1993-1-5. *Eurocode 3: design of steel structures. Part 1-5: plated structural elements*. European committee for standardisation (CEN), 2005.
29. EN 1994-1-1. *Eurocode 4: design of composite steel and concrete structures. Part 1-1: general rules and rules for buildings*. European committee for standardisation (CEN), 2004.
30. EN 1994-1-2. *Eurocode 4: design of composite steel and concrete structures. Part 1-2: general rules - structural fire design*. European committee for standardisation (CEN), 2004.
31. EN ISO 6892-1. *Metallic materials. Part 1: method of test at room temperature*. European committee for standardisation (CEN), 2019.

32. FIB (FÉDÉRATION INTERNATIONALE DU BÉTON). *fib Model Code for Concrete Structures 2010*. Berlin: Ernst & Sohn, 2013. ISBN 9783433604083.
33. FU, G., G. FU, C. YU, S. LI, F. WANG and J. YANG. Behaviour of rectangular concrete-filled steel tubular slender column with unequal wall thickness. *Engineering Structures* [interactive]. Elsevier, 1 June 2021, vol. 236. Access via doi: 10.1016/j.engstruct.2021.112100
34. GE, H. B. and T. USAMI. Strength analysis of concrete-filled thin-walled steel box columns. *Journal of Constructional Steel Research* [interactive]. 1994, vol. 30, no. 3, 259–281. Access via doi: 10.1016/0143-974X(94)90003-5
35. HAJJAR, J. F. and B. C. GOURLEY. Representation of Concrete-Filled Steel Tube Cross-Section Strength. *Journal of Structural Engineering* [interactive]. November 1996, vol. 122, no. 11, 1327–1336. Access via doi: 10.1061/(ASCE)0733-9445(1996)122:11(1327)
36. HAN, L. H. Flexural behaviour of concrete-filled steel tubes. *Journal of Constructional Steel Research* [interactive]. Elsevier, 1 February 2004, vol. 60, no. 2, 313–337. Access via doi: 10.1016/J.JCSR.2003.08.009
37. HAN, L. H., X. L. ZHAO and Z. TAO. Tests and mechanics model for concrete-filled SHS stub columns, columns and beam-columns. *Steel and Composite Structures* [interactive]. Techno-Press, 25 March 2001, vol. 1, no. 1, 51–74. Access via doi: 10.12989/scs.2001.1.1.051
38. HU, H. T., C. S. HUANG, M. H. WU and Y. M. WU. Nonlinear Analysis of Axially Loaded Concrete-Filled Tube Columns with Confinement Effect. *Journal of Structural Engineering* [interactive]. ASCE library, October 2003, vol. 129, no. 10, 1322–1329. Access via doi: 10.1061/(ASCE)0733-9445(2003)129:10(1322)
39. HUANG Z., D. LI, B. UY, H. T. THAI, and C. HOU. Local and post-local buckling of fabricated high-strength steel and composite columns. *Journal of Constructional Steel Research* [interactive]. Elsevier, 1 March 2019, vol. 154, 235–249. Access via doi: 10.1016/j.jcsr.2018.12.004
40. JIANG, A. U, J. CHEN and W. L. JIN. Experimental investigation and design of thin-walled concrete-filled steel tubes subject to bending. *Thin-Walled Structures* [interactive]. Elsevier, 1 February 2013, vol. 63, 44–50. Access via doi: 10.1016/j.tws.2012.10.008
41. JOHANSSON, M. and M. ÅKESSON. Finite Element Study of Concrete-Filled Steel Tubes Using a New Confinement-Sensitive Concrete Compression Model. *Nordic Concrete Research* [interactive]. Nordic Concrete Federation, January 2002, vol. 27, 43–62. Access via: <https://nordicconcrete.net/wp-content/uploads/2017/11/NCR-27-5.pdf>
42. KAMIL G. M., Q. Q. LIANG and M. N. S. HADI. Nonlinear post-fire simulation of concentrically loaded rectangular thin-walled concrete-filled steel tubular short columns accounting for progressive local buckling. *Thin-Walled Structures* [interactive]. Elsevier, 1 December 2019, vol. 145. Access via doi: 10.1016/j.tws.2019.106423
43. KAMIL G. M., Q. Q. LIANG and M. N. S. HADI. Fiber element simulation of interaction behavior of local and global buckling in axially loaded rectangular concrete-filled steel tubular slender columns under fire exposure. *Thin-Walled Structures* [interactive]. Elsevier, 1 December 2019, vol. 145. Access via doi: 10.1016/j.tws.2019.106403
44. KAZEMZADEH AZAD, S. and B. UY. Effect of concrete infill on local buckling capacity of circular tubes. *Journal of Constructional Steel Research* [interactive]. Elsevier, 1 February 2020, vol. 165. Access via doi: 10.1016/j.jcsr.2019.105899

45. KENT D. C. and R. PARK. Flexural Members with Confined Concrete. *Journal of the Structural Division* [interactive]. American Society of Civil Engineers, 1 July 1971, vol. 97, no. 7, 1969–1990. Access via doi: 10.1061/jsdeag.0002957
46. LACROIX, E. A. *Comparative study of strength design methods for rectangular reinforced concrete and composite steel-concrete columns*. Master's thesis [interactive]. University of Manitoba, Winnipeg, Canada, 1998. Access via: <https://mspace.lib.umanitoba.ca/xmlui/handle/1993/1362?show=full>
47. LESKELÄ, M. *Behaviour and design of steel-concrete composite structures*. Lahti: Peikko Group Corporation, 2017.
48. LIANG, Q. Q. and B. UY. Theoretical study on the post-local buckling of steel plates in concrete-filled box columns. *Computers and Structures* [interactive]. Elsevier, 2000, vol. 75, 479–490. Access via doi: 10.1016/S0045-7949(99)00104-2
49. LIANG, Q. Q. *Analysis and design of steel and composite structures*. Boca Raton: CRC Press, 2015. ISBN 9780415532204.
50. LIANG, Q. Q. Performance-based analysis of concrete-filled steel tubular beam-columns, Part I: Theory and algorithms. *Journal of Constructional Steel Research* [interactive]. Elsevier, 2009, vol. 65, no. 2, 363–372. Access via doi: 10.1016/j.jcsr.2008.03.007
51. LIANG, Q. Q. *Performance-based optimization of structures: theory and applications*. London: Spon Press, 2005. ISBN 020333471X.
52. LIANG, Q. Q. Performance-based analysis of concrete-filled steel tubular beam-columns, Part II: Verification and applications. *Journal of Constructional Steel Research* [interactive]. Elsevier, 2009, vol. 65, no. 2, 351–362. Access via doi: 10.1016/j.jcsr.2008.03.003
53. LIANG, Q. Q., B. UY and J. Y. R. LIEW. Local buckling of steel plates in concrete-filled thin-walled steel tubular beam-columns. *Journal of Constructional Steel Research* [interactive]. Elsevier, March 2007, vol. 63, no. 3, 396–405. Access via doi: 10.1016/j.jcsr.2006.05.004
54. LIANG, Q. Q., B. UY and J. Y. R. LIEW. Nonlinear analysis of concrete-filled thin-walled steel box columns with local buckling effects. *Journal of Constructional Steel Research* [interactive]. Elsevier, 1 June 2006, vol. 62, no. 6, 581–591. Access via doi: 10.1016/j.jcsr.2005.09.007
55. LIM, J. J. and T. S. EOM. Compression tests of octagonal concrete-filled thin-walled tube columns. *Engineering Structures* [interactive]. Elsevier, 15 October 2020, vol. 221. Access via doi: 10.1016/j.engstruct.2020.111082
56. LONG, Y. L., J. WAN and J. CAI. Theoretical study on local buckling of rectangular CFT columns under eccentric compression. *Journal of Constructional Steel Research* [interactive]. Elsevier, 1 April 2016, vol. 120, 70–80. Access via doi: 10.1016/j.jcsr.2015.12.029
57. LONG, Y. L. and L. ZENG. A refined model for local buckling of rectangular CFST columns with binding bars. *Thin-Walled Structures* [interactive]. Elsevier, 1 November 2018, vol. 132, 431–441. Access via doi: 10.1016/j.tws.2018.09.019
58. MANDER, J. B., M. J. N. PRIESTLEY and R. PARK. Theoretical Stress-Strain Model for Confined Concrete. *Journal of Structural Engineering* [interactive]. American Society of Civil Engineers, 1 September 1988, vol. 114, no. 8, 1804–1826. Access via doi: 10.1061/(asce)0733-9445(1988)114:8(1804)
59. MANDER, J. B., M. J. N. PRIESTLEY and R. PARK. Observed Stress-Strain Behavior of Confined Concrete. *Journal of Structural Engineering* [interactive]. American Society of Civil Engineers, 1 September 1988, vol. 114, no. 8, 1827–1849. Access via doi: 10.1061/(asce)0733-9445(1988)114:8(1827)

60. MARTINAVIČIUS, D. and M. AUGONIS. Influence of imperfections on behaviour of thin-walled steel-concrete composite columns. *Mechanika* [interactive]. Kauno Technologijos Universitetas, 24 February 2021, vol. 27, no. 1, 5–11. Access via doi: 10.5755/J02.mech.25935
61. MARTINAVIČIUS, D. and M. AUGONIS. Experimental Research of the Reinforced Concrete-filled Thin-walled Steel Beams. In: *Advanced Construction and Architecture. Proceedings of 1<sup>st</sup> International Scientific Conference*, 23-25 September 2020, Kaunas, Lithuania. Kaunas: Technologija. ISSN 2669-1922. 2020, p. 75-76. Access via doi: 10.5755/e01.2669-1922.2020
62. MARTINAVIČIUS, D., M. AUGONIS, N. ADAMUKAITIS and T. ZINGAILA. Experimental and Numerical Investigation of Concrete Filled Closed Section Steel Beams. In: *Advanced Construction 2018. Proceedings of 6<sup>th</sup> International Scientific Conference*, 20 September 2018, Kaunas, Lithuania. Kaunas: Technologija. ISSN 2029-1213. 2018, p. 74-75. Access via doi: 10.5755/e01.2538-8983.2018
63. MARTINAVIČIUS, D., M. AUGONIS, N. ADAMUKAITIS and T. ZINGAILA. Experimental and Numerical Investigation of Concrete Filled Closed Section Steel Beams. *Journal of Sustainable Architecture and Civil Engineering* [interactive]. Technologija, 3 October 2018, vol. 22, no. 1, 88–98. Access via doi: 10.5755/j01.sace.22.1.20862
64. MARTINAVIČIUS, D., M. AUGONIS and M. R. T. ARRUDA. Experimental and analytical study on local buckling behavior of the concrete-filled thin-walled welded steel columns. *Periodica Polytechnica Civil Engineering* [interactive]. Budapest University of Technology and Economics, 3 September 2020, vol. 64, no. 3, 917–927. Access via doi: 10.3311/PPci.15705
65. MCANALLEN, L. E., D. A. PADILLA-LLANO, X. ZHAO, C. D. MOEN, B. W. SCHAFER and M. R. EATHERTON. Initial Geometric Imperfection Measurement and Characterization of Cold-Formed Steel C-Section Structural Members with 3D Non-Contact Measurement Techniques. In: *Proceedings of the Annual Stability Conference Structural Stability Research Council*, 25-28 March 2014, Toronto, Canada. Available via: <https://www.aisc.org/globalassets/continuing-education/ssrc-proceedings/2014/initial-geometric-imperfection-measurement-and-characterization-of-cold-formed-steel-c-section-structural-members-with-3d-non-contact-measurement-techniques.pdf>
66. NAKAI, H., T. KITADA and O. YOSHIKAWA. A design method of steel plate elements in concrete filled square steel tubular columns [in Japanese]. *Doboku Gakkai Ronbunshu* [interactive]. Japan Society of Civil Engineers, 20 April 1985, vol. 1985, no. 356, 405–413. Access via doi: 10.2208/jscej.1985.356\_405
67. NASCIMENTO, S., J. J. P. OLIVEIRA and A. BISCAYA. Flange-induced buckling of plate girders of high strength steel. *Thin-Walled Structures* [interactive]. Elsevier, 1 February 2021, vol. 159. Access via doi: 10.1016/j.tws.2020.106974
68. PAN, Y. G. Analysis of complete curve of concrete filled steel tubular stub columns under axial compression [in Chinese]. In: *Proceedings of International Conference on Concrete Filled Steel Tubular Structures*. Harbin, PR China. 1988, p. 87–93.
69. PHAN, D. H. H., V. I. PATEL, Q. Q. LIANG, H. AL ABADI, and H. T. THAI. Simulation of uniaxially compressed square ultra-high-strength concrete-filled steel tubular slender beam-columns. *Engineering Structures* [interactive]. Elsevier, 1 April 2021, vol. 232. Access via doi: 10.1016/j.engstruct.2020.111795
70. RABBAT, B. G. and H. G. RUSSELL. Friction coefficient of steel on concrete or grout. *Journal of Structural Engineering* [interactive]. American Society of Civil Engineers,

- March 1985, vol. 111, no. 3, 505–515. Access via doi: 10.1061/(ASCE)0733-9445(1985)111:3(505)
71. RAGHEB, W. F. Local buckling of welded steel I-beams considering flange-web interaction. *Thin-Walled Structures* [interactive]. Elsevier, 2015, vol. 97, 241–249. Access via doi: 10.1016/j.tws.2015.09.026
  72. RAMBERG, W. and W. R. OSGOOD. Description of Stress-Strain Curves by Three Parameters. *NACA Technical Notes* [interactive], 1943, no. 902. Available via: <http://www.apesolutions.com/spd/public/NACA-TN902.pdf>
  73. LIEW, J. Y. R. and D. X. XIONG. Effect of preload on the axial capacity of concrete-filled composite columns. *Journal of Constructional Steel Research* [interactive]. Elsevier, 1 March 2009, vol. 65, no. 3, 709–722. Access via doi: 10.1016/j.jcsr.2008.03.023
  74. RICHART, F. E., A. BRANDTZAEG and R. L. BROWN. A study of the failure of concrete under combined compressive stresses. *University of Illinois Bulletin* [interactive], 1928, vol. 26, no. 12. Access via: <https://www.ideals.illinois.edu/bitstream/handle/2142/4277/engineeringexperv00000i00185.pdf?sequence=3&isAllowed=y>
  75. ROSSI, A., A. S. C. DE SOUZA, R. S. NICOLETTI, and C. H. MARTINS. The influence of structural and geometric imperfections on the LDB strength of steel–concrete composite beams. *Thin-Walled Structures* [interactive]. Elsevier, 1 May 2021, vol. 162. Access via doi: 10.1016/j.tws.2021.107542
  76. SCHNEIDER, S. P. Axially loaded concrete-filled steel tubes. *Journal of Structural Engineering* [interactive]. American Society of Civil Engineers, 1 October 1998, vol. 124, no. 10, 1125–1138. Access via doi: [https://doi.org/10.1061/\(ASCE\)0733-9445\(1998\)124:10\(1125\)](https://doi.org/10.1061/(ASCE)0733-9445(1998)124:10(1125))
  77. SEIF M. and B. W. SCHAFER. Local buckling of structural steel shapes. *Journal of Constructional Steel Research* [interactive]. Elsevier, 2010, vol. 66, no. 10, 1232–1247. Access via doi: 10.1016/j.jcsr.2010.03.015
  78. SHI, G., X. KELONG, H. BAN and C. LIN. Local buckling behavior of welded stub columns with normal and high strength steels. *Journal of Constructional Steel Research* [interactive]. Elsevier, 1 March 2016, vol. 119, 144–153. Access via doi: 10.1016/j.jcsr.2015.12.020
  79. SIMULIA. ABAQUS/CAE User’s Manual, Version 6.14, 2013. Available via: <http://abaqus.software.polimi.it/v6.14/books/usi/default.htm>
  80. SOMODI, B. and B. KÖVESDI. Residual stress measurements on welded square box sections using steel grades of S235–S960. *Thin-Walled Structures* [interactive]. Elsevier, 1 February 2018, vol. 123, 142–154. Access via doi: 10.1016/j.tws.2017.11.028
  81. SONG, T. Y., T. ZHONG, L. H. HAN and B. UY. Bond Behavior of Concrete-Filled Steel Tubes at Elevated Temperatures. *Journal of Structural Engineering* [interactive]. 2017, vol. 143, no. 11. Access via doi: 10.1061/(asce)st.1943-541x.0001890
  82. SONG, Y. C., R. P. WANG and J. LI. Local and post-local buckling behavior of welded steel shapes in partially encased composite columns. *Thin-Walled Structures* [interactive]. Elsevier, 2016, vol. 108, 93–108. Access via doi: 10.1016/j.tws.2016.08.003
  83. SONG, Y., J. LI and Y. CHEN. Local and post-local buckling of normal/high strength steel sections with concrete infill. *Thin-Walled Structures* [interactive]. May 2019, vol. 138, 155–169. Access via doi: 10.1016/j.tws.2019.02.004
  84. SZALAI, J. and F. PAPP. A new residual stress distribution for hot-rolled I-shaped sections. *Journal of Constructional Steel Research* [interactive]. June 2005, vol. 61, no. 6, 845–861. Access via doi: 10.1016/j.jcsr.2004.12.004



85. TOMII, M. and K. SAKINO. Elasto-plastic behavior of concrete filled square steel tubular beam-columns. *Transactions of the Architectural Institute of Japan* [interactive]. Architectural Institute of Japan, 30 June 1979, vol. 280, 111–122. Access via doi: 10.3130/aijsaxx.280.0\_111
86. UY, B. Local and post-local buckling of concrete filled steel welded box columns. *Journal of Constructional Steel Research* [interactive]. Elsevier, 1 August 1998, vol. 47, no. 1–2, 47–72. Access via doi: 10.1016/S0143-974X(98)80102-8
87. UY, B. Strength of Concrete Filled Steel Box Columns Incorporating Local Buckling. *Journal of Structural Engineering* [interactive]. March 2000, vol. 126, no. 3, 341–352. Access via doi: 10.1061/(ASCE)0733-9445(2000)126:3(341)
88. UY, B. Local and Postlocal Buckling of Fabricated Steel and Composite Cross Sections. *Journal of Structural Engineering* [interactive]. American Society of Civil Engineers, June 2001, vol. 127, no. 6, 666–677. Access via doi: 10.1061/(ASCE)0733-9445(2001)127:6(666)
89. VRCELJ, Z. and B. UY. Strength of slender concrete-filled steel box columns incorporating local buckling. *Journal of Constructional Steel Research* [interactive]. Elsevier, 1 February 2002, vol. 58, no. 2, 275–300. Access via doi: 10.1016/S0143-974X(01)00045-1
90. WANG, Y. C. A simple method for calculating the fire resistance of concrete-filled CHS columns. *Journal of Constructional Steel Research* [interactive]. Elsevier, 1 June 2000, vol. 54, no. 3, 365–386. Access via doi: 10.1016/S0143-974X(99)00061-9
91. WILLIAMSON, S. J., P. F. PALLETT and L. A. CLARK. *Friction in temporary works*. Birmingham: HSE books, 2003. ISBN 071762613X.
92. WINTER, G. Strength of Thin Steel Compression Flanges. *Transactions* [interactive]. American Society of Civil Engineers, 1947, vol. 112, no. 1, 527–554. Access via: [https://www.ce.jhu.edu/cfs/cfslibrary/winter\\_strength\\_of\\_thin\\_steel\\_flanges\\_eff\\_width.pdf](https://www.ce.jhu.edu/cfs/cfslibrary/winter_strength_of_thin_steel_flanges_eff_width.pdf)
93. WRIGHT, H. D. Local Stability of Filled and Encased Steel Sections. *Journal of Structural Engineering* [interactive]. October 1995, vol. 121, no. 10, 1382–1388. Access via doi: 10.1061/(ASCE)0733-9445(1995)121:10(1382)
94. XIONG, M. X., D. X. XIONG and J. Y. R. LIEW. Behaviour of steel tubular members infilled with ultra high strength concrete. *Journal of Constructional Steel Research* [interactive]. Elsevier, 1 November 2017, vol. 138, 168–183. Access via doi: 10.1016/j.jcsr.2017.07.001
95. YAMAKI, N. Postbuckling behavior of rectangular plates with small initial curvature loaded in edge compression. *Journal of Applied Mechanics* [interactive]. American Society of Mechanical Engineers Digital Collection, 1 June 1960, vol. 27, no. 2, 335–342. Access via doi: 10.1115/1.3643962
96. YAN, B., X. ZHOU and J. LIU. Behavior of circular tubed steel-reinforced-concrete slender columns under eccentric compression. *Journal of Constructional Steel Research* [interactive]. Elsevier, 1 April 2019, vol. 155, 342–354. Access via doi: 10.1016/j.jcsr.2018.11.018
97. YOUNG, B. W. Residual stresses in hot rolled members. *IABSE reports of the working commissions* [interactive], 1975, 25–38. Access via doi: 10.5169/seals-19798
98. ZHANG, Q., L. FU and L. XU. An efficient approach for numerical simulation of concrete-filled round-ended steel tubes. *Journal of Constructional Steel Research* [interactive]. Elsevier, 1 July 2020, vol. 170. Access via doi: 10.1016/j.jcsr.2020.106086
99. ZHANG, R. L., J. LIU, W. WANG and Y. F. CHEN. Fire behaviour of thin-walled steel tube confined reinforced concrete stub columns under axial compression. *Journal of*

- Constructional Steel Research* [interactive]. Elsevier, 1 September 2020, vol. 172. Access via doi: 10.1016/j.jcsr.2020.106180
100. ZHANG, Z., S. XU, Y. WANG, B. NIE and T. WEI. Local and post-buckling behavior of corroded axially-compressed steel columns. *Thin-Walled Structures* [interactive]. Elsevier, 1 December 2020, vol. 157. Access via doi: 10.1016/j.tws.2020.107108
  101. ZUBYDAN, A. H. and A. I. ELSABBAGH. Monotonic and cyclic behavior of concrete-filled steel-tube beam-columns considering local buckling effect. *Thin-Walled Structures* [interactive]. Elsevier, 1 April 2011, vol. 49, no. 4, 465–481. Access via doi: 10.1016/j.tws.2010.12.007

## **CURRICULUM VITAE**

### **Personal information**

Deividas Martinavičius was born on 9<sup>th</sup> of July 1992 in Kaunas.

Email: [deividas.martinavicius1@gmail.com](mailto:deividas.martinavicius1@gmail.com), [deividas.martinavicius@ktu.lt](mailto:deividas.martinavicius@ktu.lt)

### **Education**

2003–2011: Garliava, Juozo Lukšos Gymnasium;

2011–2015: Bachelor studies and BA degree of Civil Engineering at Kaunas University of Technology, Faculty of Civil Engineering and Architecture;

2015–2017: Master studies and MA degree of Civil Engineering at Kaunas University of Technology, Faculty of Civil Engineering and Architecture.

2017–2021: Doctoral studies of Civil Engineering at Kaunas University of Technology, Faculty of Civil Engineering and Architecture.

### **Scientific internships**

An internship at the University of Lisbon, Higher Technical Institute (IST) from 1<sup>st</sup> of February 2019 to 31<sup>st</sup> of May 2019.



## **LIST OF SCIENTIFIC ARTICLES ON THE DISSERTATION TOPIC**

### **Publications in journals indexed on Clarivate Analytics Web of Science**

1. Martinavičius, Deividas; Augonis, Mindaugas. Influence of imperfections on behaviour of thin-walled steel-concrete composite columns // *Mechanika*. Kaunas: Kaunas University of Technology. ISSN 1392-1207. eISSN 2029-6983. 2021, vol. 27, no. 1, p. 5-11. DOI: 10.5755/j02.mech.25935. [Science Citation Index Expanded (Web of Science); Scopus; Academic Search Complete].
2. Martinavičius, Deividas; Augonis, Mindaugas; Arruda, Mário Rui Tiago. Experimental and analytical study on local buckling behavior of the concrete-filled thin-walled welded steel columns // *Periodica Polytechnica Civil Engineering*. Budapest: Budapest University of Technology and Economics. ISSN 0553-6626. eISSN 1587-3773. 2020, vol. 64, no. 3, p. 917-927. DOI: 10.3311/PPci.15705. [Science Citation Index Expanded (Web of Science); Scopus].

### **Other publications in journals indexed in international databases**

1. Martinavičius, Deividas; Augonis, Mindaugas; Adamukaitis, Nerijus; Zingaila, Tadas. Experimental and numerical investigation of concrete filled closed section steel beams // *Journal of Sustainable Architecture and Civil Engineering = Darnioji Architektūra ir Statyba*. Kaunas: Technologija. ISSN 2029-9990. eISSN 2335-2000. 2018, vol. 22, no. 1, p. 88-98. DOI: 10.5755/j01.sace.22.1.20862. [Index Copernicus].

### **Proceedings of international conferences**

1. Martinavičius, Deividas; Augonis, Mindaugas. Experimental research of the reinforced concrete-filled thin-walled steel beams // *Advanced Construction and Architecture: Proceedings of the 1<sup>st</sup> International Scientific Conference*, 23-25, September, 2020, Kaunas, Lithuania. Kaunas: Technologija. ISSN 2669-1922. 2020, p. 75-76. DOI: 10.5755/e01.2669-1922.2020.
2. Martinavičius, Deividas; Augonis, Mindaugas; Adamukaitis, Nerijus; Zingaila, Tadas. Experimental and numerical investigation of concrete filled closed section steel beams // *Advanced Construction 2018: Proceedings of the 6<sup>th</sup> International Scientific Conference*, September 20th, 2018, Kaunas, Lithuania. Kaunas: Technologija. ISSN 2029-1213. eISSN 2538-8983. 2018, p. 74-75. DOI: 10.5755/e01.2538-8983.2018



UDK 624.016(043.3)

SL 344. 2022-03-28, 17,75 leidyb. apsk. l. Tiražas 14 egz. Užsakymas 67.  
Išleido Kauno technologijos universitetas, K. Donelaičio g. 73, 44249 Kaunas  
Spausdino leidyklos „Technologija“ spaustuvė, Studentų g. 54, 51424 Kaunas

